HIGH PERFORMANCE PHOTO-DETECTORS AND FIELD EFFECT TRANSISTORS BASED ON LOW TEMPERATURE SOLUTION PROCESSING ROUTES

A Thesis Submitted to the

UNIVERSITY OF PUNE

For the Degree of

DOCTOR OF PHILOSOPHY

In

PHYSICS

By
LILY MANDAL

DR. JYOTI P. JOG
(RESEARCH GUIDE)

DR. S. B. OGALE
(RESEARCH CO-GUIDE)

NATIONAL CHEMICAL LABORATORY

PUNE – 411 008, INDIA

SEPTEMBER 2013

Dedicated
To
My
Beloved
Family

सीएसआयआर–राष्ट्रीय रासायनिक प्रयोगशाला
(वैज्ञानिक तथा औद्योगिक अनुसंधान परिषद)
डॉ. होमी भाभा मार्ग, पुणे – 411 008. भारत
CSIR-NATIONAL CHEMICAL LABORATORY
(Council of Scientific & Industrial Research)
Dr. Homi Bhabha Road, Pune - 411008. India

CERTIFICATE

This is to certify that the work presented in the thesis entitled "**High Performance Photo-detectors and Field Effect Transistors Based on Low Temperature Solution Processing Routes**" by Lily Mandal, submitted for the degree Doctor of Philosophy in Physics was carried out under our supervision at the Polymer Science and Engineering Division, Physical and Material Chemistry Division, National Chemical Laboratory, Pune, 411008, India. All the materials from other sources have been duly acknowledged in the thesis.

Dr. Jyoti P Jog

Research Guide

Dr Satishchandra B. Ogale

Research Co-Guide

Date: 26/9/13

Place: NCL, Pune

Communication Channels
NCL Level DID : 2590
NCL Board No. : +91-20-25902000
EPABX : +91-20-25893300
: +91-20-25893400
FAX
Director's Office : +91-20-25902601
COA's Office : +91-20-25902660
COS&P's Office : +91-20-25902664
WEBSITE
www.ncl-india.org

DECLARATION

I declare that the matter included in the thesis titled "**High Performance Photo-detectors and Field Effect Transistors Based on Low Temperature Solution Processing Routes**" submitted for the degree Doctor of Philosophy in Physics to the University of Pune, is the result of investigation carried by me at Polymer Science and Engineering Division and Physical and Material Chemistry Division of National Chemical Laboratory, Pune under the joint supervision of Dr. Jyoti P. Jog and Dr. Satishchandra B. Ogale. This work has not been submitted elsewhere for the award of any degree or diploma. Due acknowledgment has been made whenever the work described is based on the findings of other investigators.

Date: **Lily Mandal**

National Chemical Laboratory **(Research Student)**

Pune – 411 008

Acknowledgement

I am grateful to my research Guide Dr. Jyoti P. Jog for her guidance throughout this work. It has been a great privilege to work under her able guidance and valuable scientific advice over the past five years. I greatly appreciate the insights she provided in various studies, especially in the domain of polymer nanocomposites and their characterization. I also wish to express my heartfelt gratitude to her for motherly care, and friendly support throughout this journey.

My deepest gratitude is also to my research co-guide Dr. Satishchandra Ogale for his consistent guidance throughout my work. He always gave me the opportunity and constant support to explore and venture into whatever I wanted to learn. He has been a constant source of motivation and encouragement throughout these five years. He has nurtured my scientific skill, presentation skill, knowledge and made me a better person. It has been a pleasure to work in a group led by his never ending energy, ideas and motivation.

I am really grateful to both Dr. Jog and Dr. Ogale for their critical comments and tremendous efforts in preparing this dissertation.

I would like to acknowledge CSIR for the scholarship provided for my PhD work. I am sincerely obliged to the Director, National Chemical Laboratory (CSIR-NCL) for giving me opportunity to work at the Institute. I also wish to thank the Head, Polymer Science and Engineering Division, and the Head, Physical and Materials Chemistry Division, NCL for providing the infrastructural facilities to carry out the research work for Ph.D. I would like to thank the technical and non-technical staff of the Polymer Science and Engineering division for their help. I would also like to thank Dr. Dr. Krishnamoorthy, and Dr. Manjusha Shelke for their timely advice and help.

I take this opportunity to thank Dr.S.I.Patil, Head, Department of Physics, University of Pune for his scientific and administrative inputs and Dr. S. N. Kale, DIAT, Pune for her valuable scientific evaluations. I acknowledge Dr. H. H. Kumar, ARDE, Pune for providing the facilities and scientific discussions.

I would like to thank Dr. Subodh Mhasailkar, Energy Research Institute @ NTU (ERI@N) Nanyang Technological University, Singapore for providing me the opportunity to work in his lab for three months. It was a great learning experience. I would like to thank Dr. K.S. Narayanan (JNCSR), Dr. Ramagopal Rao (IIT Bombay) for providing me the opportunity to visit their lab and learn.

Special thanks to my present lab mates Dipti, Abhik, Rounak, Meenal, Vishal, Datta, Onkar, Anirruddha, Mandakini, Anil, Rohan, Dhanya, Shruti, Pooja, Nilima, Mukta, Reshma, Arif, Parvez, vivek, Yogesh, Umesh, Wahid, Sarika, Upendra, Divya, Ketki, Shraddha, Satyawan, Subhra, Aparna, Rupali, Dr. Sambhaji, Harish Sir, Ashish Sir, Sarika, Praverthana, Kirti, Sumit, Kush, Tanya, Divya, Prashant, Dhanalakshmi, Amol for a wonderful work environment. They all have been very helpful and very friendly. I have learnt a lot from them as well as my past lab mates Vivek, Abhimanyu, Prasad, Chetan, and Subhas. I would also like to thank friends from other labs which include Dr. Manohar Rao and Keke Zhang (NTU, Singapore) for their support in my research work.

I would like to take this opportunity to acknowledge all my teachers throughout my life for their knowledge, inspiration, blessing and belief in me which motivated me.

A special thanks to my parents for the freedom and faith to pursue my dream and my brother Manas for supporting and motivating me.

Lily Mandal

List of Abbreviations

QD	Quantum Dots
NIR	Near Infrared
0D	Zero- Dimensional
1D	One- Dimensional
2D	Two- Dimensional
3D	Three- Dimensional
CNT	Carbon Nanotube
UV	Ultra Violet
IR	Infrared
PECC	Photo Electrochemical Cell
QE	Quantum Efficiency
NW	Nanowire
FET	Field Effect Transistor
TMDC	Transition Metal Di-chalchogenides
CVD	Chemical Vapour Deposition
PLD	Pulse Laser Deposition
ALD	Atomic Layer Deposition
GB	Gain-Bandwidth
EDL	Electric Double Layer
XRD	X-ray Diffraction
FWHM	Full Width at Half Maximum
ITO	Indium Tin Oxide
FTO	Fluorine Tin Oxide
ac	Alternating Current

dc	Direct Current
TFT	Thin Film Transistor
MIS	Metal Insulator Semiconductor
MOSFET	Metal Oxide Semiconductor Field Effect Transistor
TOS	Transparent Oxide Semiconductor
AOS	Amorphous Oxide Semiconductor
IAD	Ion Assisted Deposition
rf	Radio Frequency
LED	Light Emitting Diode
CBM	Conduction Band Minimum
VBM	Valence Band Minimum
TCO	Transparent conducting oxides
ZTO	Zinc Tin Oxide
SAND	Self Assembled Nanodielectrics
TLC	Trap Limited Conduction
MIOS	Metal-insulator-oxide-semiconductor
NVM	Non-Volatile Memory
FeFET	Ferroelectric Field effect transistor
PVdF	Poly(vinylidene fluoride)
PVdF-HFP	Poly(vinylidene fluoride co hexafluoropropylene)
NR	Nanorods
IPCE	Incident Photon to Current Conversion efficiency
SEM	Scanning Electron Microscopy
PL	Photoluminescence
CB	Conduction Band
VB	Valence Band
FTIR	Fourier Transform Infrared

UV-VIS	Ultraviolet-Visible
DRS	Diffuse Reflectance Spectroscopy
UHV	Ultra High Vacuum
OCV	Open Circuit Voltage
PE-ALD	Plasma Enhanced Atomic Layer Deposition
MTR	Multiple Trap and Release
V_{th}	Threshold Voltage
SS	Subthreshold Slope
DOS	Density of States
IGZO	Indium Gallium Zinc Oxide
TMA	Trimethyl Aluminium
IZO	Indium Zinc Oxide
DSC	Differential Scanning Calorimetry
MIM	Metal Insulator Metal
ATR	Attenuated Total Reflectance
EIS	Electrochemical Impedance Spectroscopy
SMU	Source Measure Unit
ZIS	$ZnIn_2S_4$
HMT	Hexamethylene Tetramine
PEI	Polyethylenimine
D. I.	Deionised

Abstract

The demand for flexible electronic components is increasing in portable handheld displays and communication products due to their light weight, flexibility, shock resistance, low cost and transparency. Flexible electronics on plastic substrates has been approached quantitatively utilizing amorphous silicon, organic semiconductor materials, carbon nanotubes, and nanowires. There are many studies and research on materials systems and processes that are used to fabricate devices that can be employed in a wide variety of applications such as flexible flat-panel displays, sensors, photovoltaics, photodetectors and electronic paper. Wide range of materials is being investigated starting from polymeric semiconductors to nanotubes to transparent conducting metal oxides in the context of these applications.

In this thesis we have mainly studied two device systems, namely photodetectors and field effect transistors, fabricated by solution processible routes. The first work deals with novel photodetector designs using some unique features and properties of the interfaces between one or two dimensional inorganic semiconductors and hydrogel. In addition to the explorations of device performance, experiments have been performed to establish the physical mechanisms of these photodetectors. The second work deals with metal oxide based transistors. The nanocomposite of PVdF-HFP/clay is used as dielectric in nonvolatile memory transistor. Finally the transport studies were done on combustion synthesized indium oxide transistors.

Chapter 1 gives a brief introduction of concepts, physical properties, materials and devices dealt in the entire thesis.

Chapter 2 gives a general outline of the instruments and methods used for the characterization of the materials and devices.

Chapter 3 includes the experimental methods, results and analysis of the work done on the photosensing property of zinc oxide nanorods forming an interface with a shape conforming hydrogel (agarose gel). The hybrid device works as highly efficient photodetector that shows strong response in the UV as well as partial visible range. It is

shown that the gel layer remarkably improves the response time and spectral responsivity of the ZnO(NR)-gel-Pt system in comparison to ZnO(NR)-Pt system. The UV response gets stronger by a factor of 1000 with the application of the gel.

Chapter 4 includes the fabrication of a highly efficient self-powered UV-Vis photo-detector based on $ZnIn_2S_4$ nanopetal film with surface-dispensed agarose gel. The $ZnIn_2S_4$ nanopetals films are grown on FTO-coated glass hydrothermally. Remarkably, the zero bias $ZnIn_2S_4$/gel hybrid photoresponse is 100 times stronger as compared to the only $ZnIn_2S_4$ device response (at -1.5 V bias) without significant degradation in the response time. We have discussed the possible operating mechanisms.

Chapter 5 includes the experimental methods, results and analysis of the work done on the nonvolatile memory (NVM) transistor using zinc oxide (ZnO) as the channel and Poly (vinylidene fluoride-co-hexafluoropropylene) (PVdF-HFP) clay nanocomposite as the gate dielectric.

Chapter 6 includes the presentation of experimental details, results and analysis of the work done on the transport studies on solution processible and low temperature synthesized In_2O_3 thin film transistors (TFTs) on Al_2O_3 and SiO_2 as dielectrics.

The **Chapter 7** summarizes the work described in this thesis by presenting the salient features of the work. Possible avenues for future investigations are also outlined.

Table of Content

CHAPTER 1

Introduction

This chapter gives a brief introduction of concepts, physical properties, materials and devices dealt in the entire thesis. The devices namely photodetector, gel based photodetector and field effect transistor are discussed. The focus is more on definitions and descriptions rather than on derivations.

1.1 Motivation

Semiconductors are the building blocks of modern electronic devices replacing thermionic devices (vacuum tubes) in most applications.[1,2] Thermionic devices operate in high vacuum, in contrast semiconductors devices has no such requirement thus enabling the miniaturization of electronic devices. Semiconductors are interesting because their carrier concentration can be modulated over several orders of magnitude by doping, temperature, electric field, light, heat etc. Semiconductor devices can be manufactured both as discrete devices or integrated devices. Discovery of semiconducting devices led to the miniaturization of modern electronic devices. The integration and miniaturization of semiconductor devices has been happening over years following the Moore's law.

The semiconductor industry is basically ruled by silicon. Alongside, a lot of research has been focusing on alternate semiconductors such as organic[3-5] and metal oxide semiconductors.[6-9] These materials can be deposited on large area and flexible substrates using physical vapour deposition routes or solution processing routes making them ideal candidates for large area flexible and/or transparent electronics.[3-9]

An interesting property of a semiconductor is photoconductivity i.e. the change in electrical conductivity due to incident light. Photoconductivity involves absorption of radiation, generation of carriers and their concurrent transport.[1,10] The change in conductivity depends on the number of carriers generated per incident photon and the mobility of the carriers. The duration for photoconductivity changes depends on the carrier lifetime and the trap-states present in the material. Photodetectors and photovoltaic devices are based on this property of semiconductor.

In recent years transparent conducting oxides (TCOs) exhibiting high mobility and optical transparency have attracted a lot in interest as active channels in unconventional transistors. The first transparent thin film transistor based on ZnO was demonstrated in 2003 by Carcia *et al*.[11] An interesting property of amorphous and polycrystalline materials over their single crystalline part is that they can be deposited on large area (including on flexible substrate) as uniform film even at room temperature.[6] They can be deposited either using vapour deposition methods as Pulse Laser Deposition

(PLD), Chemical Vapour Deposition (CVD), Atomic Layer Deposition (ALD), radio frequency (rf) Sputtering etc; or solution routes such as spin coating, dip coating, inkjet printing etc.[9]

This thesis is divided into two sections: The first section deals with some novel photodetector designs developed in this work using the interface of one or two dimensional inorganic semiconductors with a hydrogel and performing experiments to establish the physical mechanisms on which these detectors function. The second section deals with solution processed metal oxide transistors. All the devices have been made by solution-processing techniques, which enable their use in ultra-low-cost applications.

1.2 Photodetectors

Photodetectors are semiconducting devices converting optical signals into electronic signals.[1,10,12] A photodetector generally involves three processes a) generation of carriers in response to illumination, b) carrier transport and in some cases multiplication (by means of current gain mechanism), and c) the current transport into the external circuit as output signal.

1.2.1 Classification of Photodetectors

Depending on the wavelength range a photodetectors can be broadly classified into a) Ultra-Violet (UV), b) Visible and c) Infrared or IR photodetectors..

1.2.1.1 UV-Photodetector

The ultraviolet radiation covers the 10 nm - 400 nm wavelength region of the electromagnetic spectrum. Ultraviolet (UV) detectors are used in scientific research, industry, and military applications, and must be either “visible blind” or “solar blind” to detect a weak UV signal in the presence of the strong ambient light. They have extensive use in areas such as the detection of UV flames for combustion control, surveillance of rockets and intercontinental ballistic missiles, secure space-to-space communication, detection of UV scintillation for medical imaging, monitoring of pollutants like nitrous

oxide and sulfur dioxide in the ionosphere, in space-based instrumentation for UV astronomy, and in UV photolithography for semiconductor processing. Pollution detection generally relies on UV spectroscopy, with detectors measuring the strength of absorption lines for pollutants such as sulfur dioxide, nitrous oxides, and ozone.[10]

For example the UV detectors can detect UV emissions from flames in the presence of hot backgrounds such as infrared emission from the hot bricks in a furnace. This provides an excellent flame on/off determination system for controlling the gas supply to large furnaces and boilers. Flame safeguard and fire control are just two of the various possible applications for the UV detectors.

Ultraviolet astronomy is a major field that got accelerated when telescopes could be placed above the Earth's UV-absorbing atmosphere. UV photodetectors are used in UV phototube or UV camera that contains a lot of information about the solar system as well as galaxies. For example, UV images have revealed the aurora of Jupiter caused by a radiation belt that is much more intense than the Earth's own Van Allen Belts.

1.2.1.2 Infrared Photodetector

The infrared (IR) radiation covers the 750 nm - 1000 µm wavelength region of the electromagnetic spectrum. The IR photo detectors have numerous applications in industry, agriculture, medicine (medical thermograph), science (survey of soil, water resources, volcanos, metrological phenomena etc.), communication, remote sensing, security (detection of heat leakage from furnace, fire detection, intruder detection) etc. They can be thermal (wavelength independent) or quantum (wavelength specific) type. They can be used as flame monitors for both the UV and infrared radiation that are emitted from flames. One important application is also infrared imaging or night vision. Various materials such as PbS, PbSe, HgCdTe, Ge, InGaAs, InAs etc. are used in IR photodetectors. Photodiodes sensitive to IR wavelengths are used for fiber optic devices, or for implementing simple commands to change channels, or switch a VCR or TV on or off. Even remote controls, however, are increasing in sophistication. The cordless mouse devices for PCs, for example, use detectors that measure the relative strength of signals to determine mouse orientation and position.[12]

Fundamental Modes of Photodetector Operation:

Here we focus on Photodetector operating in two modes:

1. Photoconductive mode
2. Photovoltaic mode

1.2.2 Photoconductor Mechanism

A photoconductor is basically a light radiation sensitive resistor. When a photon of energy greater than the band gap strikes and is absorbed by the semiconductor it generates an electron-hole pair, which in turn changes the conductivity of the semiconductor.[1,10,12] **Figure 1.1** shows the schematic of a photoconductor.

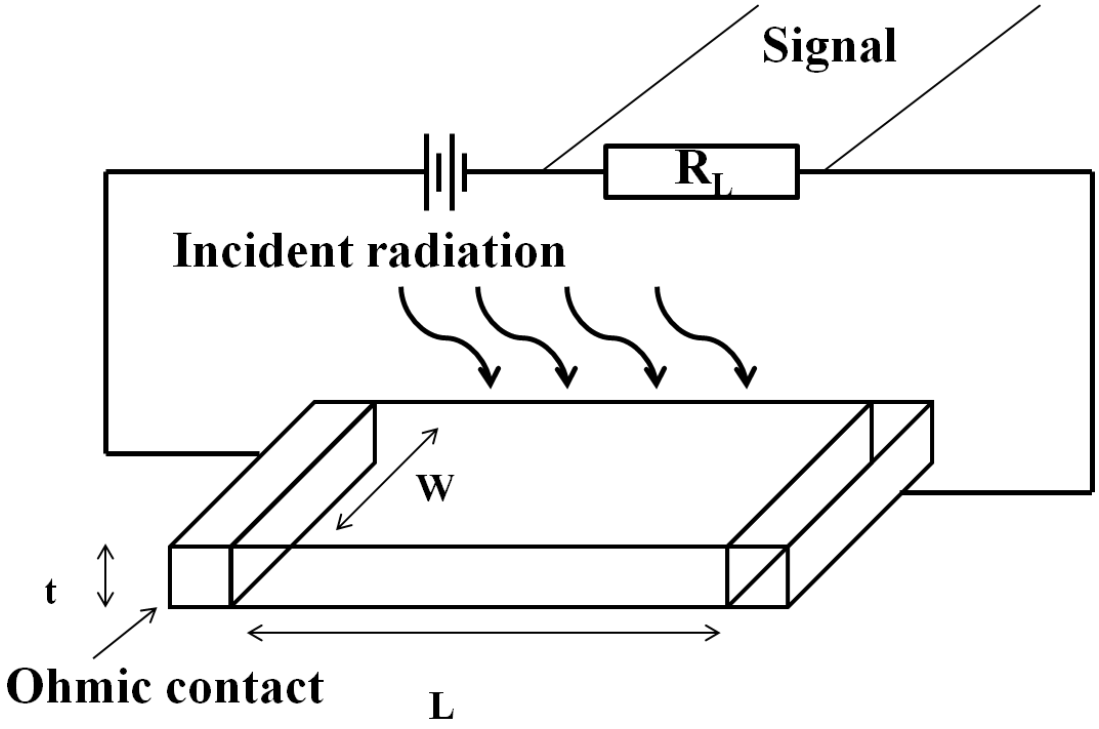

Figure 1.1: *Schematic and bias of photoconductor redrawn from ref 10*

In a semiconductor the conductivity (σ) is given by[1,10,13]

$$\sigma = ne\mu$$

Where, n is carrier density, e is electron charge and μ is mobility. In the presence of applied field $E = V/l$, where V is the applied potential applied across a photoconductor of length l, the current density is $J = \sigma E = nev$ with drift velocity ν as μE.

In the presence of illumination both the carrier density n and mobility μ change resulting in a change in the conductivity as $\Delta\sigma = e(\mu\Delta n + n\Delta\mu)$. Here, the changes in both mobility and carrier density depend on time.

The photocurrent is given by $J_{pc} = e(\mu\Delta n + n\Delta\mu)E$

In most semiconductor Δn >> Δμ, therefore the photocurrent is given as $J_{pc} = e\mu\Delta nE$

The photoconductive gain is also given as,

$$g = \frac{\tau}{l^2/\mu V_b} = \frac{\tau}{t}$$

Where, τ is the electron life time and t is the electron transit time between the two electrodes.

In these type of photodetectors generally a single carrier type (either electron or hole) is transported i.e. they are unipolar. The other type of carrier is trapped.[14] These traps serve to delay band-to-band recombination and to impede the extraction of the trapped carrier, a condition necessary for photoconductive gain. Due to the trapping of one carrier type the other charge carrier type can circulate many times in the external circuit before recombination leading to high gain.

In the presence of light the conductivity of photoconductor increases for duration known as persistence time.[14] The persistence is determined by the electron–hole pair recombination time, and this is prolonged with the aid of traps. These types of photodetectors have high responsivity (defined as the photocurrent flowing through the detector per incident optical power.) but at the same time suffer from long response time. The high responsivity photodetectors simplify the function of read-out circuits; at the same time the long response time reduces the bandwidth.

1.2.3 Photovoltaic Mechanism

In such detector systems the electron hole pair is separated by the electric field created by a p-n junction, a Schottky contact or a metal-insulator-semiconductor capacitor which leads to photocurrent in the external circuit.[10,14] It requires two materials; one of them has to be semiconductor while the second one could be a metal or another semiconductor. Due to the difference in the Fermi levels of the two materials at the interface, an in-built field is developed. This field at the interface makes the electron and holes to move in opposite direction. The quantum efficiency of such photodetectors cannot be higher than 1. These types of photodetector have a fast response time.

1.2.3.1 Self Powered Photodetectors

In order to get reasonable detectivity most of the photodetectors need certain applied potential (1V-10V) which therefore requires a constant use of batteries (power). This makes the overall circuitry heavy and uneconomical in the current energy scenario. The 'self-powered' photo-detectors which are either integrated with an energy harvesting unit such as biofuel cell or piezotronic circuitry, or which can generate self-sufficient potential for their operation have attracted considerable attention of scientists and technologists lately. The self powered photodetectors enhances the adaptability of the device as well as reduce the size and weight of the systems.[15] These self powered photodetectors are of two types:

- Using the photovoltaic mode
- Devices coupled to an energy harvester.[16]

The self powered photodetectors working in photovoltaic mode are powered by open circuit voltage generated at the interface. They have fast response as well as high photosensitivity. Various self powered Schottky,[17] p-n junction[18,19] or photo electrochemical cell (PECC)[20,21] type photodetectors have thus been reported. For instance, Bie *et al.* have demonstrated a self biased ZnO/GaN p-n junction type photodetector.[18] The device shows photovoltaic effect with short circuit current of 5×10^4 mA/cm^2 and an open circuit voltage of 2.7 V. The device has fast response rise time of 20 μs and decay time of 219 μs.

1.2.4.2 p-n Junction Photodiode

In these detectors the built-in potential causes the electrons and holes to move in opposite directions. When photons with energy greater than the band gap are incident on the device, electron hole pairs are generated. The electron hole pairs generated away from the junction diffuse to the junction where the in-built potential separates them. This way a photocurrent is generated which shifts the current–voltage characteristic in the direction of negative or reverse current. **Figure 1.2** shows the schematic and photocurrent of a p-n junction photodetector. For high speed operation, the depletion region needs to be thin so that the transit time is less, whereas high quantum efficiency requires thick depletion region so that more photons are absorbed. The response time of photodiode is determined by the diffusion of carriers, drift time of carriers in the depletion region and the capacitance of the depletion region.[1,10,14]

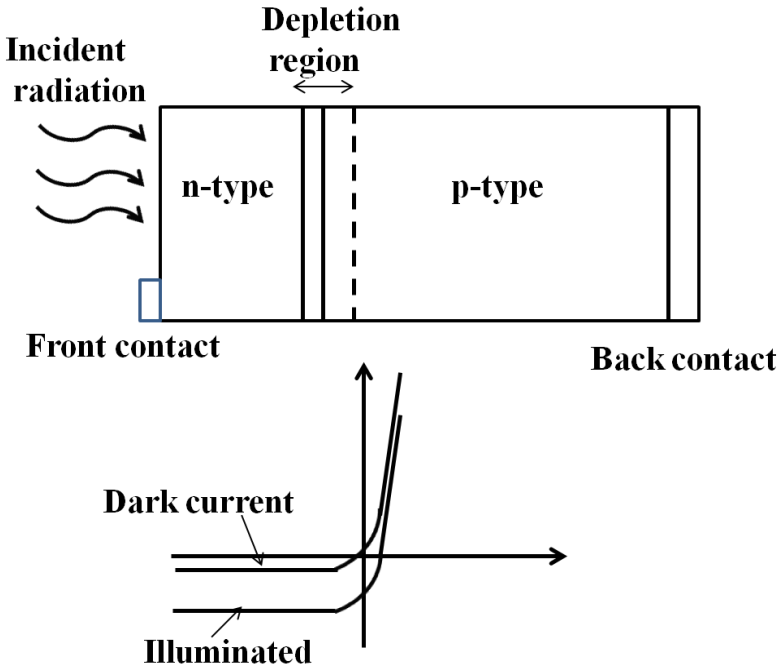

Figure 1.2: *Schematic of p-n junction photodetector with I-V characteristics in dark and illumination. (Redrawn from ref 10)*

1.2.4.2 Schottky Barrier Photodetector

When a metal is making intimate contact with semiconductor then the Fermi level of the two should match at the equilibrium. If there is a difference in the Fermi level of two, then charge flows across the interface causing band bending at the interface and leading to barrier formation known as the Schottky barrier. According to Mott-Schottky, this barrier at the interface leads to the rectifying property at the metal-semiconductor interface. When photon of energy less than band gap but greater than the barrier energy i.e. $E_g > h\nu > q\varphi_B$ is incident on the photodetector, the photo-excited electrons jump from the metal into the semiconductor. Whereas when photons with energy greater than E_g are absorbed by the semiconductor, they generate electron-hole pairs which can be separated by the in-built potential.[10,17,22] The difference between the Schottky contact and p-n junction is that the current in former is due to majority carriers whereas in later is due to minority carriers.

1.2.5 Figure of merit to characterize a photodetector

1. Responsivity[14] (R_λ): It is defined as the photocurrent flowing through the detector per incident optical power.

2. Dark Current: The current flowing through the photodetector in dark. In an unbiased photodiode at steady state, this is equal to zero.

3. Quantum efficiency (QE or η): It represents the number of electron-hole pairs generated per incident photon. i.e. the ratio of photocurrent (in electrons per second) to photon fluence incident on the device (photons per second). QE is related to responsivity by the photon energy as

$$R = QE/E_{photon}$$

Where, E_{photon} is measured in eV. In a photoconductor, the term QE is sometimes used synonymously with absorbance.

4. Gain (g): In a photoconductor, this represents the ratio of photocurrent to the no. of photon absorbed. This signifies how well the generated electron-hole pairs are used to generate the current response of a photodetector. The spectral responsivity in terms of gain is also given as,

$$R_\lambda = \frac{\lambda\eta}{hc} qg$$

Where, R_λ is responsivity, λ is wavelength, q is electron charge, h is Planck's constant, c is velocity of light, η is quantum efficiency.

5. Detectivity (D): It determines the signal to noise ratio of a photodetector as,

$$D = R_\lambda \left(\frac{A_0 \Delta f}{I_n}\right)^{\frac{1}{2}}$$

Where, Δf is the frequency bandwidth, A_o is the optical area and I_n is the noise current of the photodetector.

1.2.6 Photodetector based on nanostructures

Currently there is growing interest in nanostructured materials for potential applications in the fields of advanced electronics and optoelectronics. Nanostructures can be divided into 0D (dimensional), 1D or 2D based on their shape and morphology. Nanostructured materials such as quantum dots[14], nanorods[22], nano-ribbons, 2D forms (graphene, MoS_2, GaS etc.)[23-25] support novel effects emanating from quantum phenomena as well as enhanced surface related effects. Moreover, due to very high surface to volume ratio, these systems are easily accessible to property engineering through surface functionalization/modification. These low dimension nanostructures can be easily integrated into circuits using lithography.[26]

1.2.6.1 1D nanostructures

The observation of high photoresponsivity in semiconductor nanowires (NWs) is attracting growing interest for their potential use in highly-integrated optoelectronic devices, hybrid organic–inorganic solar cells, optical interconnects, and transceivers etc. Indeed, in the context of photo-response, which is the subject of the present work, novel

effects and mechanisms have been reported with unprecedented levels of response through surface band bending and charge separation scenarios.[13-15]

Light scattering and absorption enhancement in vertical nanowire array:

In nanowires (NWs), when the physical dimension in comparable to the incident light wavelength then there is light scattering.[13] In open configurations the NWs arrays are surrounded by air which has low dielectric constant. Effective-medium models predict a significant reduction of the reflectance of vertical NW arrays over the entire spectral range, due to the low effective refractive index of the array of NWs surrounded by air. It was found that, for typical NW diameters around 50 nm, diffuse multiple light scattering dominates the optical properties. Depending on the ratio between the absorption and scattering mean free path, absorption losses can be strongly suppressed in the NWs arrays. The scattering mean free path can be controlled by varying the NW diameter or by infiltration with refractive index matching materials). This has obvious implications for the design of efficient NW absorbers in NWs-based photovoltaic cells, or in determining the spectral response of NW photodetectors.

1.2.6.2 2D nanostructures

With the discovery of graphene and its remarkable properties (electrical, thermal conductivity, high mobility, transparency etc.), there is a renewed interest in two-dimensional materials with unique electronic and optical attributes.[27,28] Various transition metal chalchogenides, 2D compounds (e.g., BN, Bi_2Te_3, MoS_2, WS_2 and Bi_2Se_3) have similar 2D structures because of strong in-plane bonding and weak out-of-plane interactions, allowing their exfoliation into two-dimensional layers of single unit cell thickness. In contrast to graphene, metal chalchogenides have a band gap and they can be used for promising interesting new FET and optoelectronic devices. The relatively high earth abundance of transition metal dichalchogenides (TMDCs) and their direct band gaps in the visible range make them attractive as the light-absorbing materials in alternative thin-film solar cells. Thin films of MoS_2 and WS_2 are photosensitive, and a phototransistor made from a single layer of MoS_2 has shown its potential as a photodetector. Hu *et al*. have demonstrated GaS[24] and GaSe[25] based photodetector on

both rigid and flexible substrates. These photodetectors have high responsivity, high quantum efficiency and fast response time.

Photoconductive Gain

Nanowires, due to their high surface to volume ratio, have a large density of trap states at their surface.[11] These trap states lead to Fermi level pinning at the surface; as a result a depletion layer exists at the surface which causes the physical separation of the electron-hole pair. This physical separation of charge carriers increases the carrier lifetime. The dark and photo current thus depend strongly on the dimension and the geometry of the nanostructure.

Photoconductive gain is defined as the number of charge carriers that passes through the photoconductor electrodes per second for each photon absorbed per second. The photoconductive gain is given by,

$$G = \frac{N_e}{N_{ph}} = \frac{\tau}{\tau_T}$$

Where, τ is the carrier life time and τ_T is the carrier transit time.

Nanostructured photoconductors have high gain due to high carrier lifetime due to the trapping of one type of carriers at the surface combined with a fast transit time. A photoconductor with internal gain can be considered as an equivalent current amplifier, in which the bandwidth B for a response time τ is

$$B = \frac{1}{2\pi\tau}$$

The gain-bandwidth (GB) product of the photoconductor, therefore, is given by:

$$GB = \frac{1}{2\pi\tau_T}$$

Here, the large photoconductive gain is achieved at the expense of dynamic response time.

Group II–VI semiconducting compounds (sulfides, selenides, and tellurides) are widely employed in optoelectronic applications due to their direct bandgap and a wide coverage of band gap energies. These are basically used in visible and infrared photodetectors. Metal oxides on the other hand are being increasingly exploited as UV photodetector and transparent conducting electrodes due to large band gap.

1.2.7 Semiconductors used for photodetector in the thesis

1.2.7.1 Zinc Oxide (ZnO)

Zinc oxide is an important metal oxide with wide application range in device systems such as such as transistors, optoelectronics, sensors and piezo-electronic transducers. Due to its wide band gap of 3.37 eV, exciton energy of 60 meV and ability to grow into various morphologies it is widely investigated as visible-blind UV-Photodetector.[10,11,29] However, due to oxygen vacancy forming deep level donor state ZnO is known to show defect related peak in photoluminescence (PL). This can be used to tune the spectral sensitivity of ZnO into the visible region. Usually in a ZnO based photodetector the photon detection is explained in terms of adsorption and desorption of molecular oxygen. In dark, the oxygen molecules get adsorbed on the ZnO surface taking the free electron and creating depletion at the ZnO surface. This depletion of electron decreases the conductivity of ZnO under dark condition. ZnO can be partly or fully depleted depending on the ZnO film thickness. When the ZnO film is illuminated by light, electron-hole pairs are generated. The holes have a tendency to move to the surface due to band bending at the surface. These light generated holes release the oxygen from the surface. In this process the photo-generated holes get trapped leaving behind free electrons. The photo-generated electron-hole pairs upon UV illumination will be effectively separated by this local electric field, which reduces the recombination rate and increases the carrier lifetime and density. As a result, oxygen can be discharged and desorbed at a faster rate. Usually ZnO based photodetector shows large photoconductivity but slow response time. To further increase the sensitivity of ZnO based photodetectors it is functionalized by various polymers.

1.2.7.2 Zinc Indium Sulphide ($ZnIn_2S_4$)

It is a layered ternary chalchogenides from the family of ternary compounds AB_2X_4 with band gap of around 2.3 eV. It is an n-type semiconductor. Due to its strong absorption in the visible region, currently it is being extensively investigated for solar energy applications such as solar cell, photocatalysis etc.[30-32] It is a photo-conducting material with applications in electrochemical recording and photo-variable capacitor. Earlier studies on single crystal $ZnIn_2S_4$ indicate exponential distribution of traps in the band gap. These traps are caused by acceptor like levels.[33] These acceptor-like centers are explained by the presence of singly and doubly charged impurity centers such as Zn^{2+} vacancies or Zn^{2+} ions occupying the In^{3+} sites.

1.2.8 Semiconductor Electrolyte Interface

When a semiconductor forms an interface with an electrolyte, the two systems try to attain equilibrium by matching the Fermi level of the semiconductor with the redox potential of the electrolyte with a flow of charge across the interface.[34-36] The excess charge on the metallic/semiconducting electrode is like a surface charge separated from the ionic counter charge in the electrolyte. Unlike a metal, in a semiconductor this excess charge penetrates inside the semiconductor, leading to the formation of a space charge region in the semiconductor. At the same time counter ionic charges form an electric double layer in the electrolyte. This is known as Helmholtz double layer. Since these counter ions are not rigidly fixed to the surface, due to thermal energy there is an exponential decrease in potential from the surface leading to the development of the Stern layer.

For a n-type semiconductor as shown in **Figure 1.3** one of the following conditions can exist at the semiconductor electrolyte interface.

a. If the Fermi level of semiconductor and redox potential of the electrolyte lie at the same energy then it is known as the flat band potential. There is no excess charge at the interface and the bands are flat. Within the semiconductor the positive

charge of immobile ions are balanced by the mobile electrons of the semiconductor.

b. For a potential negative to flat band potential for n-type semiconductor there is an excess of the majority charge carrier (electrons) in this space charge region, which is referred to as the accumulation region.

c. For an n-type semiconductor even under open circuit condition (zero applied bias) the Fermi level of the semiconductor usually lies above the redox potential of the electrolyte. The electrons flow from the semiconductor to the electrolyte leading to an upward band bending in the semiconductor causing depletion of charges at the interface. Depletion region arises at potentials positive of the flat-band potential for an n-type semiconductor.

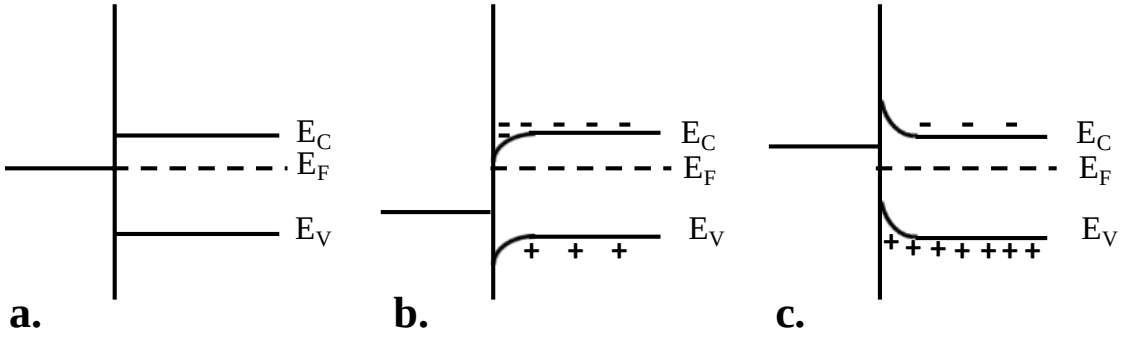

Figure 1.3: *Schematic showing the space charge layers in an n-type semiconductor in contact with an electrolyte.*

The charge transfer ability of the semiconductor electrolyte interface depends on whether there is accumulation or depletion layer at the interface. In the presence of illumination electron hole pair will be generated in the semiconductor. The junction capacitance at the semiconductor electrolyte will help in the separation of charge carriers. The charge distribution at the semiconductor electrolyte interface can be studied through differential capacitance or impedance spectroscopy. **Figure 1.4** shows the capacitance distribution at the semiconductor-electrolyte interface. The semiconductor-electrolyte interface is modeled as a series of three types of capacitances namely Helmholtz

Capacitance C_H (EDL), capacitance of the diffuse layer of charges in the electrolyte C_D and Space charge capacitance of the semiconductor C_{sc},

$$C_T = C_H + C_D + C_{sc}$$

Since, in a series combination of capacitors the total capacitance is determined by the smallest one, it is C_{sc} in this case.

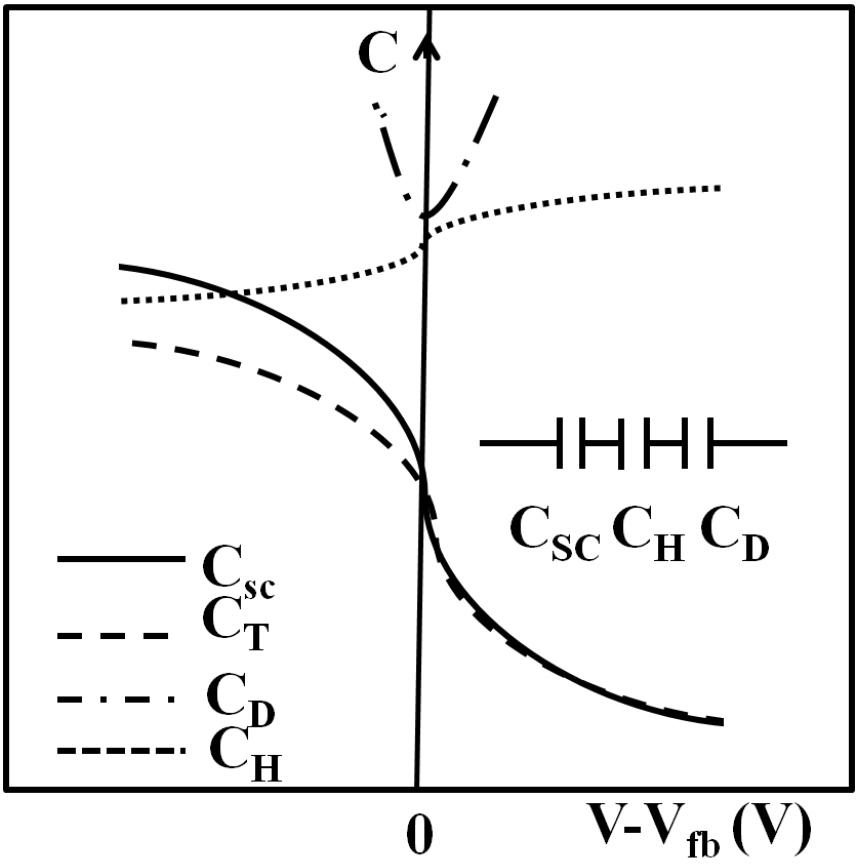

Figure 1.4: *shows the dependence of capacitance component at n type semiconductor/electrolyte interface as function of potential (redrawn from ref 36)*

1.2.9 Capacitance-Voltage (C-V) measurement

The barrier height formed at the interface of semiconductor with metal/electrolyte can be determined by C-V measurements. In C-V measurement a small *ac* signal is superimposed on the *dc* bias. As a result one kind of charges is induced at the

metal/electrolyte surface and the opposite charges on the semiconductor. The C-V relation is given by,

$$C = \frac{|Q_{sc}|}{\partial V} = \sqrt{\frac{q\varepsilon_s N_D}{2(V_{bi} - V - {kT}/{q})}}$$

When $1/C^2$ is plotted against the applied voltage V, a straight line is thus obtained. This plot is known as a **Mott-Schottky plot.** The intercept on the voltage axis is the barrier height.

From the slope the carrier density can be calculated as

$$N_D = \frac{2}{q\varepsilon_s}\left[\frac{-1}{d\left({-1}/{C^2}\right)/dV}\right]$$

It can also be used to study deep impurity level in the semiconductor. This is done by taking C-V plots at different frequencies.

1.3 Metal Oxide Field Effect Transistors

Thin film transistor (TFT) was discovered in 1925 by J.E. Lilienfeld and O. Heil [9,37] and patented in 1930. Metal oxide semiconductors have high carrier mobilities, wide band gaps, broad transparency windows, tunable doping levels, and amenability to room-temperature film growth. The first TFT was demonstrated by Weimer in 1962. He used a thin film of polycrystalline CdS as channel in a metal-semiconductor field-effect-transistor.[1,38]

1.3.1 Device Architecture and Operation

TFTs are basically three terminal devices. The basic operating principal of TFT is the modulation of current flowing through a semiconductor by the field applied across the

dielectric. In TFTs a dielectric in inserted between the semiconductor and the gate electrode. The term field effect implies the capacitive injection of carriers in the semiconductor by the semiconductor/dielectric interface which results in modulation of current across the semiconductor.

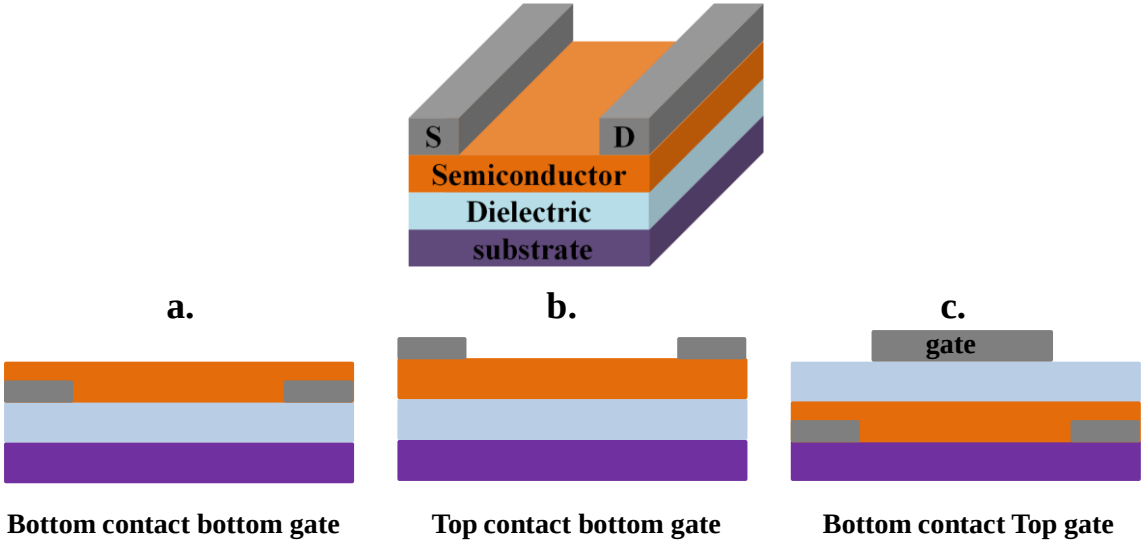

Figure 1.5: *Schematics showing different TFT structures, depending on the position of the gate electrode and source drain electrodes relative to the semiconductor*

Figure 1.5 shows the common TFT configurations: a) Bottom contact bottom gate b) Top contact bottom gate and c) top gate bottom contact, depending on whether the gate electrode is on top or bottom of the structure.

1.3.2 Metal Insulator Semiconductor (MIS) Structure

Figure 1.6 a) show the energy band diagram ideal of MIS at zero applied bias i.e. at zero bias the work function of metal is aligned to the Fermi level of semiconductor. This is the flat band condition. Depending on the bias applied, three conditions can exist in the MIS system.[1,3] In case of n type semiconductor:

- When positive voltage (V > 0) is applied to the metal, the conduction band bends downward and gets closer to the Fermi level. This bending causes accumulation

of electrons near the semiconductor surface. This is the case of accumulation layer formation. This is depicted in **Figure 1.6** b)

- When small negative voltage is applied to the metal (V < 0) the bands in semiconductor bend upward and the electrons are depleted near the semiconductor interface. This is the case of depletion layer formation. This is depicted in **Figure 1.6** c)

- When a large negative voltage is applied to the metal the band bends even more upwards. Now the density of minority carriers (holes) is higher at the semiconductor interface than the electron. This is the case of inversion layer formation.

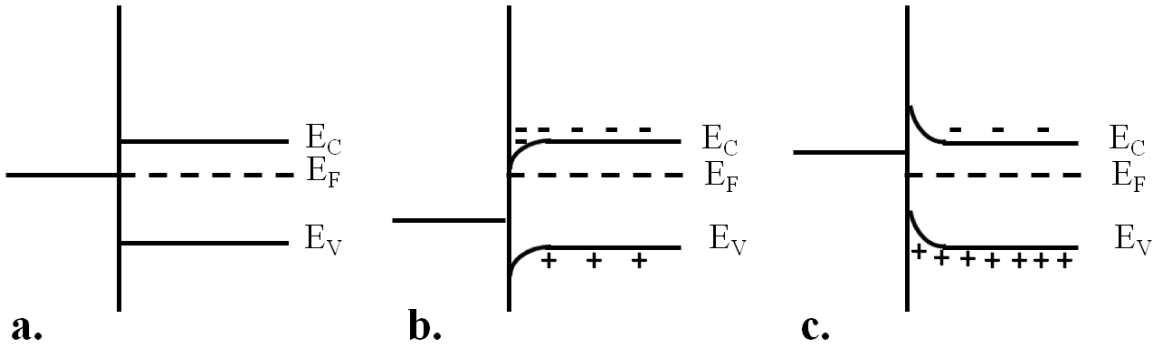

Figure 1.6: *The energy band diagram of Metal-insulator-semiconductor in case of n type semiconductor under different applied gate voltage condition. E_C, E_F and E_V represent respectively the valence band, Fermi level and conduction band of semiconductor a.V_g = 0V b. V_g > 0V c. V_g< 0V.*

In silicon metal oxide semiconductor field effect transistors (MOSFETs) all the three conditions can exists but in the case of metal oxide semiconductors or organic semiconductors TFTs can work only in accumulation and depletion modes. This is due to the fact that MOSFETs have p-n junctions in the source drain regions, which are absent in TFTs.

1.3.3 Working Principal of FETs

When a gate voltage is applied ($V_g > 0$ for a n-type semiconductor) it will induce electrons at the insulator/semiconductor interface that are injected from the grounded source electrode. The number of electrons accumulated depends on the applied gate voltage and insulator capacitance. There is a minimum gate voltage V_{th} below which all induced charges fill the trap states and only for $V_g > V_{th}$ mobile charges are induced in the semiconductor and contribute to the current in a field-effect transistor. That is, a gate voltage has to be applied that is higher than a threshold voltage (V_{th}) and thus, the effective gate voltage is $V_g - V_{th}$. With no source-drain voltage the charge carrier concentration in the transistor channel is uniform.

Now if a small drain voltage is applied the current will start flowing between the source and drain electrodes. The small V_{ds} creates a linear gradient of electrons from source to the drain. The semiconductor behaves like a resistance with source drain current (I_{ds}) proportional to drain voltage (V_{ds}). The transistor is in the linear region.

When the drain voltage is increased gradually (with source grounded) and it reaches $V_g - V_{th}$ the channel depth near the drain becomes zero. This is known as the pinch-off point. Beyond pinch-off the drain current remains the same with increasing V_{ds}. This is due to the formation of depletion layer near the drain [the local potential (the difference between V_g and $V_{ds)}$ near the drain is negligible]. A space-charge-limited saturation current $I_{ds,sat}$ can flow across this narrow depletion zone as carriers are swept from the pinch-off point to the drain by the comparatively high electric field in the depletion region. With further increase in V_{ds} The current $I_{ds,sat}$ remains the same only increasing the width of pinch-off region or decreasing the effective channel length.

1.3.4 TFTs obey the MOSFET equation

In a transistor the mobile charges accumulate at the semiconductor insulator interface and the total accumulated charge is given by

$$Q_{mob} = C_i(V_g - V_{th})$$

The I_{ds} is given by,

$$I_{ds} = \mu \frac{W}{L} C_i(V_g - V_{th} - \frac{V_{ds}}{2})V_{ds}$$

Where W is the channel width, L is channel length, C_i is the insulator capacitance per unit area.

In the saturation region,

$$I_{ds} = \mu \frac{W}{2L} C_i(V_g - V_{th})^2$$

In the linear region,

$$I_{ds} = \mu \frac{W}{L} C_i(V_g - V_{th})V_{ds}$$

The important device characteristics can be extracted from the output and transfer characteristics of the transistor shown in **Figure 1.7**

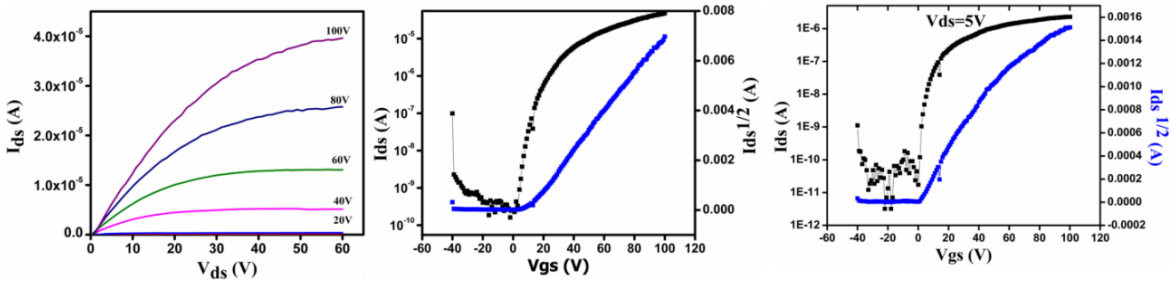

Figure 1.7: *The output and transfer curve in saturation and linear region respectively of n type In_2O_3 TFT*

1.3.5 Performance parameters

- **On/Off ratio (I_{on}/I_{off}):** It is the ratio of the maximum current (I_{ds}) to the minimum current. It represents the amplification by a transistor.

- **Threshold Voltage** (V_{th}): It is defined as minimum voltage at which the device turns on i.e. the minimum voltage at which conductive channel is formed close to the dielectric/semiconductor interface, between the source and drain electrodes. V_{th} is determined by extrapolating I_{ds}-V_g curve in linear region or $I_{ds}^{1/2}$ –V_g curve in saturation region on V axis to the intercept which gives V_{th}.

- **Sub-threshold Swing (S):** It indicates the V_g necessary to increase I_{ds} by one decade,

$$S = \left(\frac{d(\log I_{ds})}{dV_g}\right)^{-1}$$

It determines the switching behavior of the transistor. Sub-threshold slope is related to the density of trap states at the channel-dielectric interface and can be calculated by the equation,

$$N_{max} = \left(\frac{C_i}{q}\right)\left(\frac{q.Sloge}{kT} - 1\right)$$

Where q is electron charge, k is Boltzmann constant, T is temperature, C_i is the capacitance per unit area and N_{max} is the interface trap density.

- **Mobility (μ):** This is a measure of how fast a charge carrier can move in response to electric field. It determines the maximum I_{ds} and operating frequency of the transistor.

Linear mobility $\mu_{lin} = \frac{L}{WC_iV_{ds}}\frac{\partial I_{ds}}{\partial V_g}$

Saturation mobility $\mu_{sat} = \frac{2L}{WC_i}\left(\frac{d\sqrt{I_{ds}}}{\partial V_g}\right)^2$

μ is affected by several scattering mechanisms, such as lattice vibrations, ionized impurities, grain boundaries and other structural defects. On a TFT, since the movement of carriers is constrained to a narrow region close to the dielectric/semiconductor interface, additional sources of scattering should be

considered, such as Coulomb scattering from dielectric charges and from interface states or surface roughness scattering.

1.3.6 Role of Electrodes

In an FET device the charges are injected from the electrode into the channel. Unlike silicon MOSFET metal oxide based and organic TFTs have a metal-semiconductor contact. The metal semiconductor contact is treated as Mott-Schottky contact with a barrier height. If the work function of metal matches with the Fermi level of the semiconductor then Ohmic contacts is formed; otherwise the difference between the metal work function and semiconductor Fermi level defines the barrier height at the interface. This barrier height can leads to poor charge injection, leading to a contact resistance.[5] The contact resistance can be determined by,[39]

1. Measurement of the voltage drop at the electrodes with noncontact scanning probe potentiometry
2. Four probe measurement
3. The transmission line Model (In this case the resistance of transistors with different channel lengths are plotted as function of channel length, then the y-intercept of the plot of resistance versus inter-electrode separation on extrapolating to zero channel length gives the parasitic contact resistance).

Depending on the mobility of the semiconductor, the channel length and gate voltage, the contact resistance can be significant or even larger than the channel resistance; thus dominating the device performance.

1.3.7 Transparent oxide semiconductor

Today there is a growing interest towards the development of transparent metal oxide field effect transistors due to technological progress and demand related to transparent, flexible, large area display technology.[6-9] These transparent metal oxides have inherent

properties of wide band gap, broad transparency window, mechanical stress tolerance and more importantly high mobility in spite of being in the amorphous state. As is the case with organic semiconductors, transparent oxides are also compatible to large area uniformity of deposition. But unlike their organic counterparts they do not suffer from stability and low mobility issues. They are currently being used as the back panel TFT in flat panel display applications. These metal oxides have shown flexibility to wide processing temperatures. In the beginning the focus was on physical vapour deposition processes such as sputtering, pulsed laser deposition (PLD), chemical vapour deposition (CVD) and ion assisted deposition (IAD). Now various research groups are working on solution based routes to synthesize these oxides leading to highly cost effective device fabrication possibilities.

The transparent electronics research was started with ZnO (polycrystalline) TFT by sputtering reported Carcia *et al.* [11] followed by demonstration of amorphous InGaZnO by Hosono *et al.* in 2004. They have grown a-InGaZnO by (PLD) on flexible substrate as an active channel in TFT[40] with high-κ yttrium oxide as transparent dielectric and demonstrated a fully transparent TFT. The ZnO TFT due to its polycrystalline nature (grain boundary) and high density of charge carriers has issues related to the control of conductance and threshold voltage. In polycrystalline transparent semiconductors the bulk mobility is found to be higher than the field effect mobility due to scattering at the interface defining the channel. Hosono *et al*. have shown that by making oxide of 2-3 metals with varying the metal ion composition, the metal oxide can go into amorphous phase, thereby eliminating the grain boundary scattering. The amorphous oxide transistor can thus exhibit higher motilities (10 cm^2/Vs), low sub-threshold swing, low operating voltage and can be fabricated on flexible substrate. These amorphous transparent oxides have unique and superior transport properties as compared to a-Si (H) (amorphous hydrogenated silicon) and amorphous chalchogenides. By chemical doping their Fermi level can be tuned from mid band gap to the mobility band edge. These can be deposited at low temperature on large area flexible polymer substrate by physical deposition such as rf-sputtering. These are ideal candidates to make high performance TFT transistors to

drive the future back panel circuits of organic LED displays and next generation liquid crystal displays.[7]

Basically, metal oxides are ionic compounds. In ionic oxides the conduction band minimum (CBM), which is electron pathway, is composed of vacant s-orbitals of cations, whereas the valence band maximum (VBM), which is the hole pathway, is composed of the maximum contribution from oxygen 2p orbitals shown in **Figure 1.8**. The vacant s-orbitals have large spherical spread resulting in the overlap between neighboring s-orbitals in the case of transition metal oxides. This large direct overlap between the s-orbitals of the neighboring cations leads to small effective mass of electron in these oxides. SnO_2, ZnO and In_2O_3 are such transparent conducting oxides (TCOs). These oxides have their highest conductivity in crystalline phase but they have good conductivity even in their amorphous phase with electron mobilities of 5 – 40 cm^2/Vs. This mobility is far better than there amorphous silicon and organic semiconductor counterparts.

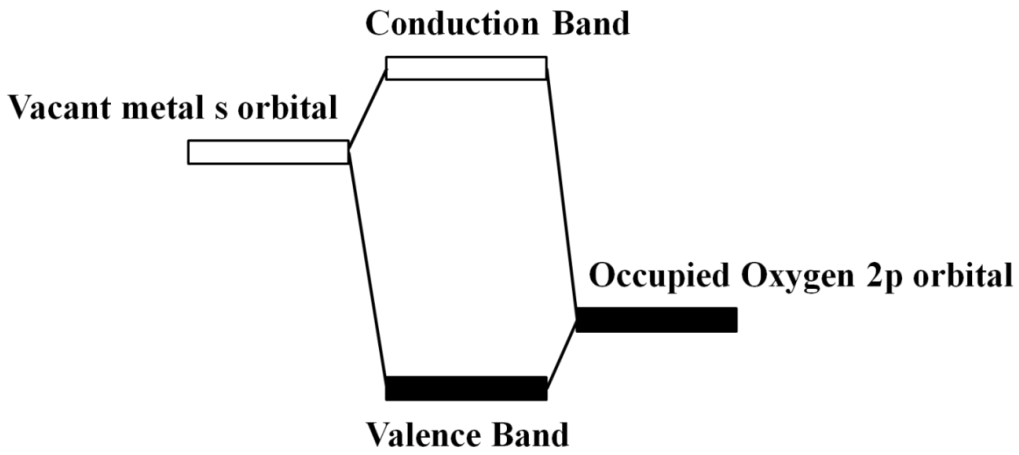

Figure 1.8: *Band structure of ionic metal oxide (redrawn from ref 7)*

1.3.7.1 Advantages of metal oxide TFTs

1. They can be processed by both physical vapour deposition and solution routes. [7] It has been shown that metal oxides deposited at low temperature by vapour routes or solution routes show satisfactory operating characteristics.

2. With their wide processing temperature window, the TFTs characteristics can be controlled by their composition and processing temperature.

3. They have large electron mobilities: They exhibit large TFT Mobilities of > 10 cm^2/V-s for appropriate chemical compositions.

4. They have low operation voltage: These semiconductors have fewer defect states in the band gap than conventional covalent semiconductors such as silicon. The low defect density allows small S values of 0.1 V/decade and low operation voltages of < 5 V.

5. Flexibility with the choice of gate insulator: Various research groups have tested a wide variety of dielectrics starting from SiO_2, SiN_x, $SiON_x$, Y_2O_3, HfO_2, Al_2O_3, $(Ba,Sr)TiO_3$, organics in general as well as hybrid dielectrics for these TFTs. They have shown good performance with these dielectrics. The choice of a gate insulator is critical for field-effect transistors including TFTs. This feature would also benefit for two reasons: a) the unipolarity of amorphous oxide semiconductor (AOS), by which only electrons are mobile and thus the valence band offset between the gate insulator and AOS is not critical; and b) the high ionic chemical bonding nature, which gives rise to fewer defects at the gate insulator/AOS interfaces.

6. They support simple electrode structure and low off current: These TFTs show good operation with simple metallic contacts when used for source and drain electrodes without increasing the off current.

7. Their films have excellent uniformity and surface flatness: They can be deposited on large area very uniformly. They show excellent uniformity and surface flatness (> 0.3 nm) owing to the amorphous structure.

1.3.7.2 Solution processable transparent metal oxides

Recently lot of efforts have been put to make these transparent high performance metal oxide semiconductors by solution routes like spin coating, roll to roll printing on flexible substrate by ink-jet, screen or gravure printing. The solution processed metal

oxides have better mobility and stability than there organic counterparts. In the case of solution processed metal oxide the solution is convenient and inexpensive to prepare by simply dissolving the metal precursor and stabilizing agent in proper proportion. Basically to make solution processable thin films the required annealing temperature is very high to reduce the precursor salt completely.[41]

Various approaches in solution processable metal oxide thin film transistor:

Colloid based process: Here the nanoparticles (10 nm) are first synthesized[41] and then a film is made by spin coating of the solution. The resulting film generally shows low mobility due to inefficient charge transport across the particles.[42] The charge transport can be improved by removing the capping agent used to synthesize the particles which improves the inter particle connectivity.

Sol gel processed metal oxide: Here, the metal oxide precursor is made by dissolving the metal salts in solvent; stabilizing agent and water.[43] The metal ions thereby form a complex with these constituents. Here, some of the water molecules surrounding the metal ions first undergo hydrolysis losing their proton and forming hydroxyl or oxy ligand. Then they undergo condensation resulting in M-O-M frame formation. The sol gel derived metal oxide films can have high mobility but the required annealing temperature is rather high around 400 ˚C. The film annealed below 400 ˚C remains inactive. Annealing leads to oxygen vacancy formation and microstructure evolution. High temperature annealing is also required to completely remove the anions of the metal salts; otherwise these impurities will hinder the metal oxide formation process as well as the charge transport in the metal oxide film.

Solution processed high performance zinc oxide based TFTs have been fabricated by direct dissolution of zinc hydroxide in aqueous ammonia solution. This solution allows for rapid metal amine dissociation and the condensation and dehydration reaction leads to the formation of ZnO nanocrystalline film at 140 ˚C by microwave assisted annealing.[44] The TFT were fabricated by using PECVD grown SiO_x dielectric and the devices were shown to withstand several bendability, rollability, wearability, and foldability tests.

Zinc tin oxide thin film transistors were fabricated by dissolving zinc acetate and tin acetate in methoxy-ethanol (0.75 M) and adding equimolar ethanolamine as stabilizing agent. The TFTs were fabricated by spin coating the solution on SiO_2 coated Si. Annealing such films at 500 ˚C, led to FETs that showed field effect mobility of 1.1 $cm^2V^{-1}s^{-1}$ and an I_{on}/I_{off} ratio of 10^6 .The electrical characteristics of the ZTO FET were shown to be dependent on the Sn concentration.[43] The same group has fabricated ZTO thin film transistors by ink jet printing of the same solution.[45]

In amorphous metal oxide semiconductors oxygen vacancy is the main source of free or mobile charge carriers. To obtain high mobility and high performance transistor (low sub threshold swing) one requires optimization of the oxygen content. Effects of doping of the metal oxides with different metal ions such as Ga, Hf, Zr and Yr have been studied. These metals act as oxygen vacancy suppressors and decrease the off current of the thin film transistors. For example, in the case of gallium the Ga-O bond is stronger than In-O or Zn-O bond, therefore the doping of Ga decreases the oxygen vacancy concentration. This decreases the carrier density and increases the stability of the device. The role of gallium doping on processing temperature of InGaZnO has also been studied and it was found that the inclusion of Ga decreases the processing temperature while indium increases the mobility but limits the low processing temperature for the film formation. [46] Effect of aluminum addition to indium tin oxide semiconductor is shown to enhance the performance of the transistor.[47]

Kim *et al*. have fabricated solution processable In-Sn-O (ITO) with In/Sn ratio and annealing temperature compatible with flexible substrate on SiO_2 showing mobility of 2 $cm^2V^{-1}s^{-1}$ and I_{on}/ I_{off} ratio of 10^4. In the same work they have used self assembled nanodielectrics (SAND) as dielectric and obtained mobility of 10-20 $cm^2V^{-1}s^{-1}$.[48] The ITO solution was made by dissolving the metal chloride salts in methoxy-ethanol and ethanolamine as stabilizing agent. Then spin coating the solution and annealing the resultant film at 200 - 250˚C led to the desired oxide film. The same group have synthesized solution-processed Zn-In-Sn-O thin film transistor.[49] They have fabricated solution processable In_2O_3 TFT using SiO_2 and high κ organic self assembled nano-dielectric (SAND) as the dielectric layer.[50] The In_2O_3 films were obtained by spin coating

Indium chloride solution in methoxy ethanol and ethanolamine and heating in a tube furnace at 400 ˚C in air for 10 minutes. On SAND as dielectric the TFT shows saturation mobility of 43.7 $cm^2V^{-1}s^{-1}$ and I_{on}/ I_{off} ratio of 10^6.

Chemically assisted annealing protocol to obtain low temperature processed metal oxide films has also been devised. Kim *et al.* have used urea or acetylacetonate as fuel and metal nitrate as oxidizing agent to combustion-synthesize metal oxide films at low temperature. The self generating heat due the local exothermic reaction taking place during the metal oxide formation eliminates the need of high external heat supply. This self generating heat converts the metal precursor into corresponding metal oxide at low processing temperature.[51] The metal nitrate as oxidizing agent reduces the probability of coke formation. They have synthesized semiconducting In_2O_3 by annealing at 200 ˚C on SiO_2 giving mobility of 1 $cm^2V^{-1}s^{-1}$. Complete solution processed FET has been fabricated combining low temperature combustion synthesized In_2O_3 along with low temperature synthesized Al_2O_3 as the dielectric. This TFT shows mobility of 13$cm^2V^{-1}s^{-1}$. The same TFT was also fabricated on flexible polymer substrate by printing the device which shows mobility of 6 $cm^2V^{-1}s^{-1}$.

The hydrolysis of metal alkoxides precursor based ‘sol gel on chip’ methods have also been developed to obtain low temperature processed metal oxides for high mobility thin film transistors.[52] Whenever a metal alkoxide is exposed to humid atmosphere hydrolysis and condensation occur; there is transfer of proton from water to the bound alkoxide ligand followed by elimination of the protonated ligand resulting on the formation of M-O-M framework at low temperature. The hydrolysis can be achieved by putting an aqueous catalyst (acid or base) to metal alkoxide before the film formation. Undesirable and uncontrolled precipitation can occur due to high reactivity of metal alkoxides. In situ heating hydrolysis annealing overcomes this drawback as here the hydrolysis process is directly applied on the surface of the film to make M-O-M framework at low temperature to synthesize the metal oxide. This approach was used to synthesize Indium zinc oxide (IZO) TFT over a temperature range of 210-280 ˚C showing mobility of 4 - 12 $cm^2V^{-1}s^{-1}$.

Low temperature solution processed Indium oxide thin film from indium chloride salt has also been made.[53] Indium chloride solution in acetonitrile is first made and then ethylene glycol is added to it. Ethylene glycol is shown to improve the film quality. The In_2O_3 film annealed at 500 ˚C shows mobility of 55.26 $cm^2V^{-1}s^{-1}$ with I_{on}/ I_{off} of 10^7. By annealing the spin-coated film in O_2/O_3 atmosphere at 200-300 ˚C yields mobility of 22.16 $cm^2V^{-1}s^{-1}$ with I_{on}/I_{off} of 10^6.

1.3.8 Gate Dielectrics

The overall performance and stability of transistor is greatly dependent on the dielectric used.[5,9] Generally to develop a good dielectric with low leakage and high breakdown voltage high temperature processes are required.[6] High temperature promotes the growth of dense film with minimum defects. One of the important challenges for metal oxide TFTs on flexible substrate is to come up with a satisfactory gate dielectric material and a process to develop such dielectrics that allows low voltage performance, and reliable and stable operation, with low device off-state current. The gate dielectric influences the type of deep level defect state in both metal oxide and organic TFTs.

SiO_2 is most commonly used dielectrics in microelectronics due to its abundance and ease of fabrication.[1] It can be thermally grown at 1000 ^oC on Si substrate. SiO_2 is a wide band gap insulator with a band gap of 9 eV, dielectric constant of 3.9, exceptionally low leakage current, high breakdown voltage, and low defect density. Every new metal oxide or organic transistor is therefore tested on SiO_2 dielectric. It is not an ideal option for large area electronics or electronics on plastic. For flexible display application, low voltage operation is a requirement as these are driven by battery with limited power. One way to decrease the operating voltage is to use high k dielectric. For flexible electronics alternate inorganic and organic insulators and processes are being investigated in this context. Like for the case of semiconductor channels, the dielectrics grown by various vapour deposition (such as PLD, sputtering, ALD) as well as solution deposition (such as spin coating, dip coating) methods are currently being investigated.[54-56]

Atomic layer deposition (ALD) is self-limiting, sequential, surface reaction process which is thermally driven. Being a layer by layer deposition technique the films deposited by ALD are high density, pinhole-free with a featureless microstructure, making ALD an ideal process for growing gate dielectrics. The ALD deposition can be done at moderate temperature making it suitable for flexible electronics.[57]

1.3.9 Transport mechanism in metal oxide

Charge transport mechanism

For transparent metal oxide deposited by physical vapour route (PLD or sputtering) the mobility is found to depend on the composition (metal ion ratio) and annealing condition.[58] Another interesting feature is that the Hall mobility (μ) is found to increase with carrier density (N_e) unlike conventional semiconductors where μ decreases with increasing carrier density. The Fermi level is found to lie within the conduction band whereas the mobility shows thermally activated behavior indicating the transport to be limited by potential barriers above conduction band. The transport is explained in terms of percolation transport.

The percolation model assumes the charge transport to take place in a conduction band with a square-root energy dependence of the densities of states (DOS). The transport is assumed to be controlled by the distributed potential barrier above mobility edge with barrier height given by E_{center} and energy distribution as ΔE.

For band transport the conductivity is related to

$$\sigma = ne\mu$$

According to percolation theory,[59] the conductivity of the system is given by

$$\sigma = \sigma_0 e^{s_c}$$

Where σ_0 is an unknown prefactor and s_c is the exponent of the critical percolation conductance

$$G = G_0 e^{s_c}$$

Multiple trap and release (MTR)[60] model assumes that the charge transport occurs in extended state with most of the carrier injected in the semiconductor are trapped in the state localized in the forbidden gap. The basic principle of the MTR is the surface charge σ induced by the gate voltage split into trapped charge σ_T and free charge σ_F. In multiple-trapping model the transport is governed by thermal activation from traps to a conduction band and subsequent re-trapping, without involving a tunneling step.

For transparent metal oxide deposited by solution route the mobility is found to depend on composition, and the annealing temperature for film formation.[61] The mobility also depends on gate voltage and temperature. As shown in **Figure 1.9** the electron conduction above the threshold voltage and low gate voltage is controlled by multiple trap and release model, and at high gate voltage it is dominated by percolation conduction.[62]

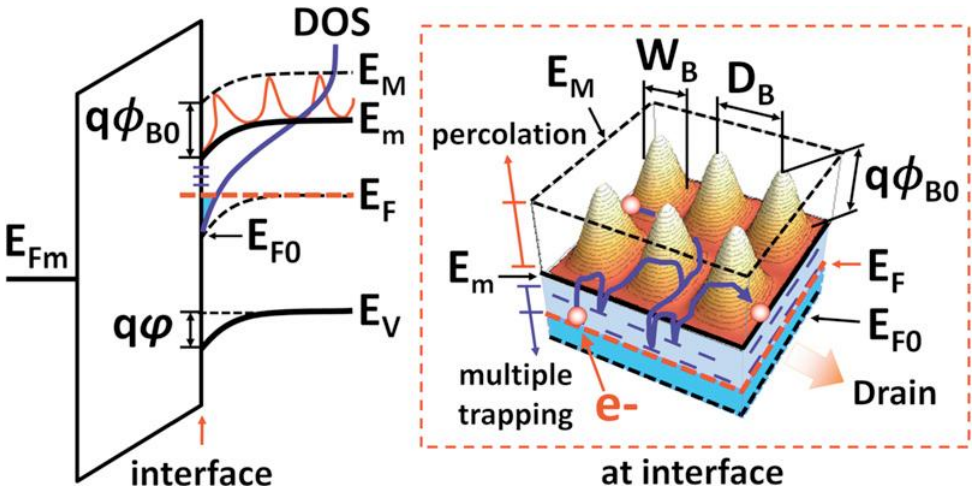

Figure 1.9: *Schematic band diagram of an oxide semiconductor TFT showing the presence of band tail states and potential fluctuations above Em, giving rise to TLC and percolation. (from ref 62)*

In polycrystalline TFT the grain boundaries act as a additional source for electron trap. The mobility of charge carriers in polycrystalline films is given by Levinson's model[63] as,

$$\mu^{-1} = \mu_0^{-1} + [\mu_{gb}\exp(-E_b/kT]^{-1}$$

Where, μ_o is the mobility in single crystalline counterpart,$\mu_{gb}\exp(-E_b/kT)$ is the contribution accounting for the grain boundary scattering. The barrier height is given by

$$E_b = \frac{q^2 N_{trap}^2}{8\varepsilon n}$$

Where q is the electronic charge, N_{trap} is density of traps at the grain boundary; n is the density of mobile carriers in a grain and ε is the dielectric constant of the semiconductor.

1.3.10 Semiconductor used as channel in this thesis

- **Zinc Oxide (Deposited by rf sputtering)**

  Zinc oxide with mobility of 200 $cm^2V^{-1}s^{-1}$ and excellent optical transparency is an ideal candidate for transparent electronics. In sputtering Zn and O (atoms, ions, complexes) are removed from a solid target (ZnO pellet) by the use of ionized Ar and get deposited on the surface of a substrate, at room temperature, in a vacuum chamber. An appropriate pressure of O_2 is kept to eliminate defects. The ZnO deposited by this method is polycrystalline in nature.

- **Indium oxide (In_2O_3)**

  Indium oxide is an n-type transparent conducting oxide that generally exists in bixbyite or C-type rare-earth structure. In_2O_3 has a high band gap of (3.6 - 3.75 eV), high single crystal mobility (160 cm^2/Vs), and good visible region transparency (> 90%) which make it an ideal candidate for transparent electronics.

- **Indium Zinc Oxide (IZO)**

  Pure In_2O_3 usually have large carrier density (due to low binding energy of In-O) resulting in high off currents when employed in TFTs. On adding Zn in In, the carrier density can be decreased, thereby decreasing the off current and improving the I_{on}/I_{off} ratio in TFT. The binary oxide always form polycrystalline films whereas ternary oxides (InZnO, ZnSnO) and quaternary oxides (InGaZnO) can form either amorphous or polycrystalline thin films depending on the metal ion ratios in the film.

1.4 Nonvolatile Memory Transistor

When the gate dielectric of a transistor is modified so that charges can be stored reversibly in the dielectric, then the transistor can work as nonvolatile memory device. A memory field effect transistor was first proposed by Kahng and Sze in 1967.[1] Nonvolatile memories do not lose its data when the system or device is turned off. They can be broadly classified into two types:

1. Floating gate devices: Here, there are two gates, one is control gate and the other is a floating gate. In floating gate devices charges are stored in floating gate.

2. Metal-insulator-oxide-semiconductor (MIOS): In this case the charges are stored at the insulator-oxide interface.

In both the cases, the charges are injected from the semiconductor into either the floating gate or the semiconductor insulator interface. A nonvolatile memory (NVM) device is a MIS transistor that has a source, a drain, an access or a control gate, and a floating gate. Tunneling is the process by which an NVM can be either be erased or programmed .The storage of the charge on the floating gate or semiconductor insulator interface electrically alters the threshold voltage (V_{th}) between a low and a high value to represent logic state of 0 and 1, respectively. In floating gate memory devices, charge or data is stored in the floating gate and is retained when the power is removed. Non volatile

memory using SiNx charge traps layer and 4.3 nm SiOx as tunneling layer was used in between ZnO channel and SiO_2 dielectric.[64] Various charge trapping layers like Ag nanoparticle, [65]Al_2O_3 or SiNx[66] have been used.

Nonvolatile memory transistors can also be made by using a ferroelectric material as a dielectric in the field effect transistor.

1.4.1 Ferroelectric Field effect transistor (FeFET)

When the gate insulator of a TFT is replaced by a ferroelectric gate insulator than ferroelectric field effect transistor (FeFET) are formed. In ferroelectric field effect transistors the remnant polarization of ferroelectric film provides the opportunity to store the information as a nonvolatile memory element. The polarization of the ferroelectric film controls the conductance of the overlying channel layer. Reading the conductance of channel allows a non-destructive readout of the polarization state of the ferroelectric. In ferroelectric capacitive kind of memory element the polarization state of the ferroelectric is affected during the readout process. For a n-type FeFET the ferroelectric polarization of the gate dielectric leads to accumulation of electrons in the semiconductor in a remnant way for positive gate bias as shown in **Figure 1.10**. A small drain voltage can then be used to probe the conductance without affecting the polarization state of the gate dielectric. If the gate voltage is removed then also the charges remain accumulated at the channel due to the remnant polarization of the dielectric.[67] Only when the field higher than the coercive field is applied the channel is depleted of the electrons. The FeFETs can thus be used as nonvolatile memory FETs.

The advantage of FeFETs over ferroelectric capacitor as a memory element is that the memory state can read out non-destructively as I_{ds} (in ferroelectric capacitor the readout operation involves applying a field and measuring the displacement response that is either high or low, depending on the initial polarization direction. So the readout process itself destructs the stored polarized state).

Ferroelectric field effect transistor using $(Fe,Zn)_3O_4$ as channel and ferroelectric PZT (with high curie temperature) as dielectric has been made. The films were deposited by PLD on Nb-STO as the substrate. The modulation of carrier density in ferri-magnatic $(Fe,Zn)_3O_4$ was achieved by ferroelectric field control by PZT.[68] High mobility FeFET has also been made by depositing PVdF-TrFE by spin coating to serve as dielectric and sputtered deposited ZnO as the channel. [69]

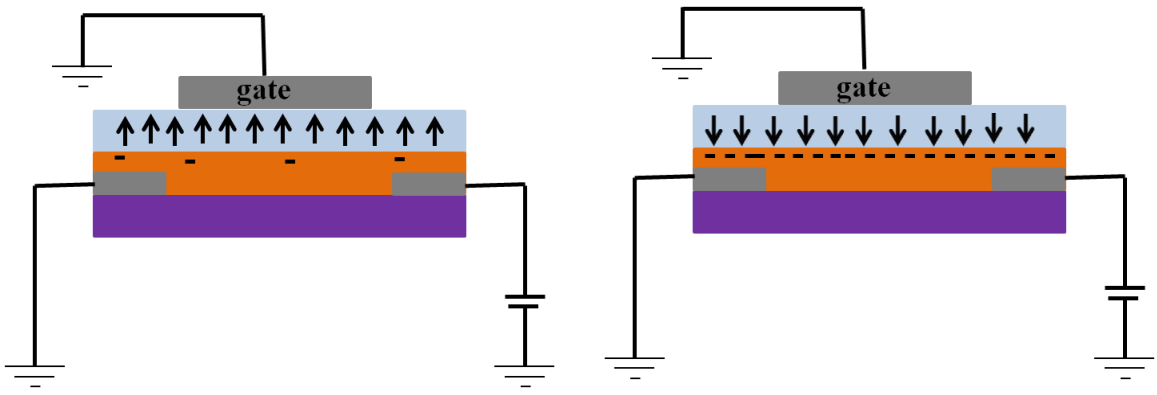

Figure 1.10: *shows the working principal of FerroFETs. When negative potential is applied to the gate then the ferroelectric dielectric gets depolarized causing depletion of charges at the semiconductor-dielectric interface. If the gate voltage is removed the dielectric still remains depolarized by measuring* I_{ds} *by applying* V_{ds} *this state can be read out without destructing the depolarized state i.e. the low* I_{ds} *denotes 0 state of the memory. When positive gate voltage is applied the ferroelectric dielectric gate polarizes leading to the formation of accumulation layer at the semiconductor-dielectric layer. This can be read as high* I_{ds} *state by applying* $V_{ds,}$ *the state 1 of the memory.*

1.4.2 Poly(vinylidene fluoride co hexafluoropropylene) (PVdF-HFP)

It is a co-polymer of PVdF with HFP. PVdF, a homopolymer, is a ferroelectric polymer with relatively large remnant polarization, a short switching time and a good thermal stability. The dipole moment in PVdF arises due the highly electronegative fluorine atom. PVdF and its copolymer are semi-crystalline polymers known to exists in

4 phases namely α, β, γ and δ which differ in their crystal structure. The α phase is known as the paraelectric phase. PVDF thin films processed from the melt or from a solution prefer the α phase formation because the crystal structure and stereo-chemical conformation are such that the dipole moments cancel each other out. The ferroelectric phase can be obtained by stretching, electric poling, addition of metal salts, clay graphene etc.

Over the years, PVdF and its copolymer have been explored for various electronic devices such as piezoelectric sensor, actuator as a protection coating due to its abrasion resistance, stiffness, non-flammability, radiation tolerance and resistance to harsh chemicals. They are also explored as nonvolatile memory elements. PVdF and its copolymer also have high κ dielectric and have been used in FET.

1.4 Objectives and outline of thesis

The objective of my thesis is to develop and study various material systems from solution route and low temperature processes based on polymers, metal oxides and metal sulfides for application in photodetector and field effect transistor.

Chapter 3: Zinc Oxide is an oxide semiconductor used in various optoelectronic applications. Specifically, photodetectors based on such metal oxides are considered important because they can be directly integrated on electronic circuits, and grown on flexible substrate with different morphologies by simple chemical protocols. There is growing interest in enhancing the performance of ZnO based photodetectors by improving the morphology, contact type, surface functionalization etc. In this work we have shown that an interface between a quasi-liquid ionic conductor and light harvesting configuration of quasi-1D functional metal oxide (ionic-electronic hybrid) yields a highly efficient photodetector that shows strong response in the UV as well as partial visible range. The electric field induced band bending at the interface and the light harvesting nature of nanorod (NR) configuration are together shown to help realize three orders of magnitude higher photocurrent in this ZnO (NR)-Gel-Pt device as compared to the case

of bare ZnO (NR)-Pt system. Impedance spectroscopy is used to bring out a significant decrease in the charge transfer resistance and capacitance of this interface-controlled device upon illumination. We have further shown that the gel layer remarkably improves the response time and spectral responsivity of the ZnO(NR)-gel-Pt system in comparison to bare ZnO(NR)-Pt system. The experimental methods, results and analysis of the work done on the photo sensing property of zinc oxide nanorods forming interface with a shape conforming hydrogel (agarose gel) are included.

Chapter 4: In this work we have examined the photo-sensing properties of vertically aligned $ZnIn_2S_4$ nanopetal films on FTO-glass in as-grown form and with surface modification involving dispensation of agarose gel. Zinc Indium Sulphide ($ZnIn_2S_4$), a ternary chalcogenide with layered structure employed in this work, is already a material of interest to the fields of charge storage, photocatalysis and photovoltaics. Our work shows that with proper surface tuning this material can also deliver in the context of photosensing. Most interestingly, while the $ZnIn_2S_4$ nanopetals film does not exhibit photoresponse under zero bias (though it does at finite voltages), dispensation of agarose gel on the film surface yields a strong photoresponse even under zero bias; making it a highly efficient self-powered UV and visible light photodetector. Remarkably, the zero bias $ZnIn_2S_4$/gel hybrid photoresponse is 100 times stronger as compared to the only $ZnIn_2S_4$ device response (at -1.5 V bias) without significant degradation in response time. We have discussed the possible operating mechanisms.

Chapter 5: Nonvolatile memory transistors employing either ferroelectric layers or charge trapping layer as gate insulators have received attention due to their benefits, including a non-destructive readout capability. Various inorganic and organic ferroelectric materials have been used in ferroelectric field effect transistors (Fe-FETs). Among organic materials PVdF and its copolymers, especially PVdF-TrFE, are the most studied in Fe-FETs and FETs. PVdF-HFP is another copolymer of PVdF with high dielectric constant, breakdown strength, and chemical inertness; however, to the best of our knowledge, the same has not yet been explored in the FET context. Here we report a nonvolatile memory transistor using zinc oxide (ZnO) as the channel and Poly(vinylidene fluoride-co-hexafluoropropylene) (PVdF-HFP) clay nanocomposite as the gate dielectric.

The field effect transistor (FET) made with pure PVdF-HFP gate dielectric is linear since in this case PVDF-HFP- is in the α-phase, a linear high κ form. Addition of clay induces formation of the ferroelectric β-phase in the nanocomposite. The corresponding nonvolatile memory thin film transistor made on glass substrate shows maximum operating voltage of 100 V and mobility of $1cm^2V^{-1}s^{-1}$.

Chapter 6: Recently, a lot of studies are going on metal oxide based transistor as they are a prime candidate to drive the future display technology. In any transistor the semiconductor insulator interface, contact resistance has drastic effect on the transistor parameter such as mobility, current I_{on}/I_{off} ratio. For transparent metal oxide transistor synthesized by precursor route even the annealing temperature has effect on the transistor performance. Here, we have fabricated Indium oxide TFT at low temperature using combustion chemistry by spin coating. We studied the effect of semiconductor dielectric interface on the performance of the transistor and found the TFT performance enhances on using high κ dielectric Al_2O_3 than SiO_2. To study the effect of variation of dielectric on the performance of the TFT in detail low temperature measurements were performed. Further, the contact resistance was calculated based on transmission line model.

1.5 References

1. S. M. Sze, K. K. Ng, in *Physics of semiconductor Devices* ,3 edition, *Wiley-VCH*, Hoboken, New Jersey, **2007**.
2. S. L. Gupta and V. Kumar, *Handbook of electronics*, 23 edition, Pragati Prakashan, Meerut, **1998**.
3. J. Zaumseil and H. Sirringhaus, *Chem. Rev.* **2007**, 107, 1296.
4. A. Facchetti, M. - H. Yoon, T. J. Marks, *Adv Mater.* **2005**, 17, 1705.
5. D. Braga, and G. Horowitz, *Adv. Mater.* **2009**, 21, 1473.
6. Editors A. Facchetti and T. J. Marks, in *Transparent Electronics From Synthesis to Applications*, 1 edition, *John Wiley & Sons Ltd*, **2010**.
7. T. Kamiya and H. Hosono, *NPG Asia Mater*. **2010,** 2, 15.
8. H. Hosono, *J. Non-Cryst. Solids*, **2006**, 352, 851.

9. E. Fortunato, P. Barquinha , and R. Martins, *Adv. Mater*. **2012**, 24, 2945.
10. M. Razeghi and A. Rogalski, *J. Appl. Phys.* **1996,** 79, 7433.
11. P. F. Carcia, Z. S. McLean, M. H. Reilly, and G. Nunes, *Appl. Phys. Lett.*, **2003,** 82, 1117.
12. Technical information characterstics and uses of infrared detectors *HAMAMATSU*.
13. C. Soci, A. Zhang, X.-Y. Bao, H. Kim, Y. Lo, and D. Wang, *J. Nanosci. Nanotechn.* **2010,** 10, 1.
14. G. Konstantatos and E. H. Sargent, *Nat. Nanotech*. **2010**, 5, 391.
15. L. Peng, L. Hu , and X. Fang, *Adv. Mater.* **2013**, DOI: 10.1002/adma.201301802.
16. B. J. Hansen , Y. Liu , R. Yang , Z. L. Wang , *ACS Nano* **2010** , 4 , 3647 .
17. Y. Yang, W. Guo, J. Qi, J. Zhao, and Y. Zhang, *Appl. Phys. Lett*. **2010,** 97, 223113.
18. Y.-Q. Bie, Z.-M. Liao, H.-Z. Zhang, G.-R. Li, Yu Ye, Y.-B. Zhou, J. Xu , Z.-X. Qin, L. Dai, and D.-P. Yu, *Adv. Mater.* **2011**, *23*, 649.
19. S. M. Hatch, J. Briscoe , and S. Dunn, *Adv. Mater.* **2013**, *25*, 867.
20. X. Li , C. Gao , H. Duan , B. Lu , Y. Wang , L. Chen ,Z. Zhang , X. Pan , E. Xie, *Small* **2013**, 9, 2005.
21. X. Lia, C. Gaoa, H. Duanb, B. Lua, X. Pana, E. Xiea, *Nano Energy* **2012** *1*, 640.
22. J. Zhou, Y. Gu, Y. Hu, W. Mai, P.-H. Yeh, G. Bao, A. K. Sood, D. L. Polla, and Z. L. Wang, *Appl. Phys. Lett*. **2009,** 94, 191103.
23. Q. H. Wang, K. Kalantar-Zadeh, A. Kis, J. N. Coleman and M. S. Strano, *Nat. Nanotech* **2012**, 7, 699.
24. P. A. Hu, L. Wang, M. Yoon, J. Zhang, W. Feng, X. Wang, Z. Wen, J. C. Idrobo, Y. Miyamoto, D. B. Geohegan, and K. Xiao, *Nano Lett*. **2013**, 13, 1649.
25. P. A. Hu, Z. Wen, L. Wang, P. Tan, and K. Xiao, *ACS nano* **2012,** 6 , 5988.
26. M. Law, D. J. Sirbuly, J. C. Johnson, J. Goldberger, R. J. Saykally, P. D Yang, *Science* **2004**, 305, 1269 .
27. M. Chhowalla, H. S. Shin, G. Eda, L. - J. Li, K. P. Loh and H. Zhang, *Nat. Chem.* **2013,** 5, 263.

28. Q. H. Wang, K. K. Zadeh, A. Kis, J. N. Coleman and M.S. Strano, *Nat. Nanotech* **2012,** 7, 699.
29. Ü. Özgür, Ya. I. Alivov, C. Liu, A. Teke, M. A. Reshchikov, S. Doğan, V. Avrutin, S. - J. Cho, H. Morkoçd, *J. Appl. Phys.* **2005**, 98, 041301.
30. S. Peng, P. Zhu, V. Thavasi, S. G. Mhaisalkar, and S. Ramakrishna, S. *Nanoscale*, **2011**, 3, 2602-2608.
31. A. Serpi, *J. Phys. D: Appl. Phys.*, **1976,** 9.
32. J. Filipowicz, N. Romeo and L. Tarricone, *Solid State Commun*. **1980,** 38, 619-623.
33. N. Romeo, A. Dallaturca R. Braglia and G. Sberveglieri, *Appl. Phys. Lett.* **1973,** 22, 21.
34. A. W. Bott Current Separations **1998,** 17:3.
35. N. Bonanos, B. C. H. Steele, E. P. Butler, in Impedance Spectroscopy Theory, Experiment, and Applications (Eds: E. Barsoukov, J. R. Macdonald) *Wiley-VCH*, Hoboken, New Jersey, **2005**, Ch. 4.
36. I. K. Kovhcs and G. Horvai, *Sensors and Actuators B,* **1994,** 18-19, 315.
37. J. E. Lilienfield, *U.S. Patent* **1930,** 1745175.
38. P. K. Weimer, *Proc. IRE* **1962**, 50, 1462.
39. G. Horowitz, P. Lang, M. Mottaghi and H. Aubin, Adv. Funct. Mater. **2004,** 14, 1069; b) J. Zaumseil, K. W. Baldwin and J. A. Rogers J. Appl. Phys. **2003,** 93, 6117 .
40. K. Nomura, H. Ohta, A. Takagi, T. Kamiya, M. Hirano,and H. Hosono, *Nature*, **2004,** 432, 488.
41. S. Jeong and J. Moon, *J. Mater.Chem.* **2012, 22**, 1243.
42. K. Okamura, D. Nikolova, N. Mechau and H. Hahn, *J. Mater. Chem*. **2010**, 20, 5651.
43. S. Jeong, Y. Jeong, and J. Moon, *J. Phys. Chem. C*, **2008**, 112, 30.
44. K. Song, J. Noh, T. Jun, Y. Jung, H.-Y. Kang and J. Moon, *Adv. Mater.* **2010**, 22, 4308.
45. D. Kim, Y. Jeong, K. Song, S.-K. Park, G. Cao, and J. Moon, *Langmuir* **2009**, 25, 11149.

46. S. Jeong, Y.-G. Ha, J. Moon, A. Facchetti, and T. J. Marks, *Adv. Mater*. **2010**, 22, 1346.
47. J. H. Jeon, Y. H. Hwang, B. S. Bae, H. L. Kwon, and H. J. Kang, *Appl. Phys. Lett*. **2010**, 96, 212109.
48. H. S. Kim, M.-G. Kim, Y.-G. Ha, M. G. Kanatzidis, T. J. Marks, and A. Facchetti, *J. Am. Chem. Soc.* **2009**, 131, 10826.
49. M.-G. Kim, H. S. Kim, Y.-G. Ha, J. He, M. G. Kanatzidis, A. Facchetti, and T. J. Marks, *J. Am. Chem. Soc.* 2010, **132**, 10352–10364.
50. H. S. Kim, P. D. Byrne, A. Facchetti, and T. J. Marks, *J. Am. Chem. Soc*. **2008**, 130, 12580.
51. M.-G. Kim, M. G. Kanatzidis, A. Facchetti and T. J. Marks, Nat. Mater. 2011, **10**, 382.
52. K. K. Banger, Y. Yamashita, K. Mori, R. L. Peterson, T. Leedham, J. Rickard and H. Sirringhaus, *Nat.Mater*. **2011**, 10, 45.
53. S.-Y. Han, G. S. Herman, and C. - H. Chang, *J. Am. Chem. Soc*. **2011**, 133, 5166.
54. B. N. Pal, B. M. Dhar, K. C. See and H. E. Katz, *Nat. Mater.* **2009,** 8, 898.
55. H. S. Kim, P. D. Byrne, A. Facchetti, and T. J. Marks, *J. Am. Chem. Soc*. **2008,** 130, 12580.
56. Y.-H. Lin, H. Faber, K. Zhao, Q. Wang, A. Amassian, M. McLachlan, and T. D. Anthopoulos, *Adv. Mater*. **2013**, 25, 4340.
57. Y.-H. Kim, J.-S. Heo, T.-H. Kim, S. Park, M.-H. Yoon, J. Kim, M. S. Oh, G.-R. Yi, Y.-Y. Noh and S. K. Park, *Nature*, **2012**, 489, 11434.
58. T. Kamiya, K. Nomura and H. Hosono, *J. Display Techn.* **2009,** 5, 468.
59. W. Chr. Germs, W. H. Adriaans, A. K. Tripathi, W. S. C. Roelofs, B. Cobb, R. A. J. Janssen, G. H. Gelinck, and M. Kemerink, *Phys. Rev. B* **2012,** 86, 155319.
60. G. Horowitz, M. E. Hajlaoui, and R. Hajlaoui, *J. Appl. Phys*. **2000,** 87, 4456.
61. W. Hu and R. L. Peterson, *J. Mater. Res*., **2012**27, TBD.
62. S. Lee, K. Ghaffarzadeh, A. Nathan, J. Robertson, S. Jeon, C. Kim, I. - H. Song, and U. – I. Chung, *Appl. Phys. Lett.* **2011,** 98, 203508.
63. J. Levinson, F. R. Shepherd, P. J. Scanlon, W. D. Westwood, G. Este, and M. Rider, *J. Appl. Phys.* **1982,** 53, 1193.

64. E. Kim, Y. Kim, D. H. Kim, K. Lee, G. N. Parsons, and K. Park, *Appl. Phys. Lett*. **2011,** 99, 112115.
65. D. Gupta, M. Anand, S.-W. Ryu, Y.-K. Choi and S. Yoo, *Appl. Phys. Lett.* **2008,** 93, 224106.
66. S. A. DiBenedetto, D. Frattarelli, M. A. Ratner, A. Facchetti, and T. J. Marks, *J. Am. Chem. Soc*. **2008**, 130, 7528.
67. R. C. G. Naber, Ph.D. thesis, University of Groningen, The Netherlands 2006.
68. J. Takaobushi, T. Kanki, T. Kawai, and H. Tanaka, *Appl. Phys. Lett.* **2011**, 98, 102506.
69. K. H. Lee, G. Lee, K. Lee, M. S. Oh, S. Im and S.-M. Yoon, *Adv. Mater*. **2009**, 21, 4287.

CHAPTER 2

Experimental and Characterization Techniques

In this chapter, we present details of the methods used for sample preparation and the experimental techniques employed. Two methods were used for thin film preparation, namely spin coating and RF sputtering. The films were studied and analyzed by different characterization techniques; mainly Fourier Transformed Infra-Red Spectroscopy (FTIR) and X-ray diffraction (XRD). We discuss these in respect of the principle and merit of the techniques. Additionally, investigation of the film morphology was carried out with the help of Scanning Electron Microscopy (SEM) imaging. The working principle of this technique is elaborated herein. Optical properties were determined using a UV-VIS spectrophotometer in DRS mode and an IPCE instrument. Finally, Capacitance-Voltage and PE-loop measurements were also performed on the films. The corresponding methods are also discussed.

2.1 Thin Film Deposition

Two techniques were used for film deposition, namely spin coating and RF sputtering. Before depositing the films it is essential to clean the substrates for achiving high quality films and reproducible results.

Substrate cleaning prior to film deposition

Various substrates such as corning 1737 glass, SiO_2/Al_2O_3 coated Si-wafers, ITO and FTO coated glass were used for our experiments. Before the preparation of thin films, pieces of substrate were cleaned through a standard RCA-1 cleaning procedure. This wet cleaning procedure is useful to remove organic contamination and particles from the surface of the substrate. The experimental set-up and the cleaning procedure are as follows:

• Substrates were cleaned by sonication in a soap solution, DI water and isopopanol respectively for 15 min each.

• Mixture of NH_4OH, H_2O_2 and de-ionized water (DI-water) was prepared in a ratio of 1:2:10. The solution is called RCA-1.

• The substrates were immersed in RCA-1 solution and the temperature was maintained at 70 ± 5 ^oC for 20 minutes. The solution starts bubbling confirming the onset of the cleaning process.

• After 20 minutes, the substrates were taken out and soaked into another beaker containing DI-water. This transfer should be fast to prevent wafers from drying up.

• The wafers were taken out one by one and rinsed with DI-water followed by rinsing with IPA. The drying was carried out using a N_2 gas flow. This step was useful to dry up the wafer faster and to prevent the formation of a water mask.

These treatments were followed for every set of samples. For solution processed indium oxide and indium zinc oxide films, the substrates were further treated with oxygen/air plasma for 5 minutes to make the substrate hydrophilic.

2.1.1 Spin coating

Spin coating is a widely used technique in the semiconductor industry for the deposition of polymer resist layers which are used in the lithographic patterning process.[1] For ultra-thin polymer film deposition, a spin coating unit is used. Spin coating is a process which involves depositing a small amount of a solution onto the centre of a substrate as shown in **Figure 2.1**, which is then spun around at a high speed so that the solution is spread out by the centrifugal force. The centrifugal force causes the excess solution to fly off the substrate and simultaneously, some of the solvent evaporates. The evaporation process raises the concentration and viscosity of the remaining solution. This high viscosity prevents the solution from exiting the substrate and a thin film of solution remains. Continued spinning evaporates the rest of the solvent after which a thin film of polymer is obtained. The spinning speed ranges from 1000 to 3500 rpm, depending on the interest of the film thickness. In a programmable spin coater, the solution is first spin coated at slower rate (of 100 rpm) so that the solution fully covers the substrate. Then a high speed is selected depending on the required film thickness. Final film thickness and other properties depend on the nature of the resin (viscosity, drying rate, percent solids, surface tension etc.) and the parameters chosen for the spin process. Factors such as final rotational speed, acceleration, and fume exhaust contribute to how the properties of coated films are defined.

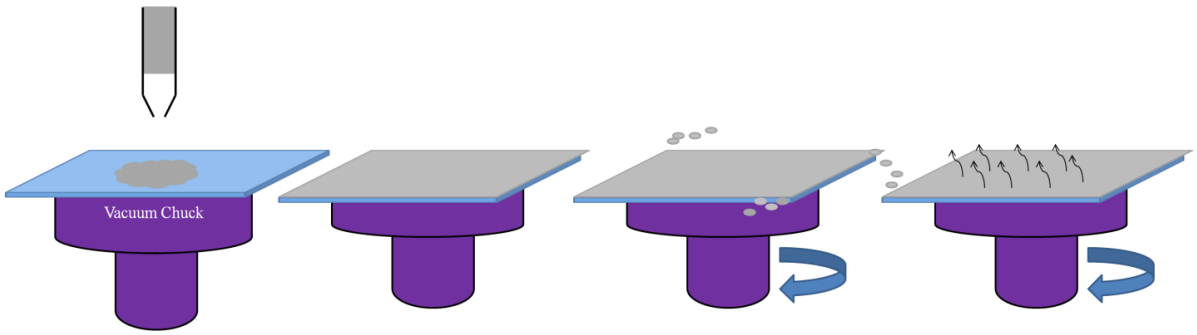

Figure 2.1: *Illustration of the spin coating technique*

A solution containing a polymer is deposited on a substrate, which is then spun at a high speed. The co-polymer we use is P(VDF-HFP) with a 94:6 molar ratio of VDF:HFP. The material is supplied as beads by Sigma Aldrich. There are some selective

solvents available for making P(VDF-HFP) solution for spin coating. We chose acetone as the solvent for spin coating as it is not hazardous and allows us to make a homogeneous polymer solution. We prepared different concentrations of P(VDF-HFP) (weight percent 5 % to 10 %) . By controlling the concentration of P(VDF-HFP) and spinning speed, we were able to achieve different film thicknesses on RCA-1 cleaned glass wafers. After spin coating, the film was annealed at 135 ^{o}C for 1 hour to improve the crystallinity.

2.1.2 RF Sputtering

Sputtering is a widely used physical vapour deposition method to deposit thin films of metal and metal oxides on a large area.[2,3] In the sputtering process, the material to be deposited is made into a solid target. This target is then bombarded with gas ions from plasma, resulting in ejection of the material from the target. The plasma ions are attracted to the target by the applied electric filed. Thus, sputtering consists of material erosion from a target on an atomic scale and the formation of a thin layer of the extracted material on a suitable substrate. The process is initiated in a glow discharge produced in a vacuum chamber under pressure-controlled gas flow. Target erosion occurs due to energetic particle bombardment by either reactive or non-reactive ions produced in the discharge. Magnets are placed behind the sputtering target in order to trap the electrons of the target thereby increasing the number of ions bombarding the target which in turn increases the sputtering rate and reduces heating of the substrate. In this process, the accelerated ions and neutral species present in the plasma provide the energy to the growing film which enhances surface mobility and causes densification of the growing film. The composition of the deposited film is almost perfectly identical to that of the target.

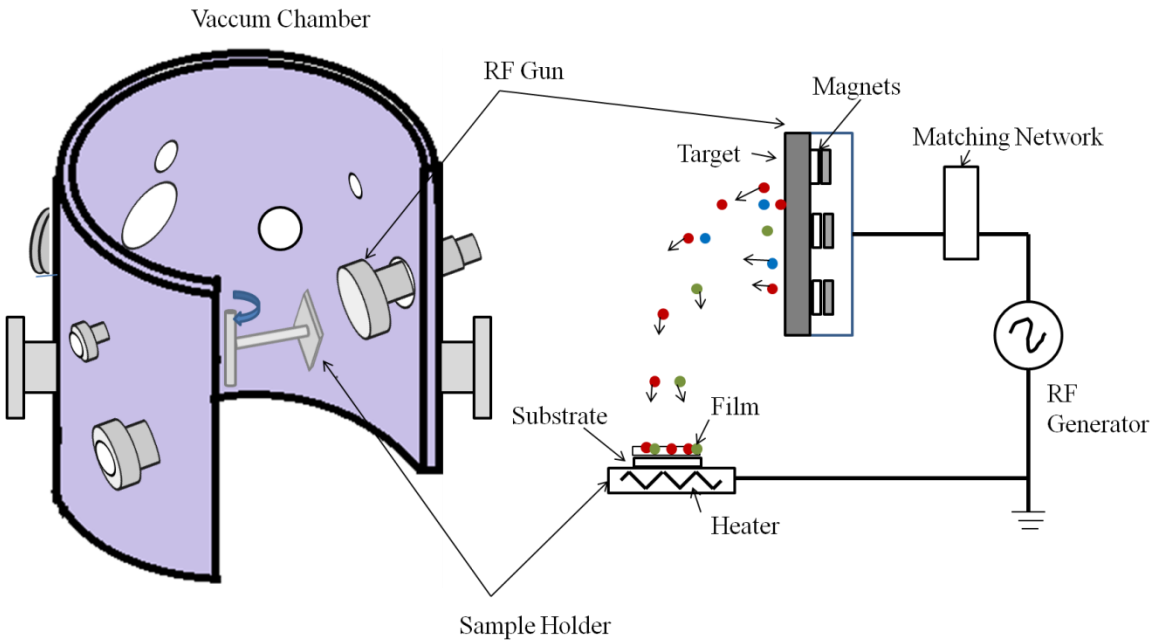

Figure 2.2: *Schematic of the deposition chamber and of the off-axis RF magnetron sputtering technique*

The off-axis radio frequency magnetron sputtering technique, schematically shown above, consists of a target, which is a plate of a stoichiometric mixture of the material to be grown, and a substrate placed on a grounded sample holder positioned at 90° of the target off-axis configuration. The glow discharge is initiated by applying power to the target in a controlled gas atmosphere, and is composed of a partially ionized gas of ions, electrons, and neutral species. The ejected material diffuses until it reaches and nucleates on the substrate. The duration of this process controls the thin film thickness. The crystalline growth of thin films on single crystal substrates, with a well defined orientation, defines epitaxy.

The use of a radio frequency (rf) generator is essential to maintain the discharge and to avoid charge build-up while sputtering metal oxides. The presence of a matching network between the rf generator and the target is necessary in order to optimize the power dissipation in the discharge. Magnets are used to enhance the sputtering rate, by increasing the ionizing effect of electrons magnetically trapped in the vicinity of the target (magnetron sputtering). Their use provides the advantage of trapping not only

electrons, but also charged species at the target, so that they do not hit the substrate, with an improvement of the film quality.

The benefits of magnetron sputtering sources are[2]:

(1) It scales easily in length, permitting production of coatings on very large substrates.
(2) Its compatibility with temperature- sensitive substrates, e.g. Plastic.
(3) Its ability to operate at lower pressure (than diode sputtering).
(4) The atomic composition (metallic) of deposited film is equal (approximately) to that of target.

2.2 Capacitance Measurement

These measurements are used extensively to study the microscopic material properties from mass transport, rates of chemical reactions, corrosion and dielectric properties to defects, microstructure and compositional influences on the conductance of solids.[4,5] Two types of measurements are generally used namely C-V and C-f measurements; in C-V measurements, the frequency is fixed and the DC bias is varied whereas in C-f measurements fixed DC bias is applied with variation in frequency. The capacitance is given by

$$C = \frac{\kappa A}{d}$$

Where C is the capacitance, κ is dielectric constant, A is the area of the capacitor and d is film thickness.

The C-V measurement involves the application of DC voltage (V_{DC}) across the capacitor and then performing the measurement by superimposing an AC signal (vsinωt).

$$V = V_{DC} + vsin\omega t$$

The resulting current is given by

$$J = J_{DC} + jsin\,\omega t$$

Where, J_{DC} is the DC Current and $jsin\,\omega t$ the AC current across the sample. If the applied ac voltage v is low then the ac current is proportional to derivative of the DC current J(V) times the AC voltage. The conductance is given by

$$G = dJ/dV = \frac{j}{v}$$

Where, G depends on applied bias voltage as well as frequency. The capacitance of the device is calculated as

$$C = \frac{I}{2\pi f V_{ac}}$$

Where I is the current flowing through the device, f is the applied frequency and V_{ac} is the magnitude and phase of the measured voltage. Basically the ac impedance of the device is calculated by applying ac voltage and measuring the ac current, voltage and the phase angle between the current and voltage. The measured capacitance also depends on frequency. The measurement of dependence of G and C on frequency is known as impedance/admittance spectroscopy (IS). The IS data can be fitted to equivalent circuit made up of ideal resistors, capacitors, inductances, and possibly various distributed circuit elements.

As mentioned in the first chapter, C-V measurement across a semiconductor/electrolyte interface or a MIS structure is used to extract various parameters such as carrier type, carrier density, type of space charge region (accumulation, depletion, inversion) within the semiconductor, and the flat band potential. The C-V combined with G-ω can be used to calculate the interface states. Different AC signal frequencies can reveal additional details. Low frequencies reveal what are called quasi-static characteristics, whereas high frequency testing is more indicative of dynamic performance. Both types of C-V testing are often required.

The C-V measurement was done using electrochemical impedance spectroscopy (EIS, Autolab PGSTAT 30) and Novo control impedance analyzer.

2.3 Incident photon-to-current conversion efficiency (IPCE) Measurements

Another fundamental measurement quantifying the performance of an optoelectronic device such as solar cell or photodetector is the "external quantum efficiency" or the incident photon to current conversion efficiency (IPCE). It specifies how efficiently the device under test (DUT) converts photons of a given wavelength into electrons. The IPCE value corresponds to the photocurrent density produced in the external circuit under monochromatic illumination of the device divided by the photon flux that strikes the device. From such an experiment the IPCE as a function of wavelength can be calculated from

$$IPCE = \frac{J}{e\phi_\lambda}$$

Where, e is the elementary charge, J is the current density and ϕ_λ is the incident photon flux.

Figure 2.3: *The Newport IPCE setup*

IPCE values provide practical information about the monochromatic quantum efficiencies of a solar cell.[6] If the absorption spectrum of the device under test is known, the fraction of absorbed photons can be used to calculate the internal quantum efficiency

(IQE). This value gives the percentage of photons absorbed by the DUT that are converted into electrons as a function of wavelength.

The setup consists of:

- Xenon Lamp: That generates the entire solar spectrum.
- Monochromator: It uses a grating and slits to reduce the Xenon lamps spectral output to nearly monochromatic light. Thus, it provides light of nearly monochromatic wavelength and measures the power at each wavelength. It is then used to calculate the number of photons that are generated. This light when incident on the device then the output current generated by the device can be used to calculate the number of electrons that are generated.
- Lock in amplifier: To measure the optical power and current.
- Current Preamp

2.4 Optical Spectroscopy

Optical Spectroscopy deals with the recording of absorption signals due to electronic transitions from near ultraviolet to near infrared region. The spectrometer can operate in two modes (i) transmission and (ii) reflection mode. In transmission mode usually materials like carbon and/or colloidal nanoparticles (NPs) well-dispersed in solvent are used. The optical measurements for opaque thin films and those NPs which are not dispersible in solvents are recorded in the diffuse reflectance (DRS) mode.

The light from the source is alternatively split into one of two beams by a chopper; one beam is passed through the sample and the other through the reference. The detector, which is often a photodiode, alternates between measuring the sample beam and the reference beam. Some double beam instruments have two detectors, where the sample and reference beams are measured at the same time.

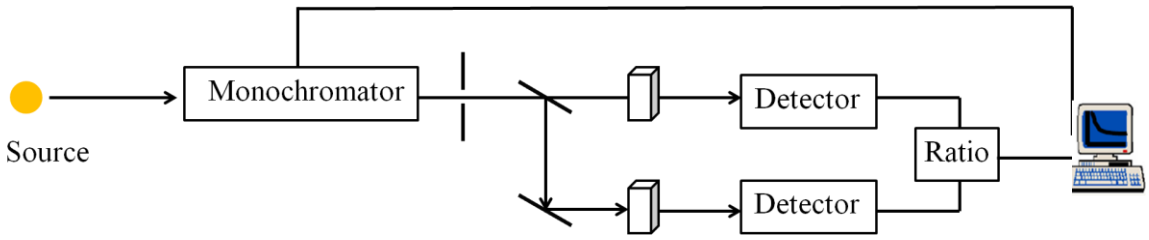

`

Figure 2.4: *Schematics of UV-VIS Spectrophotometer in Transmission Mode*

The schematic diagram of UV-VIS Spectrophotometer is shown in **Figure 2.4**. In other instruments, the two beams pass through a beam chopper which blocks one beam at a time.

Broadening of spectral transitions takes place possibly because of:

(a) Doppler Broadening: Random motion of NPs in the liquids and gaseous samples causes their absorption and emission frequencies to show a Doppler shift and hence the spectrum lines are broadened. This effect is more pronounced in liquids than gaseous samples due to significant collisions in solutions. In the case of solids, the motions of the particles are more limited in extent and less random in direction. Thus, solid phase spectra are often sharp but show evidence of interactions by the splitting of the lines into two or more components.

(b) Heisenberg's Uncertainty Principle: If a system exists in an energy state for a limited time 'δt' seconds, then the energy of that state will be uncertain (fuzzy) to an extent 'δE' and is given by $\delta E \times \delta t \approx h/2\pi \approx 10^{-34}$ J.s ,where h = Planck's Constant. Usually life time of excited state is 10^{-8} sec, i.e. 10^{8} Hz, so the uncertainty in the radiation frequency which is, in fact, small as compared to UV-Vis frequency regime ($10^{14} – 10^{16}$ Hz).

Intensity of Spectral lines: There are three main factors that decide the intensity of spectral lines: (i) Transition probability: The likelihood of a system in one state changing to another state, which is usually governed by quantum mechanical selection rules.

(ii) Population of states: The number of atoms/molecules initially in the state from which the transition occurs. This is governed by the equation: $N_{upper} / N_{lower} = \exp(-\Delta E/kT)$; where, $\Delta E = (E_{upper} - E_{lower})$, T= temperature (K), k = Boltzman's Constant = 1.38×10^{-23} J/K.

(iii) Concentration and path length: Since the sample is absorbing energy from a beam of radiation, increase in the amount of sample results in an increase path length for the beam and simultaneously a greater energy absorption. Besides the amount of the sample, the concentration of the sample is also a deciding factor for the energy absorption. Based on this, Beer-Lambert law, which is often written as:

$I / I_0 = \exp(-\kappa cl)$ or $I / I_0 = 10^{-\varepsilon cl} = T$

Where, κ = constant, for particular spectroscopic transition under consideration.

Where T = transmittance = I / I_0 , ε = molar absorption coefficient.

Inverting above equation and taking logarithms,

$I_0 / I = 10^{\varepsilon cl}$ or $\log (I_0 / I) = \varepsilon cl = A$, Where A = absorbance / optical density

Thus, absorbance is directly proportional to the concentration, where the path length and molar extinction coefficient is supposed to be constant for the particular measurement. The source used for the UV and visible light are deuterium and tungsten lamps respectively and the detector used is usually PMT.

2.5 Powder X-Ray Diffraction

X-ray diffraction (XRD) technique is used to study structural properties of materials and obtain information about crystal structure/phase, lattice parameters, crystallite size, orientation of single crystals, preferred orientation of polycrystals, defects, strains etc.[7] This technique is suitable for thin films, bulk materials and nanomaterials. In the case of nanostructures, the change in lattice parameters w. r. t. bulk systems gives us an idea about the nature of strain present in the material.

In XRD, a collimated monochromatic beam of X-rays is incident on the sample for diffraction to occur. A constructive interference occurs only for certain θ's correlating to those (hkl) plane, where path difference is an integral multiple (n) of wavelength. Based on this, the Bragg's condition is given by

$$2dsin\theta = n\lambda$$

Where, λ is the wavelength of the incident X-ray, d is the interplaner distance, 'θ' is the scattering angle and n is an integer called order of diffraction.

In nanostructures, X-rays are diffracted by the oriented crystallites at a particular angle to satisfy the Bragg's condition. Having known the value of θ and λ, one can calculate the inter-planar spacing. The XRD can be taken in various modes such as θ-2θ scan mode, θ-2θ rocking curve, and ϕ scan. In the θ-2θ scan mode, a monochromatic beam of X-ray is incident on the sample at an angle of θ with the sample surface. The detector motion is coupled with the X-ray source in such a way that it always makes an angle 2θ with the incident direction of the X-ray beam (**Figure 2.5**). The resulting spectrum is a plot of the intensity recorded by the detector versus 2θ. Schematic view of XRD is shown in **Figure 2.5**.

The incident X-rays may reflect in many directions but will only be measured at one location. So we will require:

Angle of Incidence (θ_i) = Angle of Reflectance (θ_r)

This is done by moving the detector twice as fast in (θ) as the source. So, only where $\theta_i = \theta_r$, will be the intensity of the reflected X-rays to be measured.

Nanomaterials have smaller sized crystallites and significant strains due to surface effects, causing considerable peak broadening and shifts in the peak positions w.r.t. standard data. From the shifts in the peak positions, one can calculate the change in the d-spacing, which is the result of change of lattice constants under strain. The crystallite size (D) is calculated using Scherrer's formula:

$$D = k\,\lambda / \beta \cos\theta$$

Where, k = Scherrer's Constant ≈ 0.9, β = Full Width at Half Maximum (FWHM).

The only disadvantage of XRD is its less sensitivity towards low-Z materials. It is therefore more suitable for high-Z materials. In such cases, electron or neutron diffraction is employed to overcome the low intensity of diffracted X-rays. **Figure 2.5** shows the representation of X-ray Diffraction.

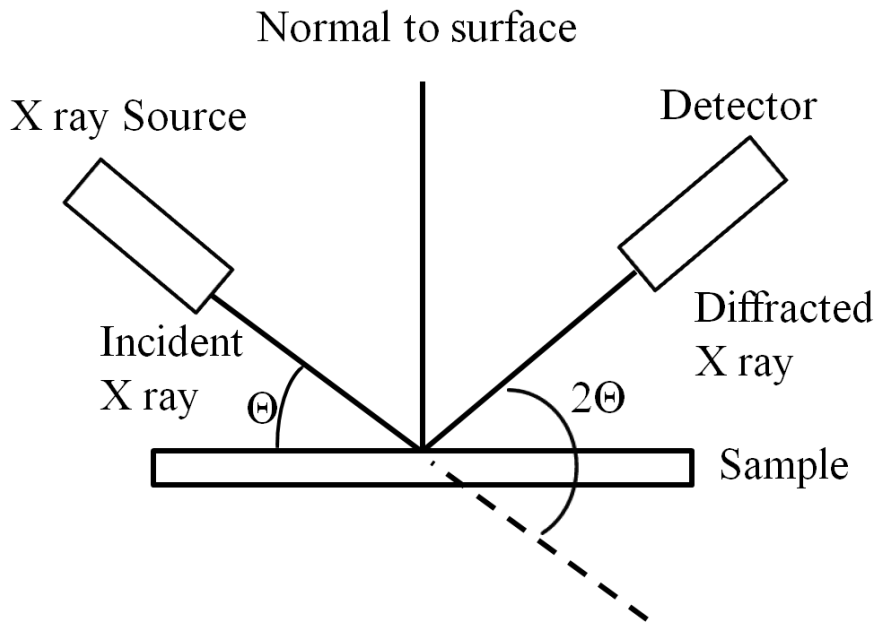

Figure 2.5: *Representation of X-ray Diffraction*

The θ-2θ scan maintains these angles with the sample, detector and X-ray source. Only planes of atoms that share this normal will be seen in the θ-2θ scan.

In the present work, the XRD patterns for all the samples were recorded using Pananlytical Philips X'Pert PRO powder diffractometer. In all the cases, the radiation source was Cu-K_α (λ = 1.542 Å).

2.6 Fourier Transform Infrared Spectroscopy

Infrared spectrum appears only when the vibrations amongst bonded atoms produce a change in the permanent electric dipole moment of the molecule/solid. It is

reasonable to suppose that the more polar a bond, the more intense will be IR spectrum arising from the vibrations of that bond. IR spectrophotometer consists of mainly source, monochromator and detector.[8,9] The source is in the form of a filament (e.g. Nernst Filament, made of a spindle of rare earth oxides or globar filament, made of carborundum rod) which is maintained as red- or white-hot by an electric current. The monochromator guides the IR beam and focuses it on the sample. The detectors are based on either temperature (bolometer/thermometer) or conductivity rise at given frequency (PbS).

Fourier Transform IR Spectroscopy: FTIR has considerably speeded up and improved spectroscopy in the IR region in general and in particular far IR region i.e. below 400 cm^{-1} where good amount of useful molecular information is contained. This is usually called as 'Energy Limited' region, where sources become weak and detectors insensitive, resulting in a poor signal to noise ratio.

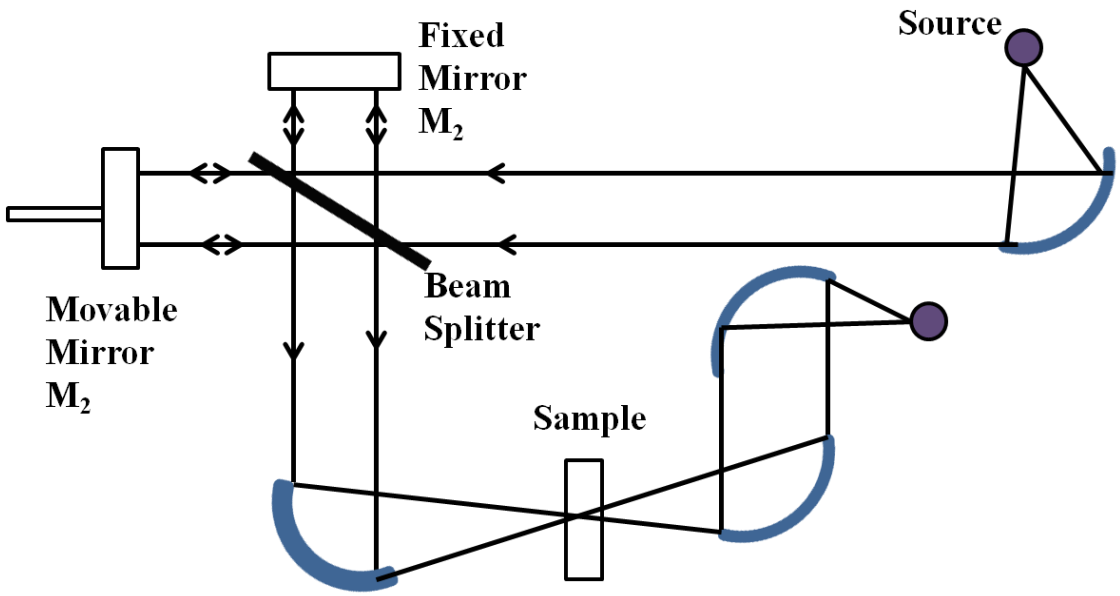

Figure 2.6: *Schematic of FTIR Spectrophotometer*

Figure 2.6 shows the schematic of FTIR spectrophotometer. The apparatus derives from the classical attempt by Michelson to measure the 'ether wind' by determining the velocity of light in two perpendicular directions. A parallel beam of radiation is directed from the source to the interferometer, consisting of the beam splitter

B and two mirrors, M_1 and M_2. The beam splitter is a plate of suitably transparent material (e.g. KBr) so as to reflect just 50% of the radiation falling on it. Thus half the radiation goes to M_1, and half to M_2, returns from both these mirrors along the same path, and is then recombined to a single beam at the beam splitter (clearly half the total radiation is sent back to the source, but this is immaterial). It is well known (and is the essence of the Michelson experiment) that if a monochromatic radiation emitted by the source is split and recombined as shown in **Figure 2.6**, the recombined beam leaving B shows constructive or destructive interference, depending on the relative path lengths namely B to M_1 and B to M_2. Thus if the path lengths are identical or differ by integral multiple of wavelengths, constructive interference gives bright beam leaving B, whereas if the difference is a half integral number of wavelengths, the beam cancels at B. As the mirror M_2 is moved smoothly away or towards from B, a detector sees radiation alternating in intensity. It is fairly easy to imagine that if the source emits two separate monochromatic frequencies, υ_1 and υ_2 then interference pattern of υ_1 and υ_2 would overlay the interference caused by M_1 and M_2; the detector would see a more complicated intensity fluctuation as M_2 is moved, but computing the Fourier transform of the resultant signal is very rapid way of obtaining the original frequencies and intensities emitted by the source. Taking the process further, even white radiations emitted by the source produce an interference pattern which can be transformed back to the original frequency distribution.

The production of a spectrum is a two-stage process: (a) Without a sample in a beam, mirror M_2 is moved smoothly over period of time (say one second) through a distance of about 1 cm, while the detector signal – the interferogram – is collected into multi-channel computer; the computer carries out the Fourier transformation of the stored data to produce background spectrum. (b) A sample interferogram is recorded in exactly the same way, Fourier transformed, and then ratioed against the background spectrum for plotting as transmittance spectrum. Alternatively, the sample and background spectra may each be calculated in absorbance forms and the latter simply subtracted from the former to give an absorbance spectrum of the sample alone. The advantage of using FTIR is that the whole spectrum is obtained across the entire frequency range at once with

constant resolving power. Powdered samples were mixed with the standard KBr powder. The FTIR measurements of these samples were carried out on a Perkin Elmer Spectrum One FTIR spectrometer operated in the diffuse reflectance mode at a resolution of 4 cm^{-1}. Three spectra were used for averaging.

2.7 Scanning Electron Microscope (SEM)

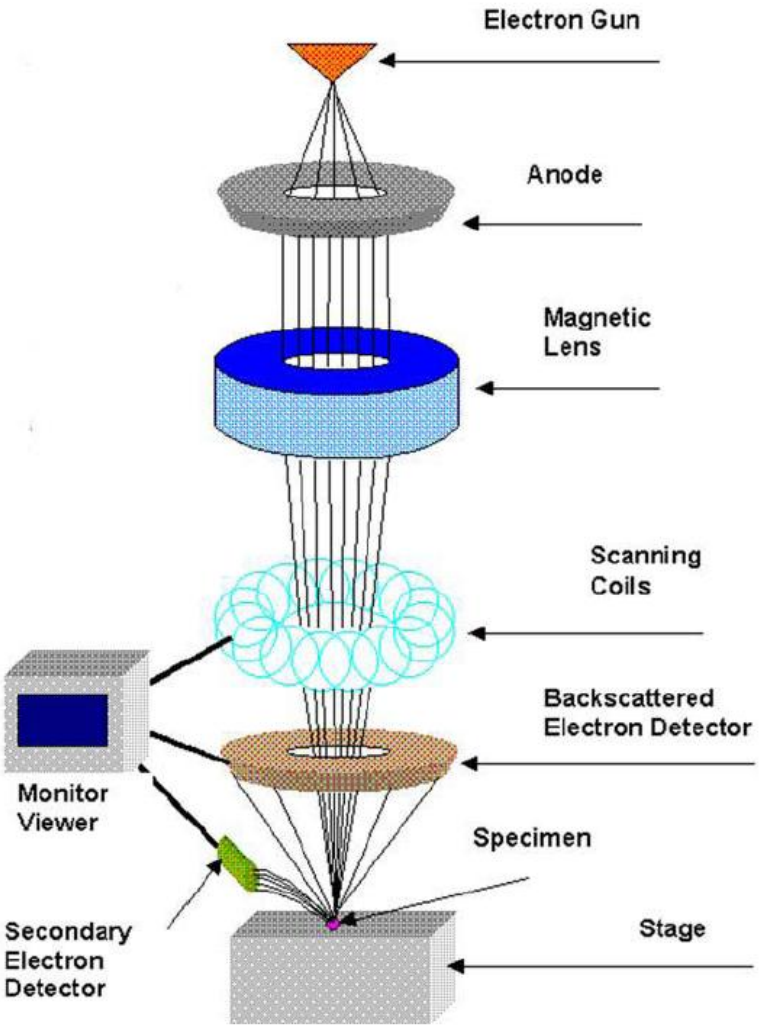

Figure 2.7: *Schematic diagram of the Scanning Electron Microscope*

[http://www.rpi.edu/dept/materials/COURSES/NANO/shaw/Page5.html]

SEM uses a beam of electrons focused to a diameter spot of approximately 1nm in diameter on the surface of the specimen and scanned back and forth across the surface. The surface topography of a specimen is revealed either by the reflected (backscattered) electrons generated or by electrons ejected from the specimen as the incident electrons decelerate secondary electrons. A visual image corresponding to the signal produced by the interaction between the beam spot and the specimen at each point and along each scan line is simultaneously built up on the face of a cathode ray tube similar to the way that a television picture is generated.

The best spatial resolution currently achieved is of the order of 1nm. **Figure 2.7** shows the schematic diagram of Scanning Electron Microscope. In the present work, the TEM and SEM images for the carbon and carbon composites samples were recorded on Ph.D. instrument (IFEI, Techni F30 FEG with 300 kV for TEM and FEI quanta 200 for SEM) at National Chemical Laboratory, Pune.

2.8 Ferroelectric Analysis

Ferroelectricity is a property of certain materials which possess a spontaneous electric polarization that can be reversed by the application of an external electric field. The term is used in analogy to ferromagnetism, in which a material exhibits a permanent magnetic moment. Ferromagnetism was already known when ferroelectricity was discovered in 1920 in Rochelle salt by Valasek. Most materials are polarized linearly by an external electric field; nonlinearities are insignificant. This is called dielectric polarization. The electric permittivity, corresponding to the slope of the polarization curve, is thereby a function of the external electric field. In addition to being nonlinear, ferroelectric materials demonstrate a spontaneous polarization.[10] The distinguishing feature of ferroelectrics is that the direction of the spontaneous polarization can be reversed by an applied electric field, yielding a hysteresis loop. Ferroelectric crystals often show several transition temperatures and domain structure hysteresis, much as ferromagnetic crystals. A ferroelectric crystal shows a reversible spontaneous electric polarization and a hysteresis loop that can be observed in certain temperature regions,

delimited by a transition point called the Curie temperature, T_c. At temperatures above T_c, the crystal is no longer ferroelectric and exhibits normal dielectric behavior. Ferroelectric materials usually, but not always, exist in a non-polar state at temperatures above T_c, and have anomalously high dielectric constants, especially near the Curie temperature. The dielectric constant increases very rapidly to a very high peak value at T_c. The anomalously high value of permittivity (ε_r) in the neighborhood of T_c is generally referred to as the anomalous value. At $T > T_c$, anomalous behavior follows closely the Curie–Weiss relation where C is known as the Curie constant.

In fact, anomalous behavior always appears near any transition point between two different phases, even at T below T_c. At the transition points, there are anomalies not only in the dielectric constant and polarization, but also in piezoelectric and elastic constants and specific heat, because of the change in crystal structure. Ferroelectrics have reversible spontaneous polarization. The word spontaneous may mean that the polarization has a nonzero value in the absence of an applied electric field. The word reversible refers to the direction of the spontaneous polarization that can be reversed by an applied field in opposite direction. The spontaneous polarization P usually increases rapidly on crossing the transition point and then gradually reaches a saturation value at lower temperatures. The most prominent features of ferroelectric properties are hysteresis and nonlinearity in the relation between the polarization P and the applied electric field E.

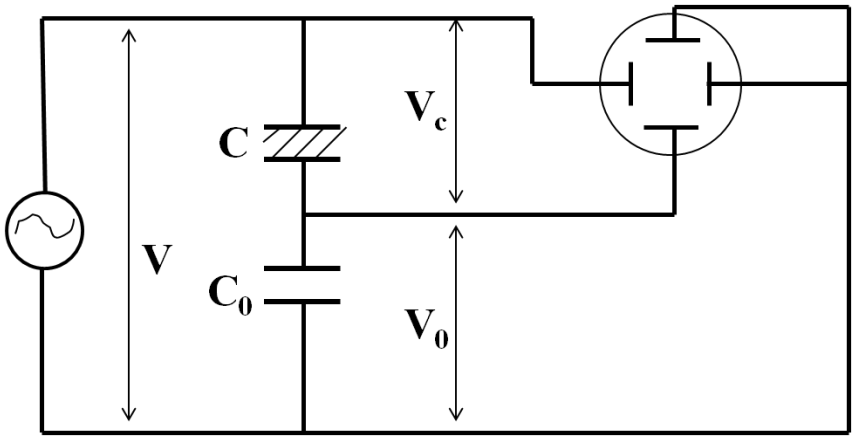

Figure 2.8: *The Sawyer -Tower method to measure the polarization-electric field characteristics.*

The Sawyer-tower method is the simplest method to measure the polarization. As shown in **Figure 2.8** here the ferroelectric capacitor C is kept parallel to a standard capacitor C_0. A sinusoidal voltage signal is applied to one of the electrodes of the ferroelectric capacitor and the amount of charge displacement in the other electrode is measured using the voltage it creates over a reference capacitor connected in series. The voltage V_0 sufficient to polarize the ferroelectric material

$$V_0 = \frac{AP}{C_0}$$

Where, A is the capacitor area, P is the polarization, V is applied ac voltage of low frequency with the applied field across the specimen as$E = \frac{V_c}{d} = \frac{(V - V_c)}{d}$, with d as the sample thickness.

Ferroelectricity analysis was carried out using aixACCT systems, GmbH Germany at ARDE, Pune.

2.9 References

1. W. W. Flack, D. S. Soong, A. T. Bell, and D. W. Hess, "A mathematical model for spin coating of polymer resists", *J. Appl. Phys.*, **1984,** 56, 1199.
2. Clark I. Bright, (Eds A. Facchetti and T. J. Marks) Transparent electronic from synthesis to application *1 edition, John Wiley & Sons Ltd*, **2010**, chapter 3.
3. http://en.wikipedia.org/wiki/Sputter_deposition.
4. Evgenij Barsoukov J. Ross Macdonald Impedance Spectroscopy Theory, Experiment, and Applications *Wiley-VCH, Hoboken, New Jersey*, **2005**.
5. Peter Stallinga Theory of electrical characterization of (organic) semiconductors http://www.stallinga.org/ElectricalCharacterization/2terminal/index.html.
6. Nathan Heston IPCE Monochromator User Guide Newport Oriel: (800) 714-5393.

7. Elements of X-ray Diffraction, ed. by B. D. Cullity, *Addison Wesley Publishing Co*., **1978**.
8. C. N. Banwell, E. M. McCash, A Book: Fundamentals of Molecular pectroscopy, 4th Ed., *Tata McGraw Hill Publishing Co. Ltd*., **2002.**
9. J. Coates, Interpretation of Infrared Spectra: A Practical Approach, Encyclopedia of Analytical Chemistry, R.A. Meyers (Ed.), 10815, *John Wiley & Sons Ltd*, **2000**.
10. K. Rabe, C. H. Ahn, J.-M. Triscone Physics of Ferroelectrics: A Modern Perspective, **2007**, 105, 1.

CHAPTER 3

A Quasi-Liquid Iontronic-Electronic Light Harvesting Hybrid Photodetector with Giant Response in UV-Visible

Here, we propose and demonstrate a novel photodetector design based on ZnO nanorods with surface dispensed agarose hydrogel which embodies the concept of an ionic-electronic hybrid system. The device fabrication reported is simple. It consists of hydrothermally grown aligned and dense ZnO nanorods on fluorine doped tin oxide (FTO) coated glass on which agarose gel is dispensed, and top contact is provided in the form of platinum tip electrode. This ZnO-gel device shows a remarkable enhancement (about three orders of magnitude) in photocurrent as compared to bare ZnO nanorods. The ZnO-gel hybrid device shows two order higher quantum efficiency in the presence of UV as compared to visible light spectrum. The quantum efficiency of the device enhances further by 20 times at the bias voltage of -2V. The optimized ZnO / agarose gel device shows rise time of about 250 ms as compared to 1.26 s in the bare ZnO system. The reset time is also reduced to 100 ms as compared to 1.02 s in bare ZnO. The observed giant enhancement in photo-response in ZnO / agarose gel device is explained on the basis of interface effects.

3.1 Introduction

Zinc oxide (ZnO) is a remarkable metal oxide that has attracted broad application interest in various fields.[1-3] It is a direct band gap semiconductor with a band gap of about 3.37 eV, high electron mobility of ~100 cm^2/Vs and exciton binding energy of 60 meV. It can be easily synthesized in various morphological forms due to its crystal growth habits that are amenable to synthetic manipulation. Substrate-supported 1D ZnO nanostructures can also be easily grown, but their incorporation into robust device systems is non-trivial due to issues related to the surface coverage of the functional over layers. An interesting approach to make a shape-conforming contact to such nanostructures is by using shape-adapting soft matter, which is transparent and conducting. It also opens up new opportunities to pursue novel science related to all-ionic or ionic-electronic hybrid systems. [4-11] For instance, in their interesting works Z. L. Wang and coworkers [4,5] have used polymer/polyelectrolyte coats to show significant performance enhancement in optoelectronic response of ZnO based device systems. Ionic liquids or gels also represent good candidates in this respect. Indeed recently there is a surge of interest towards developing ionic conductor based electronic devices which mimic biological system (neuron) in their operation. In their significant studies on gel based device systems Velev and coworkers[6-9] have used Agarose-based hydrogel, which has good ionic conductivity, biocompatibility and optical transparency, and shown applications to make a polyelectrolyte diode,[6] an ion current diode,[7] a memristor[8] and a photovoltaic device.[9] In other interesting studies on soft matter based devices Chung and coworkers[10] have also developed ionic circuits based on polyelectrolyte diodes, while Berggren and coworkers[11] have more recently reported on the development of NPN ion bipolar transistor.

In this work we demonstrate a highly efficient photodetector device covering UV and visible ranges based on the functionality of the interface between an inorganic solid and quasi liquid (gel) hetrostructure. The ZnO nanorods-agarose gel heterojunction was made by putting a drop of agarose solution on ZnO nanorod array film and allowing it to cool to room temperature (gelification). Such ZnO-gel device was seen to exhibit 3 orders of magnitude enhancement in photoresponse as compared to only ZnO array film.

3.2 Experimental Section

The ZnO nanorods array is grown using a simple chemical method employing a protocol previously reported.[12] The seed solution is prepared by stirring 5 mM zinc acetate in ethanol until it gets slightly milky white colored. It is deposited on fluorine doped tin oxide (FTO) coated glass substrate by spin coating at the rotation speed of 2500 rpm for 30 sec. These seed coated substrates are annealed at 300 ^{o}C for 1h for better adherence of ZnO nanoparticles which act as nucleating sites for the growth of ZnO nanorods. For the facile growth of ZnO nanorods, an equimolar (25 mM) solution of zinc nitrate hydrate, hexamethylene tetramine (HMT) and 5 mM polyethylenimine (PEI) is used for the reaction. In closed glass container, the seeded substrates are immersed into the solution with the seeded side facing the bottom of the glass container. Further the container is heated at 95 ^{o}C on the magnetic heater-cum-stirrer for three hours. The sample substrates are taken out and then rinsed with distilled water. After the reaction is complete, the grown ZnO NRs are thoroughly rinsed with Milli-Q water and dried in air to remove residual polymer. Longer ZnO NRs (7-9 μm) can be produced by repeating the above growth process in a fresh aqueous precursor solution for three times. Finally, the deposited samples are kept for annealing at 300 ^{o}C for 1h for better adherence of ZnO nanorods on the substrates.

The agarose gel is prepared by mixing agarose (2 wt %) in D. I. water by continuous stirring and boiling the solution on a hot plate. When the agarose is completely dissolved the gelation occurs by cooling the solution to room temperature.

3.3 Characterization

The samples were characterized by X-ray diffraction (Philips X'pert pro), Diffused reflectance spectroscopy (DRS), Scanning electron microscopy (SEM FEI, Quanta 200 3D), and electrochemical impedance spectroscopy (EIS, Autolab PGSTAT 30). The I-V characteristics were recorded by Keithley 2400-c source meter. To measure the photo-conductance, solar simulator (Newport) at 100mW/cm^2 AM1.5 and UV light

source (Hamamatsu) operated at 100 mW/cm^2 were used. The film thickness was measured with Dektak surface profilometer. The quantum efficiency was measured with Newport IPCE measurement setup.

3.4 Results and Discussion

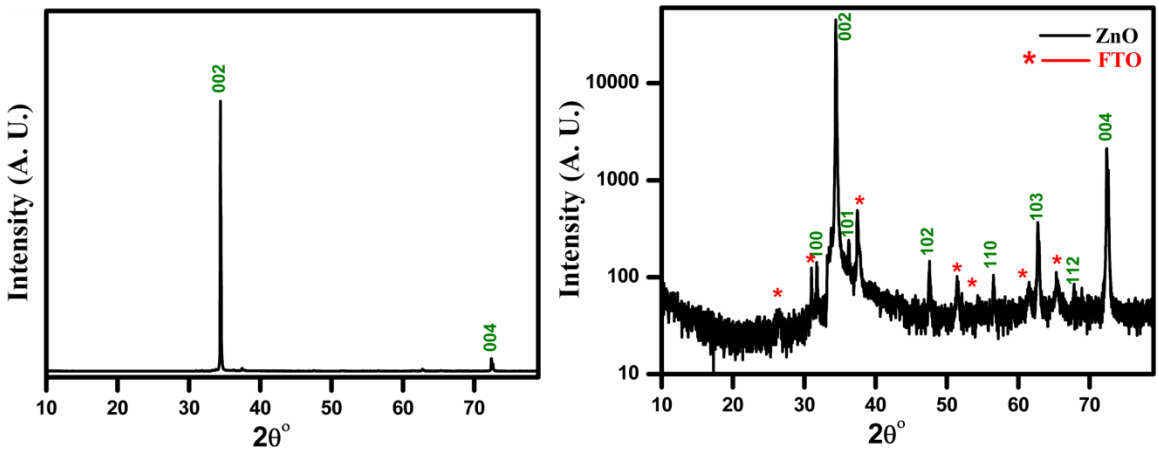

Figure 3.1: *XRD of ZnO nanorods linear and semi-log plot.*

Figure 3.1 shows the X-ray diffraction pattern which reflects that the nanorods are primarily vertically oriented as shown by a differentially higher intensity of (002) family of planes. However, when the XRD intensity is plotted on the log scale to highlight smaller contributions signatures of other planes are noted; which implies that the vertical alignment is not perfect. **Figure 3.2** shows the cross section SEM image which confirms the primarily vertical alignment.

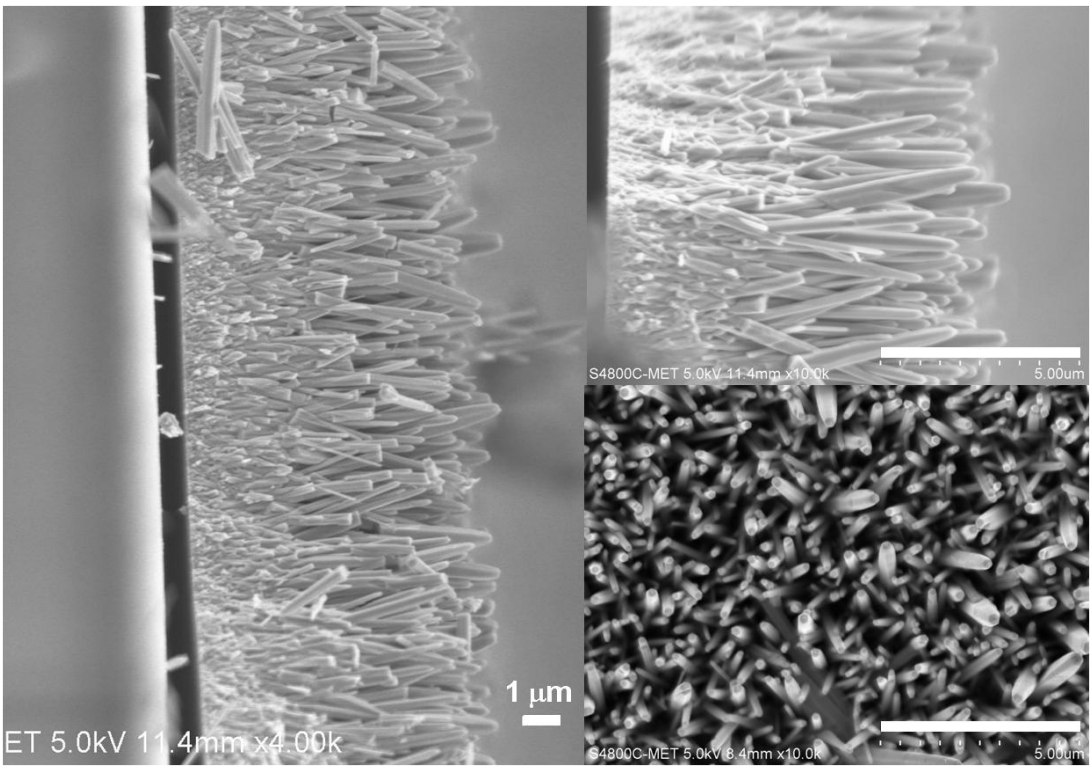

Figure 3.2: *Cross-sectional SEM of ZnO nanorods.*

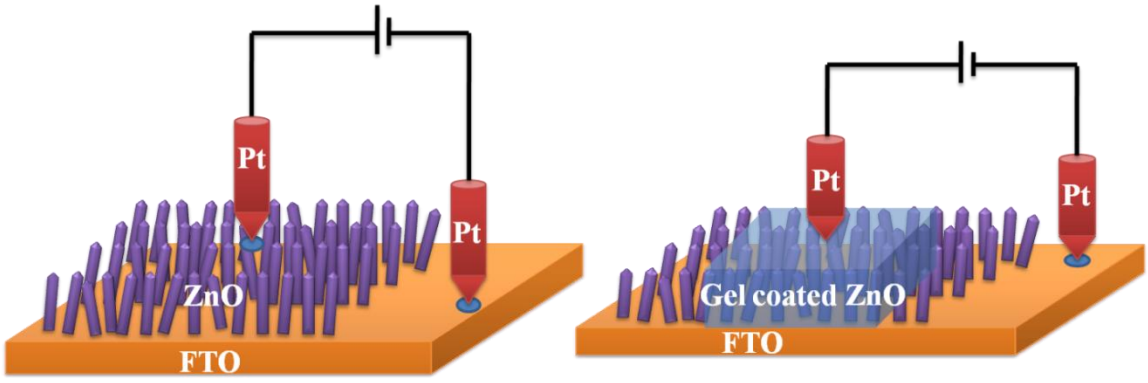

Figure 3.3: *Device architecture of the respective system.*

The device structures of ZnO-Pt and ZnO-agarose gel-Pt studied in this work are illustrated in the **Figure 3.3** respectively. A FTO coated glass serves as the bottom electrode and a platinum tip acts as the top contact. For the electrical measurements (room temperature) the FTO coated glass is always kept grounded and the potential is

applied to the platinum tip. It is useful to mention contact properties were examined separately for the Pt-FTO and Pt-gel cases. In this case the I-V characteristics were studied with two Pt contacts made to FTO in one case, and two Pt contacts made on the top of gel surface supported on normal glass slide. The I-V characteristics were recorded as a function of the distance between the two contacts. The characteristics are shown below in **Figure 3.4** As expected the Pt-FTO contact is Ohmic while the Pt-gel contact is non-Ohmic. The extrapolation of the graph to zero inter-electrode distance reflects the contact resistance.

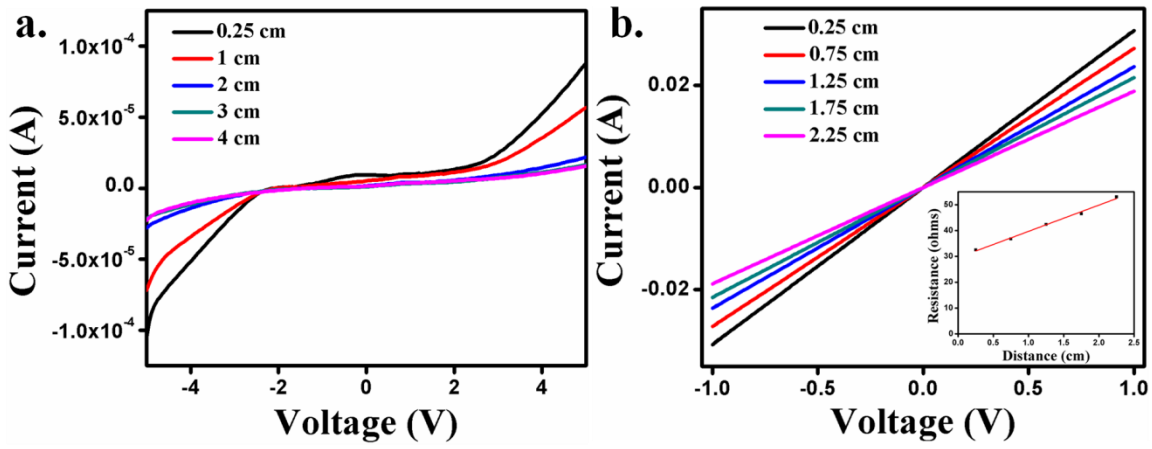

Figure 3.4: *The I-V characteristics of the top and bottom contact junctions:* ***a****. Pt-agarose gel and* ***b****. Pt –FTO inset show resistance as function of contact distance in Pt-FTO case.*

Figure 3.5 a and **b** show the I-V characteristics for the ZnO-Pt interface and the ZnO-gel-Pt system, respectively, under dark and under AM1.5 1 Sun illumination (100mW/cm^2). In dark the slight non-linearity of the I-V curve (see the **Figure 3.6** which shows the dark current on a linear scale for clarity) in the case of ZnO-Pt interface indicates that the contact between ZnO and Pt is Schottky type.[13] The presence of agarose gel modifies the characteristic, making it more rectifying (**Figure 3.5 b**). The dark current is also seen to be higher in the ZnO-gel-Pt case as compared to the ZnO-Pt case. It can be seen that in sweeping the bias from -5V to +5V (+5V to -5V) in the dark, the current minimum occurs in between -1V to -2V (+1 to +2V), respectively, whereas under illumination it occurs at 0V. This shift can be attributed to the solid /quasi-liquid (i.e.

ZnO / agarose gel) nature of the heterojunction. The attendant electrical (electronic-ionic) discontinuity at such an interface leads to a space charge region inside ZnO, an electric double layer at the interface and diffused charge layer in the gel due to electron ion imbalance.[14] These result in different capacitances which lead to the formation of accumulation, depletion and inversion regions inside the semiconductor in the dark.

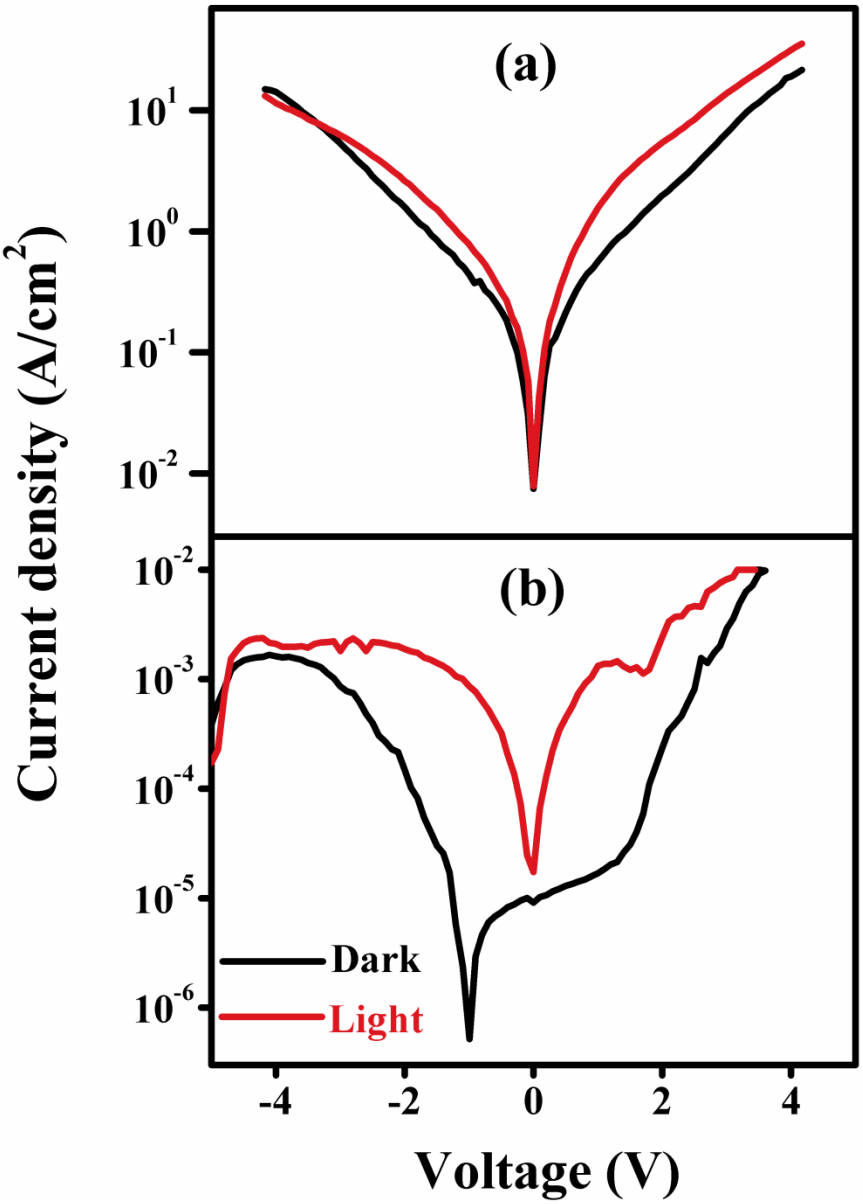

Figure 3.5: *I-V under Dark and AM1.5 1 Sun illumination of* ***a****. ZnO-Pt and* ***b****. ZnO-gel-Pt systems.*

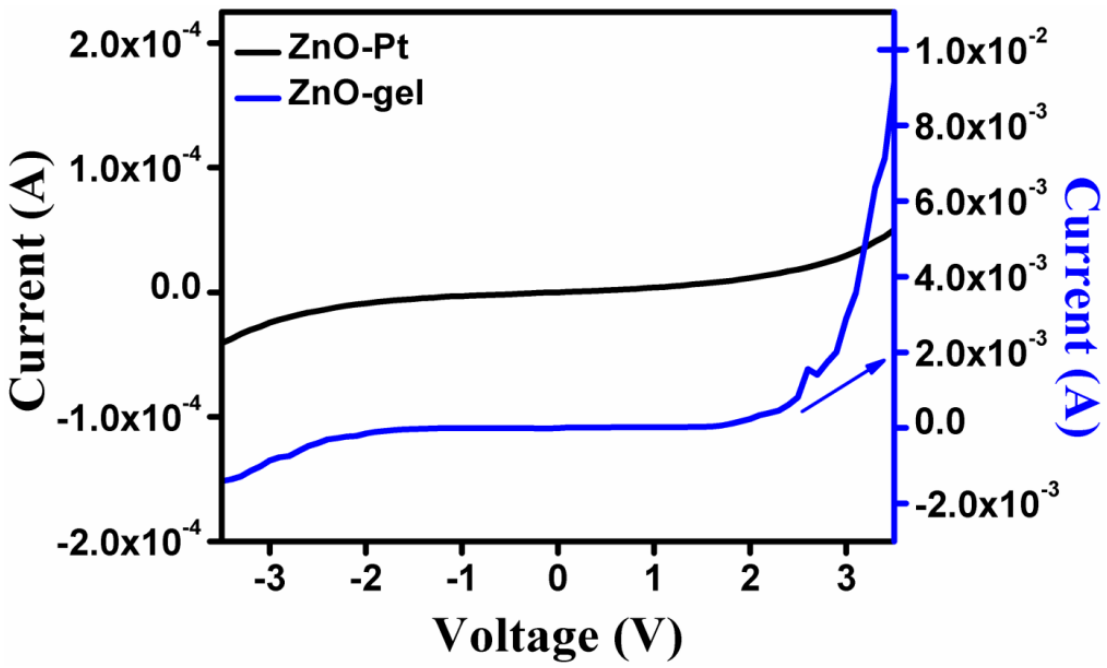

Figure 3.6: *I-V (linear-linear) plot under dark for ZnO-Pt and ZnO-gel-Pt system.*

When this interface is illuminated high density of electrons and holes is generated which changes the interface charge distribution, thereby dramatically reducing the capacitances of the interface regions and shifting the current minimum to 0 V. Since, the current minimum in the ZnO-gel-Pt occurs at around -2 V maximum photoresponse can be obtained for this bias. Interestingly, the ZnO-gel-Pt system even shows a photovoltaic characteristic curve under solar illumination with open circuit voltage of 0.24 V and short circuit current of 5 $\mu A/cm^2$.

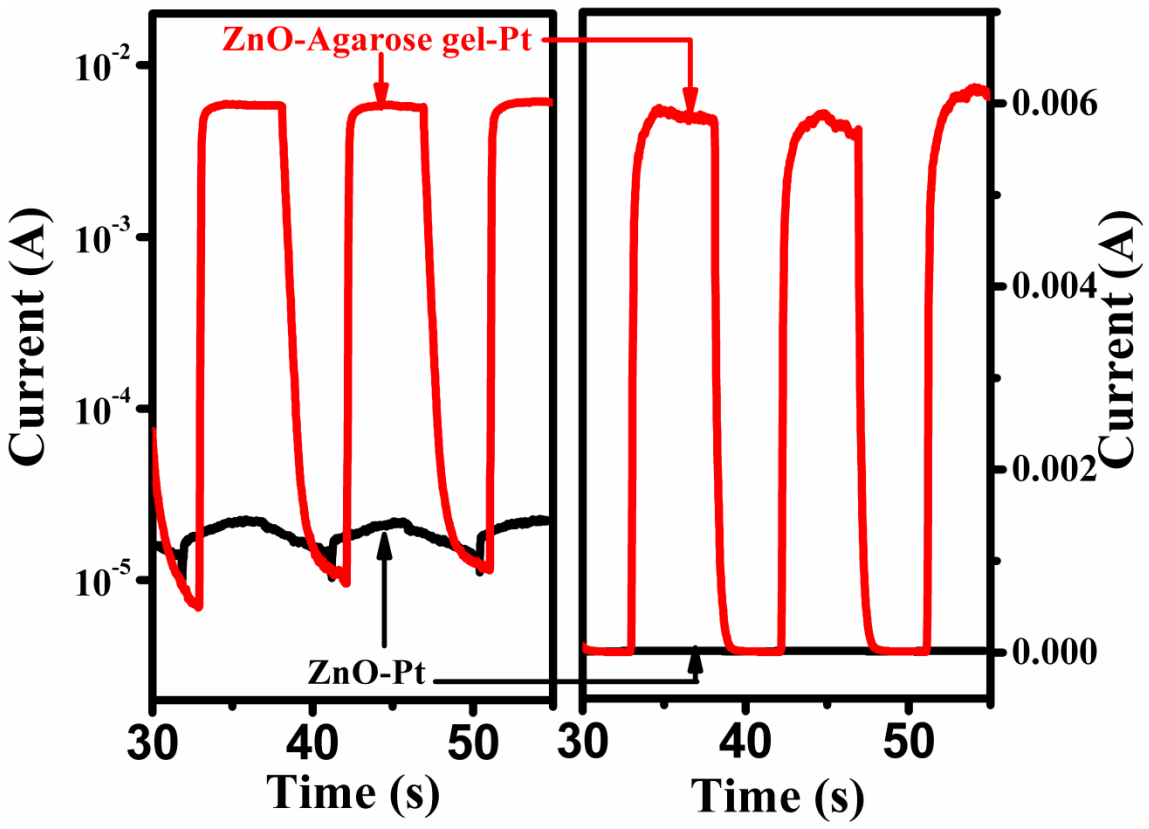

Figure 3.7: *Photoresponse as a function of time with light chopping in semi-log and linear plot under AM1.5 1 Sun illumination.*

Figure 3.7 shows the photocurrent response as function of time for the ZnO-Pt and ZnO-gel-Pt systems; the response being plotted on the log scale. The same data with the response plotted on the linear scale is presented in right part of the graph. The light source was manually chopped for 5 sec duration. The data represent the current at an applied voltage of -2 V. The light source used was a solar simulator (AM1.5 1 Sun, 100 mW/cm^2). Upon illumination the current enhances by a factor of 2 in bare ZnO-nanorods case, while in ZnO nanorods-gel-Pt case it increases by almost three orders of magnitude. The sample to sample variation of this result was also examined on a set of independently prepared samples and the enhancement was found to be fairly robust as reflected by the variation shown in **Figure 3.8**. Given the band gap of ZnO of 3.4 eV (UV regime) such strong response in the visible is remarkable and surprising. To make sure that this enhancement is not due to agarose gel itself the photoresponse of gel sandwiched

between ITO-glass and Pt-tip was also recorded. Upon illumination the current increases but only by a factor of 2. Thus, the low photoresponse in the cases of bare ZnO and the agarose-gel confirms that the enhanced heterojunction photoresponse is due to the interfacial effect between the ZnO-nanorods and agarose-gel.

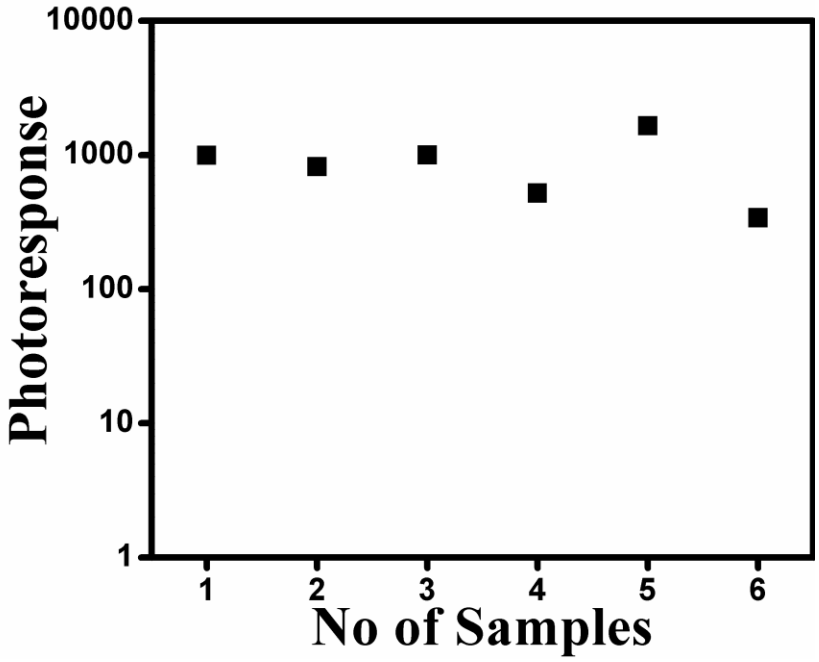

Figure 3.8: *The statistical data of photoresponse*

Interestingly, the photoresponse of this ZnO-gel device is almost comparable for visible (AM1.5) and full-UV illumination of ~100 mW/cm^2. At higher intensities, all deep lying surface states can be probed and saturation can occur,[15] hence we also measured the photoresponse at low intensity ~10 mW/cm^2 (0.1 Sun). **Figure 3.9** shows the response of ZnO-gel-Pt photodetector for 100 and 10 mW/cm^2 at -2V bias. At 10 mW/cm^2 the response of the detector for UV is almost twice that for visible showing the expected dominance of inter-band transition and non-saturation of response at low intensity.

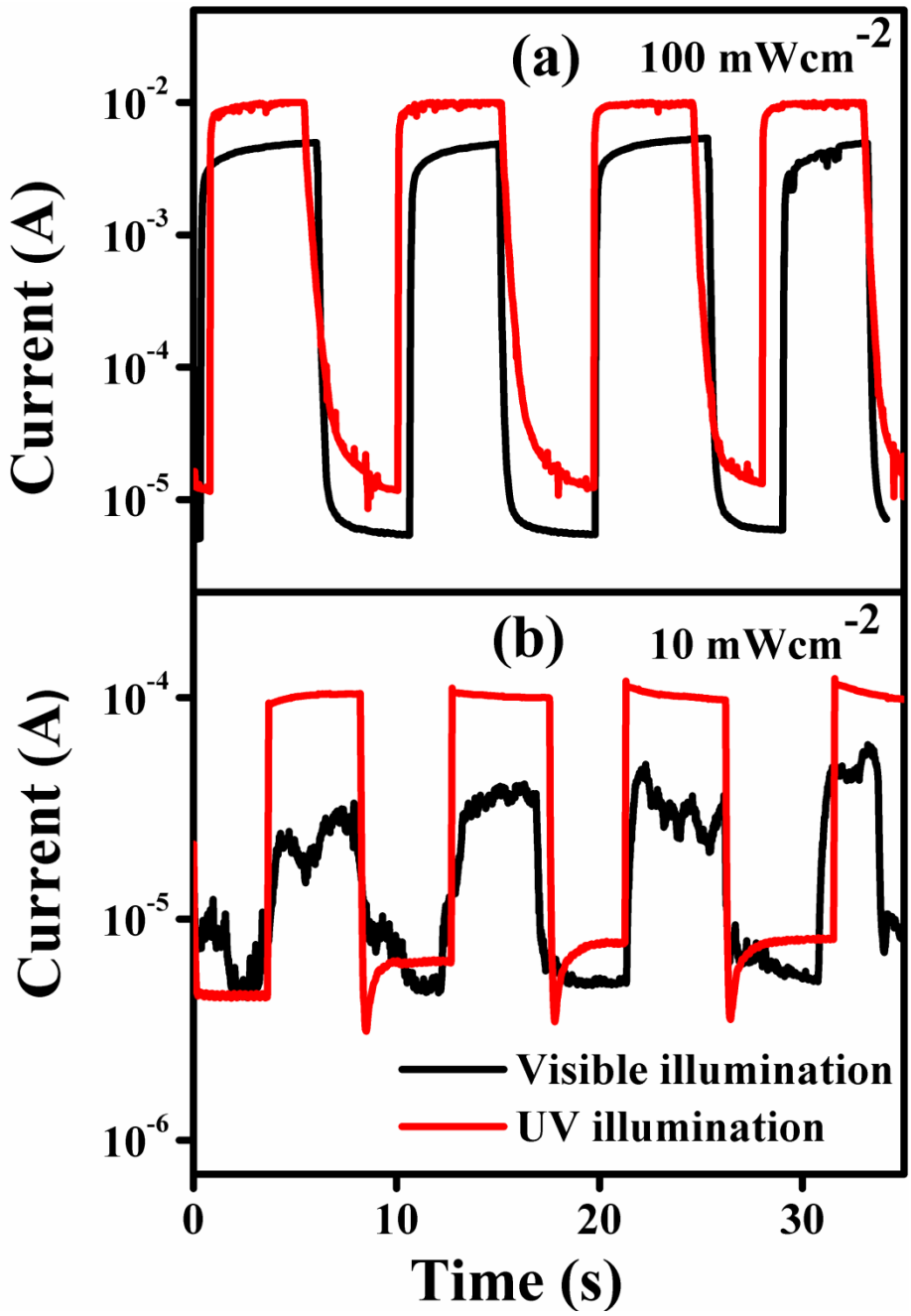

Figure 3.9: *UV and visible response of ZnO-Agarose gel-Pt photo-detector for illumination intensity of* ***a****. 100 mW/cm^2 and* ***b****. 10 mW/cm^2 at an applied bias of -2V in semi-log.*

To understand the electronic properties and the interface effects in the ZnO-gel system, electrochemical impedance spectroscopy was performed in the dark and under AM1.5 1 Sun illumination on the three electrode system in the frequency range of 10

mHz to 10^6 Hz at 10 mV ac voltage. **Figure 3.10**. shows the Nyquist plot. We fitted the obtained data into an equivalent circuit shown in the inset of **Figure 3.10** and the fitted parameters are given in **Table-1**. The Rs obtained at high frequency represents the total contact resistance in the circuit. Its value is almost constant in the dark and under illumination. In the dark the impedance plot shows one semicircle in high frequency region and a roughly straight (slightly bowing) line over the low frequency regime (implying a highly extended second semicircle). In the high frequency regime the agarose gel acts as an insulator because the ions cannot respond to such frequency. This semicircle at high frequency must therefore represent the interface impedance of ZnO with effectively insulating agarose, and the straight line in the low frequency region represents the impedance of the interface between ZnO and agarose-gel with enabled ionic conduction.[16]

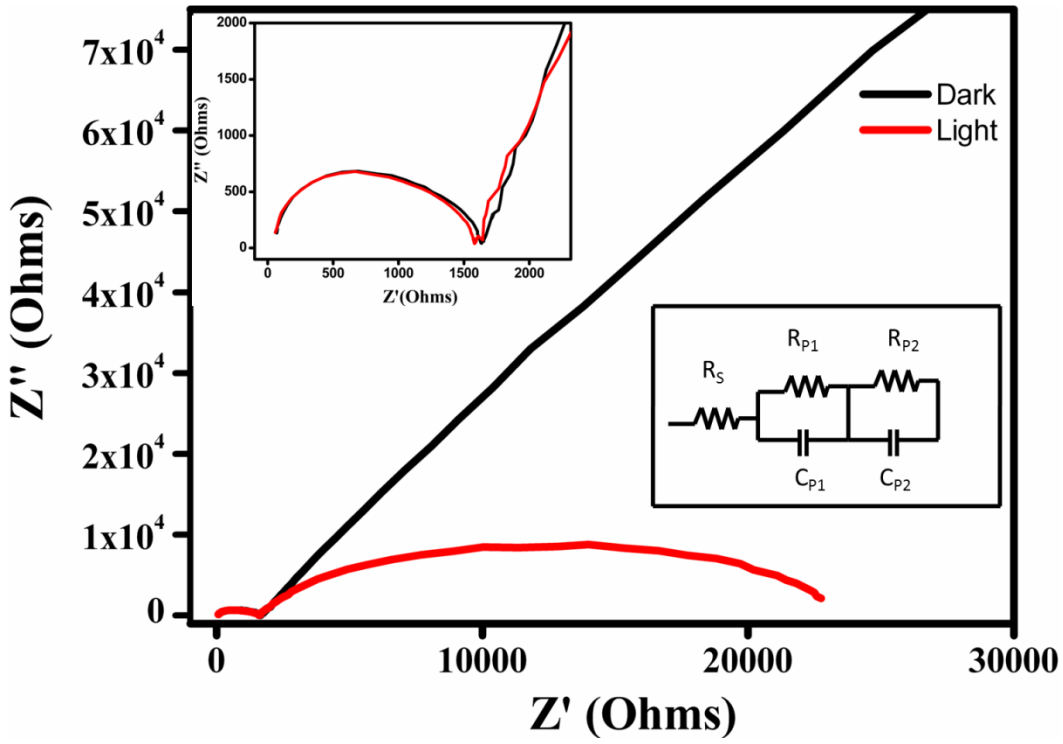

Figure 3.10: *Impedance plot of ZnO-agarose gel-Pt under dark and AM1.5 1 Sun illumination. Insets show magnified response at high frequency and fitted equivalent circuit.*

Under illumination the impedance plot shows two complete semicircles, the first one at high frequency is exactly the same as that for the dark case (magnified in the inset, top left) confirming that it represents the interface aspects which do not respond to light. In low frequency region, the diameter of the 2nd semicircle in the dark reduces dramatically in the presence of light. It shows an overall decrease in the capacitance as well as the resistance of the interface, as seen from the fitted equivalent circuit parameters. The second semicircle gives R_{P1}, the charge transfer resistance, and its value is drastically reduced from 227 kΩ in dark to 18.8 kΩ under illumination. This can be attributed to the highly efficient photogeneration and separation of the charge carriers which decrease both the resistance and the capacitance.[17]

	R_S [Ω]	R_{P1}[kΩ]	R_{P2} [kΩ]	C_{P1}[μF]	C_{P1}[nF]
Dark	**58.9**	**227**	**1.61**	**54.2**	**1.21**
Light	**49**	**18.8**	**1.55**	**41.5**	**1.22**

Table 1: *Fitted impedance parameters.*

In order to investigate the flat band potential we measured capacitance-voltage (C-V) characteristics and examined the Mott-Schottky plots.[18-20] In Mott Schottky plot $1/C^2$ is plotted against the applied potential. The intercept of linear portion of $1/C^2$ on the x-axis gives the value of the flat band potential, the slope of the curve gives the charge carrier density, and the width of space charge layer can be calculated by Mott-Schottky equation which is:

$$\frac{1}{c^2} = \left(\frac{2}{e_0 \varepsilon \varepsilon_0 N_d}\right) q[(V - V_{FB}) - \frac{kT}{e_0}]$$

The charge density can be calculated by,

$$N_d = \left(\frac{2}{e_0 \varepsilon \varepsilon_0}\right) \left[\frac{\mathrm{d}\left(\frac{1}{\mathrm{C}^2}\right)}{\mathrm{dV}}\right]^{-1}$$

The width of the depletion layer at the interface between the semiconductor and electrolyte interface can by calculated by,

$$W = \sqrt{[\frac{2\varepsilon_0 \varepsilon (V - V_{FB})}{e_0 N_d}]}$$

where, ε_0 is permittivity of free space, ε is the dielectric constant of ZnO, e_0 is electronic charge, N_d is carrier density, and V_{FB} is the flat band potential. The calculated value of flat band potential is 0.4 V. The positive slope of Mott-Schottky plot shows that the as grown ZnO is n-type, as expected. The calculated carrier density in the ZnO nanorods in the presence of agarose gel is 3.8×10^{16} cm^{-3} which is comparable to that in hydrothermally grown ZnO nanorods.[21,22] The width of the depletion layer comes out to be 21.5 nm which is smaller than the diameter on ZnO nanorods, which shows that the nanorods are not fully depleted.

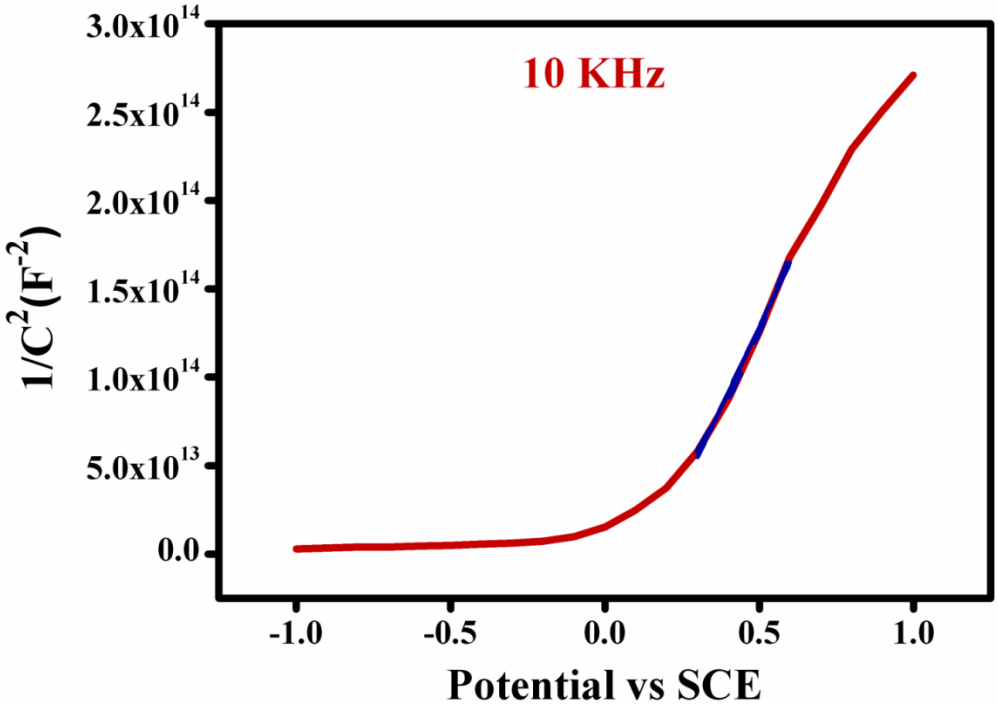

***Figure** 3.**11:** Mott Schottky plot of ZnO-agarose gel in dark at 10 kHz.*

Figure 3.12 shows the incident photon to current conversion efficiency (IPCE) in the spectral range of 350-800 nm for the photodiode based on ZnO-gel-Pt system at different values of applied bias. For the measurement of IPCE, almost transparent platinized FTO (Pt-FTO) was used (instead of Pt tip) as the top electrode. Platinized FTO was prepared by drop casting H_2PtCl_6 on clean FTO and then annealing at 400 ˚C for 10 minutes. **Figure 3.13** shows the schematic of sample preperation procedure and the photoresponse as a function of time with light chopping in semi-log with platinized FTO as top contact.

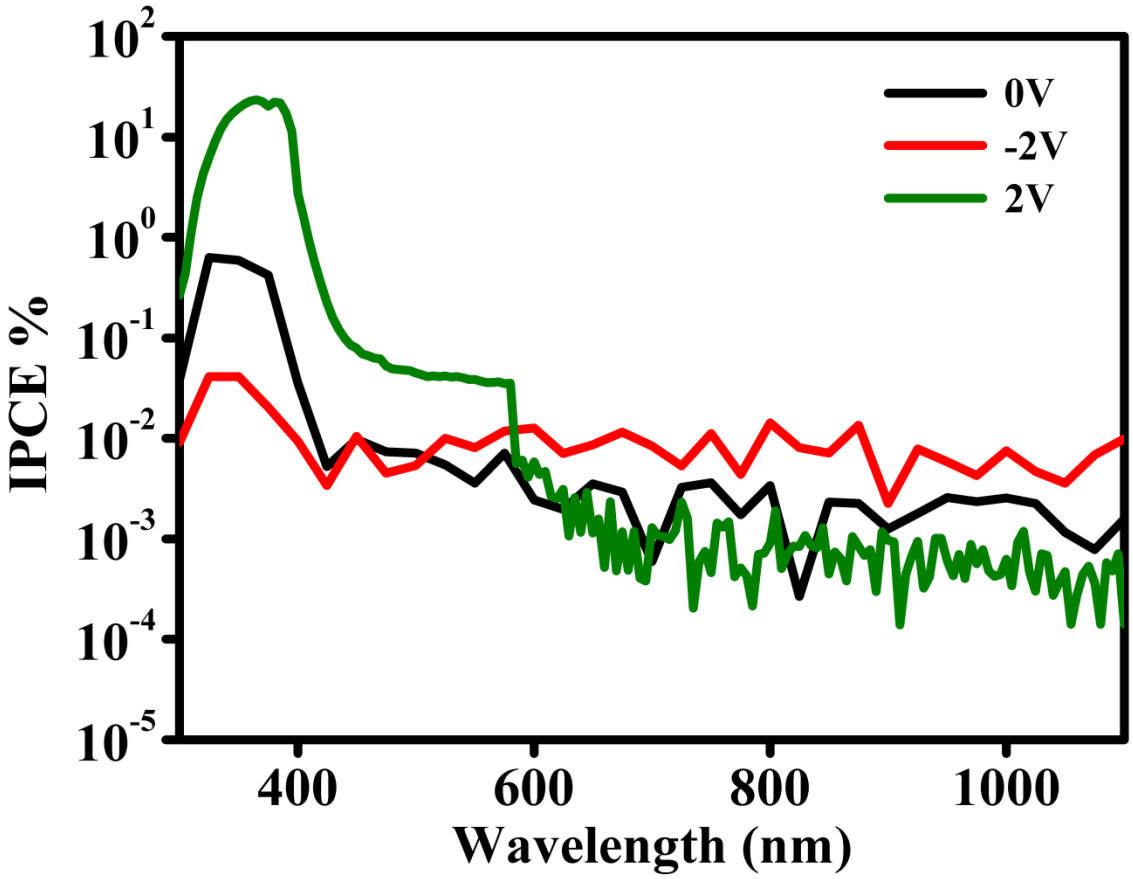

Figure 3.12: *Incident photon to current conversion efficiency (IPCE) data plotted at semi-log scale for ZnO-agarose gel under applied potential of 0 V, 2 V and -2 V in semi-log.*

As seen, the photoresponse with this top electrode is also comparable to that with Pt tip. The IPCE of the diode shows almost 2 orders of magnitude stronger response in UV (350-400 nm) than in visible under 0 and -2 V bias. The IPCE is > 1 order lower for 2 V bias as compared to 0V bias. On the application of -2 V more charge carriers are generated due to direct creation of separated electrons and holes across the interface or highly efficient ionization of created excitons.[23] Under application of reverse bias and illumination to a Schottky system, the photogenerated electron-hole pairs are known to separate efficiently under the local generated field, decreasing the recombination rate and increasing the carrier lifetime.[5] Most interestingly, there is one order of magnitude enhancement in the IPCE of the ZnO-gel system over the visible spectral regime of (400-600 nm) upon application of a bias of -2V.

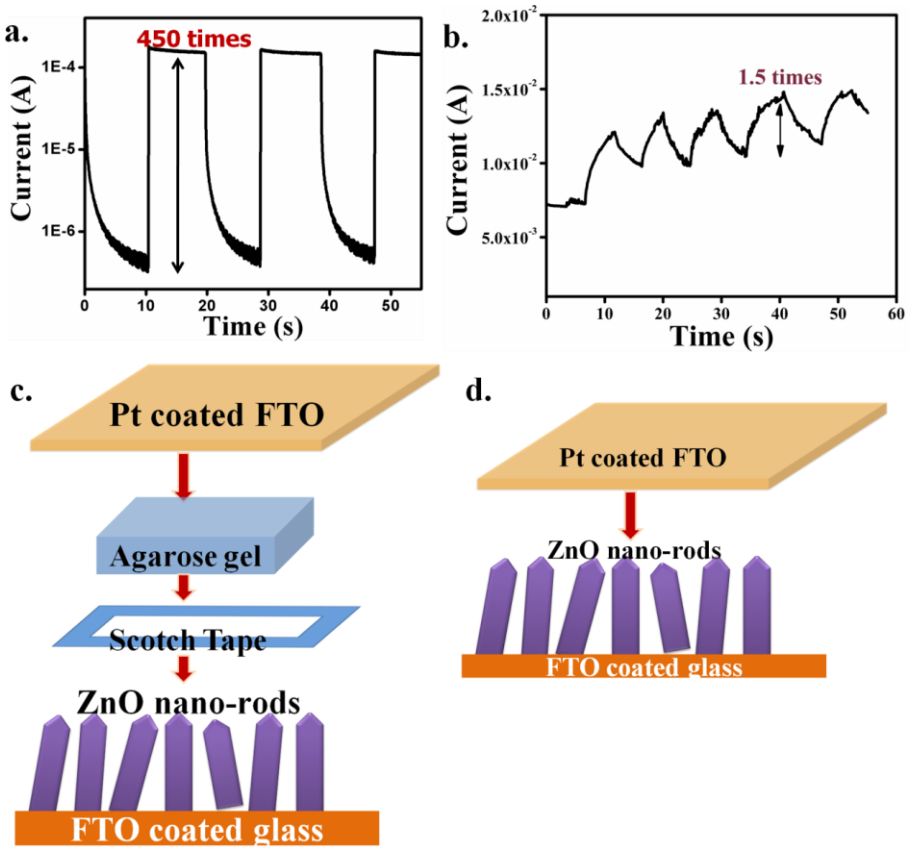

Figure 3.13: *Photoresponse as a function of time with light chopping in semi-log plot* ***a****. ZnO-gel-Platinized FTO* ***b****. ZnO-Platinized FTO* ***c****. Schematic of ZnO-gel with platinized FTO* ***d****. Schematic of ZnO with platinized FTO.*

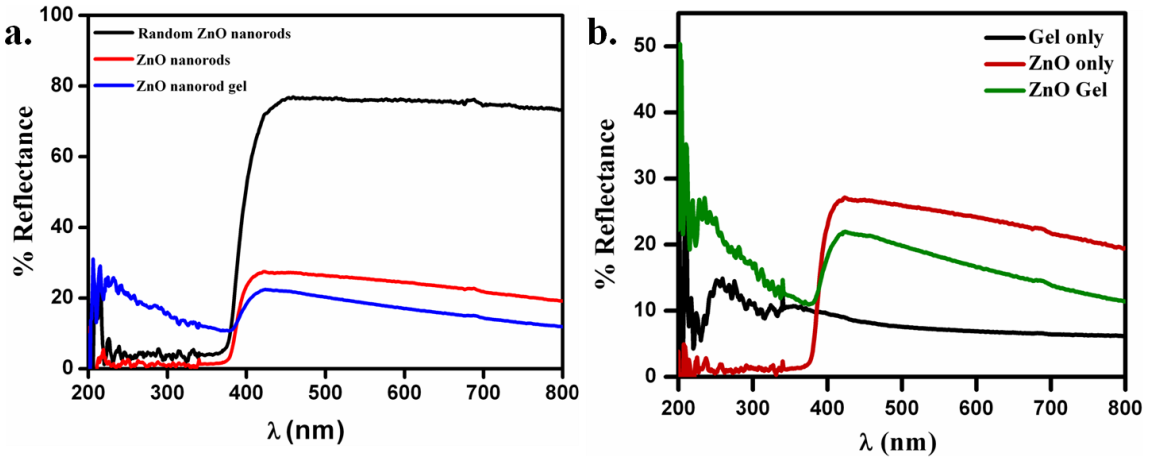

Figure 3.14: *a. Diffused reflectance spectra (DRS) of randomly oriented, vertically aligned on the substrate, and the vertically aligned ZnO nanorods-gel system; b. Diffused reflectance spectra of agarose gel, ZnO nanorods and ZnO nanorods-agarose -gel.*

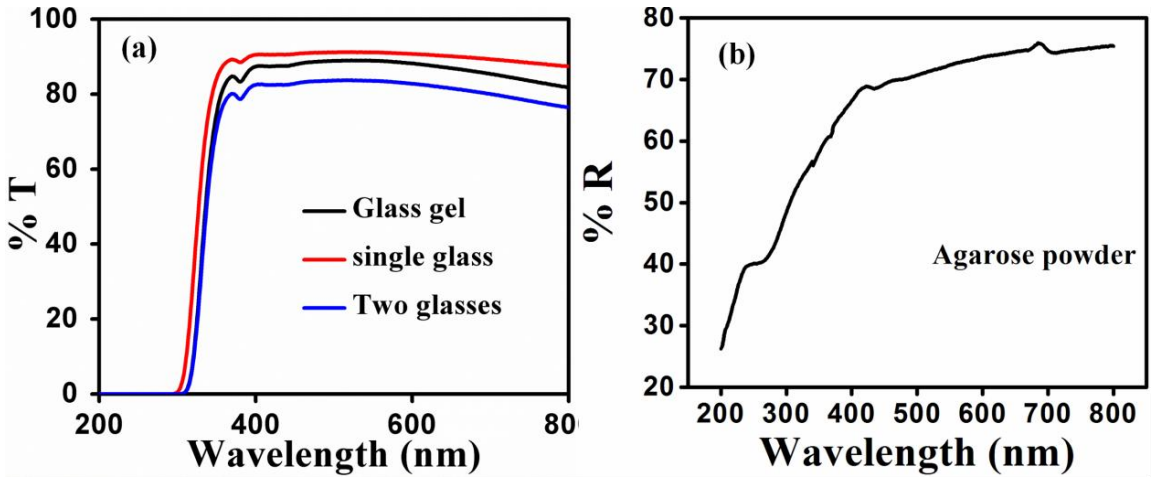

Figure 3.15: a*. Tranmittance of agarose gel sandwiched between two normal glass* ***b****. DRS of agarose polymer.*

Pure ZnO nanorods, the agarose gel and the unbiased ZnO-gel system do not absorb the visible light as confirmed by the DRS spectra shown in the **Figure 3.14** and the optical transmittance data shown in **Figure 3.15 a**. The DRS of the agarose powder itself (which forms 2% component in the gel) is also shown in **Figure 3.15 b**. Interestingly on application of a bias of -2 V (to Pt top contact) the IPCE leads to a tail in

visible. While ZnO expectedly shows a UV photoresponse, its visible photoresponse with the gel interface is interesting indeed. Surface defects on ZnO nanorods, especially oxygen vacancies, play an important role in this visible photoresponse,[24] as also shown by theoretical studies.[25] Multiple reflections inside the quasi 1D nanostructure with oxygen vacancies enhance the effect further (light harvesting).[26] Comparison of the DRS spectra for aligned nanorods and doctor-bladed nanorod film shown in **Figure 3.14 a** clearly establish that the aligned nanorods absorb far more light compared to the randomly oriented nanorods. The differences in the degree of scattering between the two cases of oriented nanorods, one without gel and another with gel can be attributed to the fact that the gel refractive index (~1.33 since it is 98% water) is intermediate between that of ZnO (~2) and air (~1).

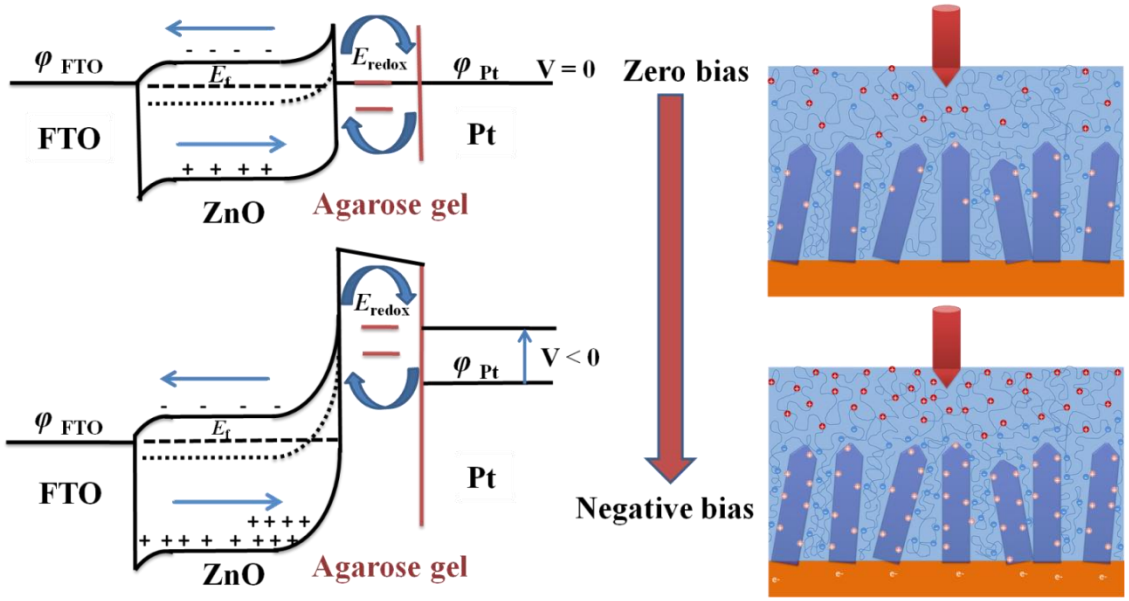

***Figure** 3.16: Energy band diagram and schematic of FTO-ZnO-agarose gel-Pt system at zero and negative bias.*

Figure 3.16 depicts the scenario at ZnO-gel interface at 0 bias and how it modifies with bias. A schematic is also included. Since the Schottky junction is reversed biased i.e. the conduction band moves upward in ZnO, the holes in ZnO move towards the interface. The holes are known to be high energy species that can extract electron from the

electrolyte [27] i.e. the nearby adsorbed OH^- ion on the ZnO surface will give its electron to ZnO. Another possible reason could be that the electric double layer at the interface can create a high field (as in electrolyte gated FETs), causing depletion of electrons from the ZnO surface.

If the applied field (-2 V bias) on the gel is high enough it can even extract the electron from the trap states, which are formed due to oxygen vacancies rendering them free. Under visible illumination the exciton can form between valence band and trap state. Since the trap states lie in the forbidden gap of ZnO they can absorb light in the visible region i.e. free trap states push the Fermi energy of ZnO to the middle leading to charge transfer exciton which can occur in the visible. Electric field is known to enhance the defect-related visible PL of ZnO nanoparticle electrolyte interface due to band bending.[28]

Now we briefly summarize the proposed mechanism of operation of the ZnO nanorods array-gel based photodiode: The interface between the ZnO nanorods and agarose gel is controlled by the Fermi level of ZnO nanorods and redox potential of the gel electrolyte. As the Fermi level of ZnO and the redox potential of the gel are different there will be charge flow across the interface from ZnO to the electrolyte creating band bending in ZnO (depletion in ZnO). The Mott-Schottky plot confirms the same with the barrier height of 0.4 V (**Figure 3.11**). When negative bias is applied through the platinum tip an electric double layer is created with accumulation of OH^- around ZnO, enhancing the depletion region in ZnO with the ZnO-gel interface behaving as a schottky diode (or MIS in depletion). Under illumination electron-hole pairs are created in the ZnO. If these are created away from the depletion region recombination probability is high, whereas if they are created within the depletion region they can be effectively separated by the built-in potential.[29] The electrons will be transported through the ZnO nanorods themselves whereas the holes will move to the ZnO-gel interface. This will result in the oxidation of OH^- ions at the interface. Similarly, when positive potential is applied accumulation of H^+ ion will occur at the ZnO-gel electrolyte interface and these will combine with the electrons at the interface leading to no or negligible charge separation.

The photoconductive gain for a photodetector is defined as the ratio of photogenerated charges collected per incident photon. The photoconductive gain is calculated as[30]

$$G = \frac{\Delta I \, h\upsilon}{P_{opt} e}$$

Where ΔI is photocurrent, P_{opt} is absorbed optical power (which is calculated using standard spectral power density[31] and absorbance of ZnO gel data). $h\upsilon$ is the energy of incident photon and e is electronic charge. The gain is calculated for a wavelength of 375 nm. The calculated photoconductive gain for ZnO-gel system at -2 V is approximately 4 for the wavelength of 375 nm. The gain is due to efficient separation of charge carriers at the interface between ZnO and gel.

The rise time is defined as the time taken by the photodetector to reach 90% of maximum photocurrent and the reset (recovery) the time taken to reach 1/e times (37%) of the maximum photoresponse current.[32,33] The response times for the cases of bare ZnO and ZnO-gel systems were also studied and the data are shown in the **Figure 3.17**. The ZnO-Pt device under AM1.5 1Sun follows exponential growth and decay, with the rise time of ~1.25 s and reset time of ~1 s. The rise (reset) time in this hybrid device is much faster, ~250 ms (~100 ms). The response time of the ZnO-gel-Pt photodetector is in fact better than the other reported photodetectors.[5,34] The photoresponse in ZnO is attributed to adsorption and de-absorption of oxygen molecules.[35,36] In the dark the oxygen molecules are known to adsorb on the surface of zinc oxide. By taking electron from the surface of zinc oxide they deplete the surface thereby decreasing the conductivity. Under illumination charge carriers are generated, and due to the presence of local field of the depletion layer the photogenerated holes move to the surface and the oxygen, thereby increasing the conductivity. The observed fast response of ZnO-gel device can be attributed to the water present in the gel.[34] Water is known to shorten the photoresponse time as it can take both electron or hole from the ZnO surface and it is more effective in negotiating with the oxygen vacancy in ZnO than O_2. The improvement in photoconductance can also be due to the Schottky contact which shows better photodetector performance.[5,13] An interesting question to ask is whether gel plays any role other than holding water mechanistically (gel is 2% polymer molecules and 98%

water). We performed related experiments and found that water also gives a good photoresponse, but the gel-based device shows a doubly stronger response. To study the difference between agarose gel and pure water; the device as shown in schematic of **Figure 3.13** was used, and then water (in one case) or agarose gel (in the second case) was added on the surface of the ZnO nanorod film. Interestingly, in the ZnO-nanorod-gel case the photoresponse was found to be 450 times, while that in the only water case was found to be 240 times as shown in **Figure 3.18**. The magnitude of photoresponse in the ZnO-nanorod-gel system is clearly much higher than that for the ZnO-nanorod-water case. This brings out the specific role of water supported by the gel molecular backbone structure in the photoresponse. The results show that Agarose not only acts as a medium to hold the water intact mechanistically, but with its more ionic conductivity than pure DI water, adds to the response as well. The agarose back bone contains negative charges [9] that increase the density of corresponding counter ions, thereby positively affecting the ionic double layer properties of interest. The response time was compared for the cases on pure water and the gel. The response time was found to be fairly comparable i.e. in the gel case the rise (reset) time was found to be 114 ms (36 ms), while in the water case the rise (reset) time was obtained as 87 ms (63 ms).

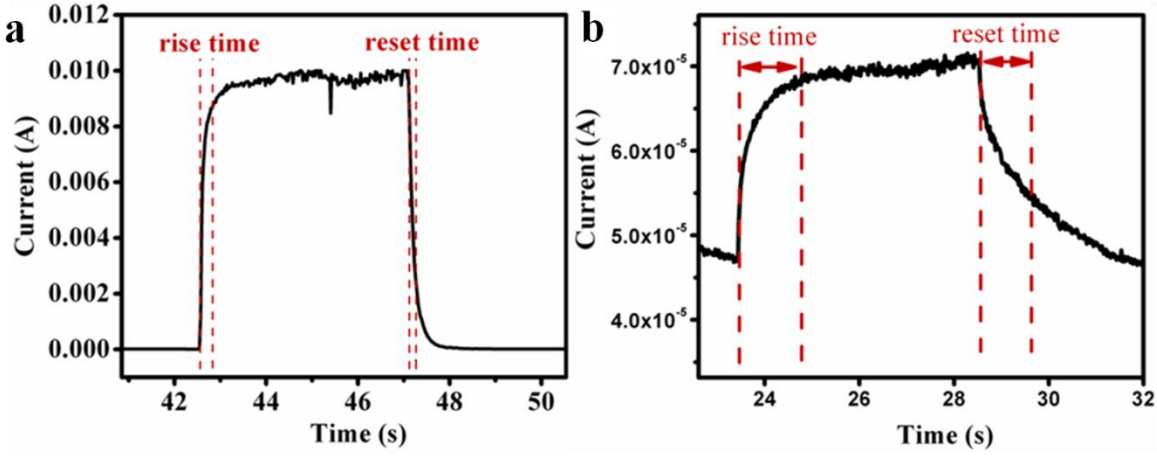

Figure 3.17: *Rise and reset time of **a**. ZnO-agarose gel-Pt **b**. ZnO-Pt systems*

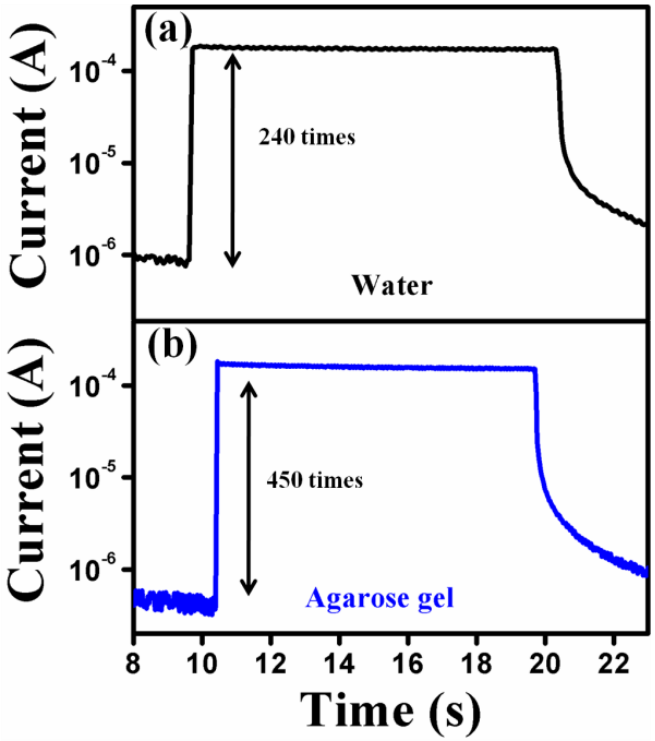

Figure 3.18: *Photoresponse as a function of time with light chopping in semi-log plot* ***a****. ZnO-water- platinized coated FTO,* ***b****. ZnO-gel- platinized coated FTO.*

To make a robust and realistic device the ZnO nanorods were covered on all the sides by ~70 μm scotch tape (as for other devices such as dye sensitized solar cells) and then agarose gel was dispensed on the surface of the ZnO nanorods. Other sealants or sealing strategies are also possible. Finally, Pt-FTO was applied as a top contact, instead of a Pt tip. **Figure 3.19** shows the schematic of this device and the corresponding photoresponse. The reported photodetector has high photoresponse and faster response time. Its other virtues include biocompatibility and low cost. One potential limitation of this device is the possibility of existence of the potential release of gas species from the electrochemical reactions occurring at either interface, especially depending on the operating voltage used, which controls the nature of reduction and oxidation reactions at the two electrodes. One can of course envision mesoporous or nanohole patterned electrodes at either ends which can allow release of gases or even replenishment of the lost fluid. Also, some optoelectronic materials (e.g. ZnO used in this work) may have piezotronic properties which may be of significance to the hybrid device function,

especially at low illumination.[37] ZnO being a piezoelectric material it is useful to comment on the possible contribution of piezoelectronic effects in the device function. In this context Wang and co-workers have shown that this can be an important effect especially at low levels of incident optical power.[38,39] Thus in the device discussed here we do expect the contribution of this effect, but not a very significant one at the levels of the intensity of light for which we have examined our materials. Nonetheless in order to

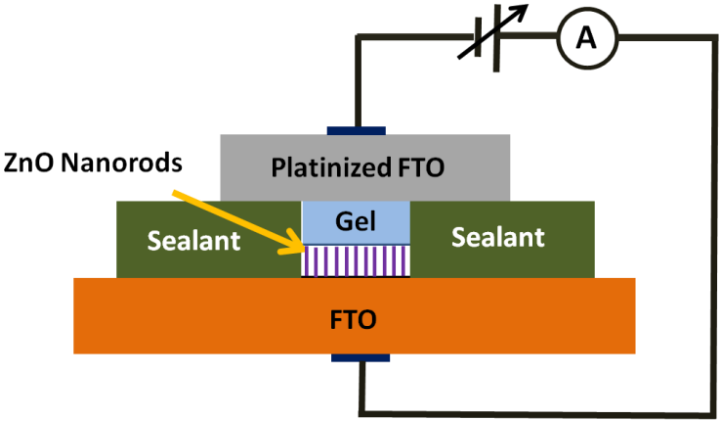

Figure 3.19: *The schematic diagram of proposed practical design of a ZnO nanorod-gel photodetector.*

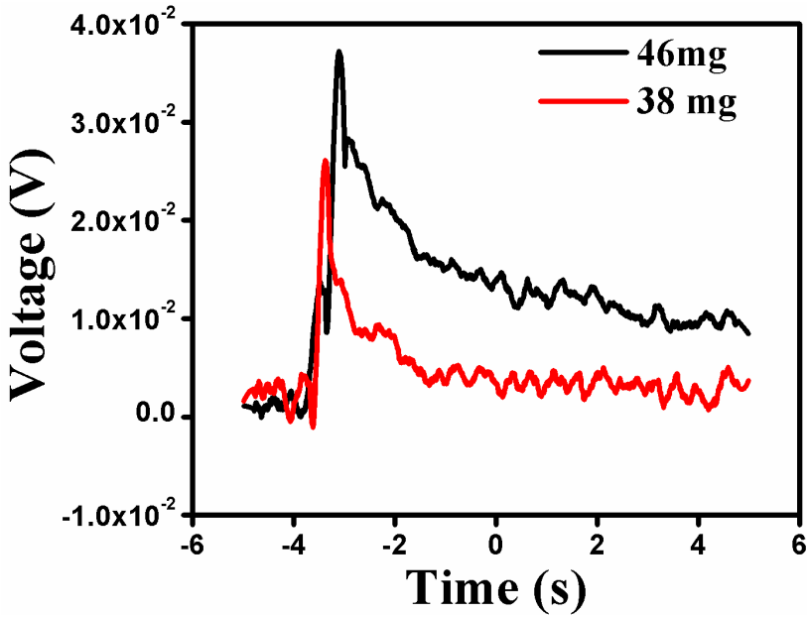

Figure 3.20: *The piezovoltage generated in ZnO nanorods by Agarose gel drop of different weight.*

find out the significance of this effect we looked at the generation of a voltage on a Pt contacted ZnO nanorod array film due to addition of a small amount of gel. As **Figure 3.20** shows, the effect is indeed present as it increases with the weight of gel dispensed on the surface. Clearly at low levels of illumination this could be important to consider. These design details are out of scope of this first academic study, but the outlook for a practical design seems to be quite optimistic.

3.5 Conclusions

We have shown that an interface between a quasi-liquid ionic conductor and light harvesting configuration of quasi-1D functional metal oxide (ionic-electronic hybrid) yields a highly efficient photodetector that shows strong photoresponse in the UV as well as partial visible range. The electric field induced band bending at the interface and the light harvesting nature of nanorods configuration are together shown to help realize three orders of magnitude higher photocurrent in this device as compared to the case of bare ZnO-nanorods-Pt system. Impedance spectroscopy is used to bring out a significant decrease in the charge transfer resistance and the capacitance of this interface controlled device upon illumination. We have further shown that the gel layer remarkably improves the response time and IPCE of ZnO-gel-Pt system in comparison to bare ZnO-Pt system.

3.6 References

1. a) Ü. Özgür, Ya. I. Alivov, C. Liu, A. Teke, M. A. Reshchikov, S. Doğan, V. Avrutin, S.-J. Cho, H. Morkoçd, *J. Appl. Phys.* **2005**, 98, 041301; b) C. Klingshirn, *Chem. Phys. Chem.* **2007**, 8, 782 .
2. a) A. B. Djurisˇic´, Y. H. Leung, *Small* **2006**, 2, 944; b) T. Zhai, X. Fang, M. Liao, X. Xu, H. Zeng, B. Yoshio, D. Golberg, *Sensors* **2009**, 9, 6504.
3. U¨. Ozgu¨r, D. Hofstetter, H. Morkoc, *Proceedings of the IEEE* **2010**, 98.
4. C. S. Lao, M. C. Park, Q. Kuang, Y. Deng, A. K. Sood, D. L. Polla, Z. L. Wang, *J. Am. Chem. Soc.* **2007**, 129, 12096.

5. Y. Hu, J. Zhou , P.-H. Yeh, Z. Li , T.-Y. Wei, Z. L. Wang, *Adv. Mater.* **2010**, 22, 3327.
6. H.-J. Koo, S. T. Chang, O. D. Velev, *Small* **2010**, 6, 1393.
7. O. J. Cayre, S.T. Chang, O. D. Velev, *J. Am. Chem. Soc.* **2007**, 129, 10801.
8. H.-J. Koo, J.-H. So , M. D. Dickey, O. D. Velev, *Adv. Mater.* **2011**, 23, 3559.
9. H.-J. Koo, S. T. Chang, J. M. Slocik, R. R. Naik, O. D. Velev, *J. Mater. Chem.* **2011**, 21, 72.
10. J.-H. Han, K. B. Kim, H. C. Kim, T. D. Chung, *Angew. Chem.* **2009**, 121, 3888.
11. K. Tybrandt, E. O. Gabrielsson, M. Berggren, *J. Am. Chem. Soc.* **2011**, 133, 10141.
12. A. Yengantiwar, R. Sharma, O. Game, A. Banpurkar, *Curr. Appl. Phys.* **2011**, 11,113.
13. a) D.C. Kim, B. O. Jung, Y. H. Kwon, H. K. Cho, *J. Electrochem. Soc.* **2012**, 159, 10; b) S. Bai , W. Wu , Y. Qin, N. Cui, D. J. Bayerl, X. Wang, *Adv. Funct. Mater.* **2011**, 21, 4464.
14. V. Gautam, M. Bag, K. S. Narayan, *J. Phys. Chem. Lett.* **2010**, 1, 3277.
15. A. Goossens, J. Schoonman, *J. Electroanal. Chem.* **1990**, 289, 11.
16. N. Bonanos, B. C. H. Steele, E. P. Butler, in Impedance Spectroscopy Theory, Experiment, and Applications (Eds: E. Barsoukov, J. R. Macdonald) *Wiley-VCH*, Hoboken, New Jersey, **2005**, Ch. 4.
17. a) M. Deo, S. Mujawar, O. Game, A. Yengantiwar, A. Banpurkar, S. Kulkarni, J. Jog, S. Ogale, *Nanoscale* **2011**, 3, 4706; b) C. He, Z. Zheng, H. Tang, L. Zhao, F. Lu, *J. Phys. Chem. C*, **2009**, 113, 10323.
18. A. A. Smith, T. R. Kuykendall, Y. Zhao, J. Z. Zhang, *Adv. Funct. Mater*. **2009**, 19, 1849.
19. I. Mora-Seró, F. F.-Santiago, B. Denier, J. Bisquert, R. T.-Zaera, *Appl. Phys. Lett*. **2006**, 89, 203117.
20. X. Yang, A. Wolcott, G. Wang, A. Sobo, R. C. Fitzmorris, F. Qian, J. Z. Zhang Y. Li, *Nano Lett.* **2009**, 9, 2331.
21. I. Mora-Seró, F. F.-Santiago, B. Denier, J. Bisquert, R. T.-Zaera, *Appl. Phys. Lett.* **2006**, 89, 203117.

22. X. Yang, A. Wolcott, G. Wang, A. Sobo, R. C. Fitzmorris, F. Qian, J. Z. Zhang Y. Li, *Nano Lett.* **2009**, 9, 2331.
23. Y.-Y. Lin, C.-W. Chen, W.-C. Yen, W.-F. Su, C.-H. Ku, J.-J. Wu, *Appl. Phys. Lett.* **2008**, 92, 233301.
24. C. Soci, A. Zhang, B. Xiang, S. A. Dayeh, D. P. R. Aplin, J. Park, X. Y. Bao, Y. H. Lo, D. Wang, *Nano Lett.* **2007**, 7, 1003.
25. R. M. Sheetz, I. Ponomareva, E. Richter, A. N. Andriotis, M. Menon, **Phy. Rev. B. 2009**, 80, 195314.
26. H. K. Raut, V. Ganesh, A. S. Nair, S. Ramakrishna, *Energy Environ. Sci.* **2011**, 4, 3779.
27. A. W. Bott, *Current Separations*, **1998**, 17, 3.
28. M. Ghosh, A. K. Raychaudhuri, *Appl. Phys. Lett.* **2011**, 98, 153109.
29. S. M. Sze, K. K. Ng, in Physics of semiconductor Devices ,3 edition, *Wiley-VCH*, Hoboken, New Jersey, **2007**, Ch. 13.
30. R. R. Prabhakar, N. Mathews, K. B. Jinesh, K. R. G. Karthik, S. S.Pramana, B. Varghese, C. H. Sow, S. Mhaisalkar *J. Mater. Chem.* **2012**, 22, 9678.
31. http://rredc.nrel.gov/solar/spectra/am1.5/.
32. Y. Hu , J. Zhou , P.-H. Yeh , Z. Li , T.-Y. Wei, Z. L. Wang, *Adv. Mater.* **2010**, 22, 3327.
33. S. Bai , W. Wu , Y. Qin , N. Cui , D. J. Bayer, X. Wang, *Adv. Funct. Mater.* **2011**, 21, 4464.
34. J. B. K. Law, J. T. L. Thong, *Appl. Phys. Lett.* **2006**, 88, 133114.
35. C.-Y. Kao, C.-L. Hsin, C.-W. Huang, S.-Y. Yu, C.-W. Wang, P.-H. Yeh, W.-W. Wu, *Nanoscale,* 2012, DOI: 10.1039/c1nr10742a
36. J. Zhou, Y. Gu, Y. Hu, W. Mai, P. Hung, *Appl. Phys. Lett.* **2009**, 94, 191103.
37. Q. Yang , X. Guo , W. H. Wang , Y. Zhang , S. Xu , D. H. Lien ,Z. L. Wang , *ACS Nano* **2010** , 4 , 6285 .
38. Y. Liu , Q. Yang , Y. Zhang , Z. Yang , Z. L. Wang *Adv. Mater.* **2012**,24,1410.
39. Q. Yang , X. Guo , W. H. Wang , Y. Zhang , S. Xu , D. H. Lien ,Z. L. Wang , *ACS Nano* **2010** , 4 , 6285 .

CHAPTER 4

A Self-Powered UV-Vis Photo-detector based on $ZnIn_2S_4$ / Hydrogel Interface

In this chapter the photo-sensing properties of vertically aligned $ZnIn_2S_4$ nanopetal films grown hydrothermally on FTO coated glass are examined without and with surface dispensed agarose gel. For the $ZnIn_2S_4$ nanopetals photodetector (without gel) there is no photoresponse for zero bias. Most interestingly, with surface dispensation of agarose gel, the hybrid electronic-iontronic interface system shows a strong photoresponse even under zero bias; a highly efficient self-powered UV-visible light photodetector. Indeed, the zero bias $ZnIn_2S_4$/gel hybrid photoresponse is a factor of 100 stronger as compared to the response of the only $ZnIn_2S_4$ device (at -1.5 V bias) and that too without any significant degradation in response time. The possible operating mechanisms are proposed.

4.1 Introduction

Metal chalchogenides have attracted considerable attention of the optoelectronics community lately due to their interesting semiconducting and optical properties. Indeed there is a significant current interest in sulphide based photodetectors.[1-3] Zinc Indium Sulphide ($ZnIn_2S_4$) is one such ternary chalcogenide with layered structure and has applications in the fields of charge storage, photocatalysis and photovoltaics.[4-7] The optical absorption of $ZnIn_2S_4$ corresponds well to the solar spectrum, rendering it a material of growing interest in the context of solar optoelectronics. Various nanostructures of $ZnIn_2S_4$ such as nanotubes, nanorods, and microspheres have been fabricated to tune the physical and chemical properties to the desired specifications.[4-9] To the best of our knowledge however no $ZnIn_2S_4$-based photodetector is reported thus far.

There are two polymorphs of $ZnIn_2S_4$ namely cubic and hexagonal[8,9] and it would be interesting to explore both of them. However since the morphologies need to be similar for proper comparison this will form a part of our ongoing efforts. Hence here we focus on the hexagonal form which we could synthesize in the desired 2D morphological form. The 2D nanostructures are especially important because of high surface area and efficient charge transport. In many cases substrate-supported 2D $ZnIn_2S_4$ nanostructures can be easily grown, but their incorporation into robust device systems is not-trivial due to issues related to the nature and degree of surface coverage of subsequent layers that can be realized for the creation of functional heterostructure configurations. An interesting approach to make a shape-conforming contact to an orientationally disordered nanostructure is by using a functional liquid or gel, which is transparent and conducting. Ionic liquids or gels represent good candidates in this respect.

Another objective was to explore the possibility of realizing self-powered photodetector in view of the charge separation (photovoltaic effect) character of the interfaces formed. Indeed, recently there is a surge of interest in self-powered nanodevices, especially photodetectors. Several structures are possible to observe photovoltaic effect: p-n junctions, heterojunctions, Schottky barriers and Metal insulator-

semiconductor (MIS) photocapacitors. Various self powered Schottky,[10] p-n junction[11,12] or photo electrochemical cell (PECC) type[13,14] photodetectors have thus been reported.

Recently, there is a growing interest towards developing ion-based devices such as rectifiers, logic gates, memresistors, transistors etc. which mimic the biological system in their mode of operation; notably the signal transport in neurons occurs via ionic transport.[15-19] Agarose-based hydrogel has attracted a lot of interest towards developing such iontronic devices, since it has good ionic conductivity (H^+ and OH^- ions). We recently demonstrated an electronic/ionic hybrid photo-detector comprised of ZnO nanorods and agarose gel, which showed a remarkable three order of magnitude strong and fast UV photoresponse as compared to that of only ZnO nanorods.[20] In this work our intent was to apply the concept of gel induced manipulation of interface phenomena to $ZnIn_2S_4$ based photosensing to realize a strong and fast response over the UV-visible regime.

In this work vertically-aligned dense $ZnIn_2S_4$ Nanopetal films were grown on FTO glass by hydrothermal method and evaluated for their photo-response in different interesting device configurations. The petals in the film are well-separated from each other and the separation between two successive petals is in the range of 200-1000 nm. This indicates that the film surface is highly accessible for an interface-based device configuration. Large surface to volume ratio and low dimensionality are known to yield higher light sensitivity and increase the photo-carrier lifetime as more charge separation take place due to surface states.

Here, we demonstrate that the UV-Vis photoresponse of vertically aligned $ZnIn_2S_4$ film is enhanced by three orders of magnitude by modifying its surface with a hydrogel. The performance of such a hybrid device is compared to that of $ZnIn_2S_4$ based photodetector without gel. Such huge enhancement in photoresponse and zero bias (self-powered) operation is attributed to unique features of the interface between the gel and the nanostructured $ZnIn_2S_4$ film.

4.2 Experimental Section

To obtain uniform film of $ZnIn_2S_4$ on the FTO substrate, first we cleaned the FTO and dried at 450 ^oC for 2h. Zinc acetate, indium nitrate and thiourea were used as precursors of Zn, In and S, respectively. 1 mmol of zinc acetate, 2 mmol indium nitrate and double excess (8 mmol) thiourea were dissolved in de-ionized (DI) water. This mixture was stirred for 30 minutes and transferred to a teflon-lined reactor. Cleaned FTO-coated glass substrates were hung in the reactor with the help of a teflon tape. The autoclave was then sealed and maintained at 150 ^oC for 16 h, followed by natural cooling to room temperature. A yellow film was seen to grow on the FTO substrate which was further washed with DI water and finally with ethanol. This film was dried under IR for further characterizations.

All the samples were characterized by X-ray diffraction (Philips X'pert Pro), scanning electron microscopy (SEM), diffuse reflectance spectroscopy (DRS) recorded with an integrated sphere, electrochemical impedance spectroscopy (EIS, Auto lab PGSTAT 30), and quantum efficiency using Newport IPCE measurement setup. The current voltage (I-V) measurements were done using Keithley 2400 SMU. Photo-conductance was measured using LEDs of different wavelengths and solar simulator model Newport AM 1.5 1 Sun. All the electrical measurements were done inside a dark room under ambient conditions.

4.3 Device Schematic and Experimental Setup

Figure 4.1 a and **4.1 b** show the schematic of FTO-$ZnIn_2S_4$-Pt electronic device and FTO-$ZnIn_2S_4$-Agarose gel-Pt electronic-ionic hybrid device, respectively. In both these devices FTO-coated glass serves as the bottom electrode and Pt tip acts as the top electrode. In the hybrid device the $ZnIn_2S_4$ nanopetal film was covered with a layer of agarose solution and cooled to room temperature for gellation. For all the current-voltage (I-V) measurement the FTO contact was grounded and potential was applied through the Pt tip.

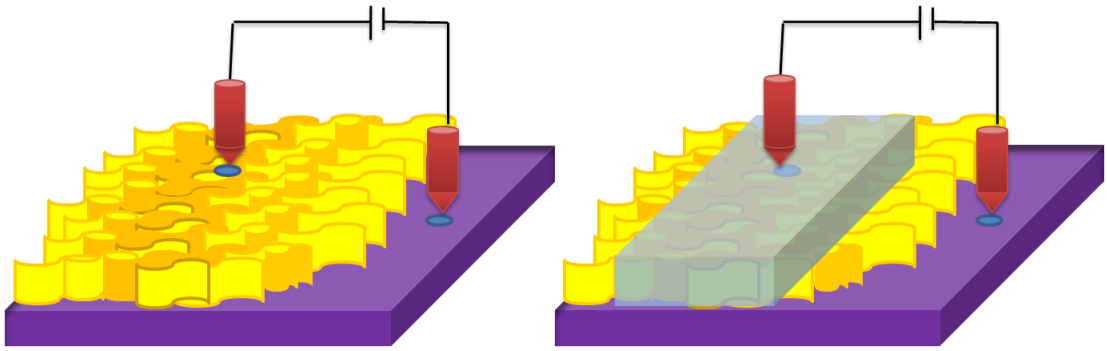

Figure 4.1: *Device architecture of FTO-$ZnIn_2S_4$-Pt and FTO- $ZnIn_2S_4$-agarose gel-Pt respectively.*

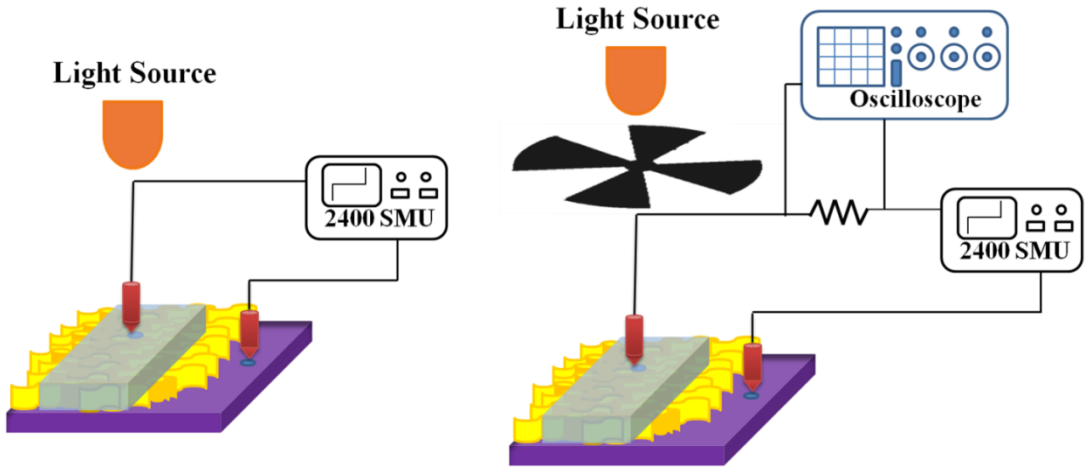

Figure 4.2: *Experimental set up to measure I-V and dynamic photoresponse.*

Figure 4.2 shows the experimental setup to measure the I-V and dynamic photoresponse of the photodetector. To measure the response time of the photodetector more precisely it was connected in series to a 1 MΩ resistor and oscilloscope. The photodetector was placed below the light source with chopper. Then the photo-voltage drop across the resistor was measured as function of time.

4.4 Characterization

Figure 4.3 a depicts the comparison between the X-ray diffraction patterns of FTO coated glass and $ZnIn_2S_4$ (ZIS) on FTO coated glass. It is clearly seen from **Figure 4.3 a** that hexagonal $ZnIn_2S_4$ is successfully grown on the top of conducting FTO glass. This result is in good agreement with the reported JCPDS data (ICDD-JCPDS card No. 72-0773). The UV-Visible diffuse reflectance spectrum (DRS) is shown in **Figure 4.3 b.** It shows a fairly sharp absorption edge indicating homogeneous and stoichiometric ZIS film formation. Strong absorption in the visible region at 515 nm implies that this material is favorable for visible light photocatalysis and photodetectors applications. The morphology of the ZIS film deposited on the FTO substrate observed by FE-SEM is shown in **Figures 4.3 c, d**.

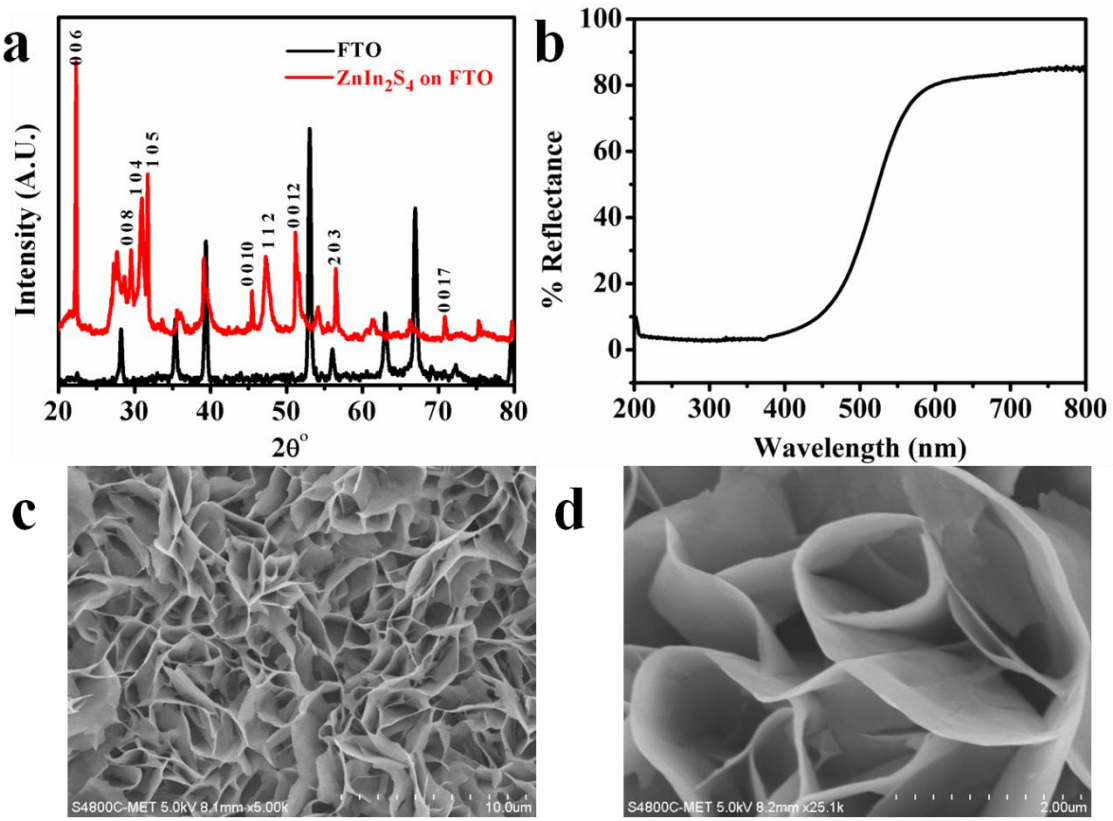

Figure 4.3: a. *XRD* ***b.*** *DRS* ***c.,d.*** *FE-SEM of* $ZnIn_2S_4$ *vertically aligned sheets on FTO coated glass.*

Uniform growth of vertically aligned petals with large density is clearly seen. The mean thickness of the petal is noted to be ~20 nm. These petals are well spaced from each other and the separation between two successive petals is in the range of 200-1000 nm. This indicates that the film is highly open-structured and this characteristic is useful to access its full surface area.

4.5 Results and Discussion

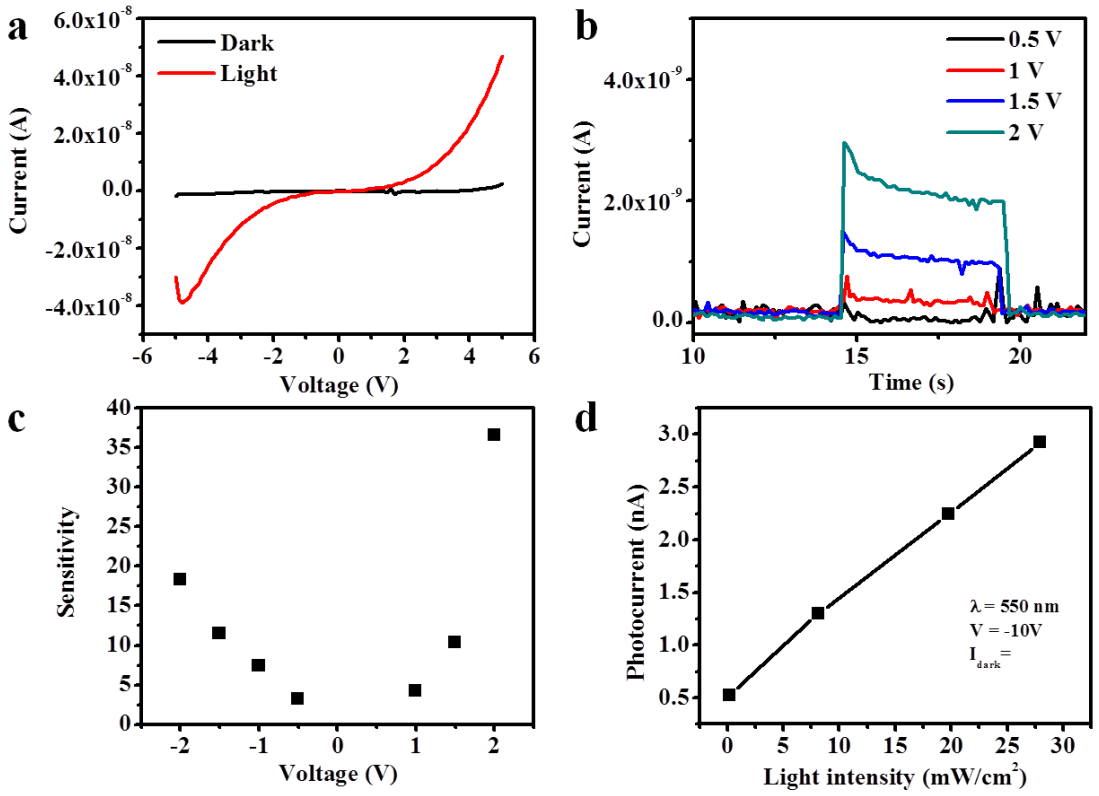

***Figure 4.4: a**. I-V under Dark and illumination **b.** Photo-response as a function of time with light chopping in semi-log plot at different bias voltage **c.** sensitivity as a function of applied bias for FTO-$ZnIn_2S_4$-Pt device **d.** photocurrent as a function of illumination intensity.*

The I-V curves for the FTO-$ZnIn_2S_4$-Pt device under dark and solar AM 1.5 1 Sun illumination are shown in **Figure 4.4 a**. The nonlinearity of the I-V curves in dark

indicates that the contact between the $ZnIn_2S_4$ film and Pt/FTO electrode is a Schottky contact. For the above device the dark current is in the range of 10^{-10} A. Such a low dark current is a requisite to achieve a high sensitivity of a given photodetector.

Figure 4.4 b shows the dynamic photoresponse of the FTO-$ZnIn_2S_4$-Pt system under solar illumination with power density of 100mW/cm^2 at different bias voltages. The dynamic photoresponse was measured by chopping the light source for 5s manually and measuring the current as function of time using Keithley 2400 SMU. The generated photocurrent increases with increasing bias voltage indicating that more number of photogenerated carriers gets converted to photocurrent with higher bias voltage. The photocurrent increases due to the reduction of the carrier transit time resulting in efficient separation of charge carrier, or reduced recombination by the applied bias. When the illumination is on, the current in the FTO-$ZnIn_2S_4$-Pt system increases rapidly, whereas when the illumination is off the current first decreases rapidly and then slowly reaches saturation. The sensitivity of the device defined as the ratio of photocurrent to dark current is also plotted as function of bias voltage and shown in **Figure 4.4 c**. The corresponding value increases with increase in the bias voltage. **Figure 4.4 d** shows the photocurrent as function of light intensity. A Green LED of wavelength 550 ± 20 nm was used as light source; the photocurrent is seen to increase linearly with increasing light intensity.

The rise time, defined as the time taken by the photodetector to reach 90% of maximum photocurrent from its dark current value, and the reset (recovery) time which is the time taken to reach 1/e times the maximum photoresponse current. To measure the response time of the photodetector more precisely it was connected in series to a 1 MΩ resistor and oscilloscope. The photodetector was placed below the light source with chopper. Then the photo-voltage drop across the resistor was measured as function of time. The $ZnIn_2S_4$ device shows the rise time and reset times of only 2 ms see **Figure 4.5**. Such fast photoresponse can be attributed to efficient generation/separation and recombination of the photocarriers.

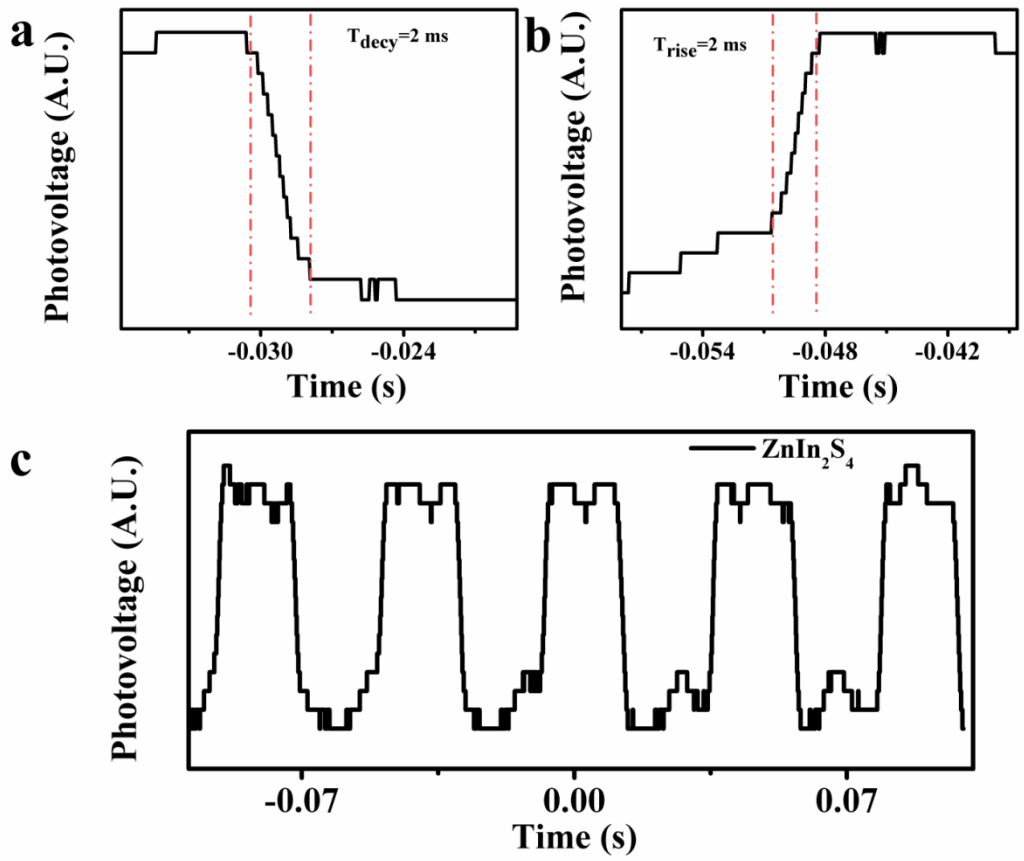

Figure 4.5: ***a****. rise time,* ***b****. reset time,* ***c****. show the full dynamic photoresponse of* $ZnIn_2S_4$ *detector without gel as measured with an oscilloscope.*

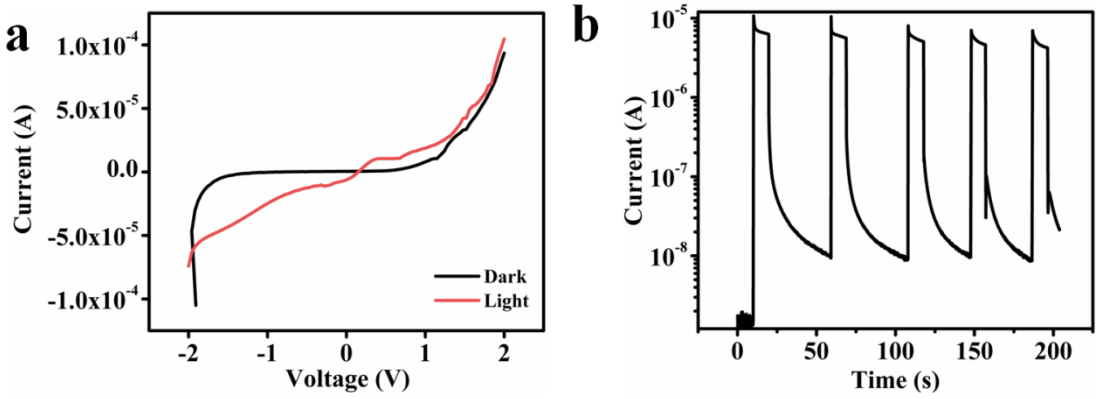

Figure 4.6: ***a****. I-V under Dark and illumination* ***b.*** *Photo-response as a function of time with light chopping in semi-log plot at 0 bias.*

Figure 4.6 a shows the current voltage (I-V) characteristics of the ZIS-agarose gel hybrid device in dark and under solar simulator AM 1.5 1Sun (100 mW/cm^2) illumination. The addition of agarose gel modifies the interface as shown in **Figure 4.7** in such a manner that the FTO-$ZnIn_2S_4$-agarose gel-Pt hybrid system is more rectifying as compared to the FTO- $ZnIn_2S_4$-Pt device. The $ZnIn_2S_4$/gel case shows a rectification ratio of 48 at ±1 V and there is an increase in the dark current as compared to the $ZnIn_2S_4$ device without gel. The striking feature of the $ZnIn_2S_4$/gel system is the photovoltaic effect i.e. the system has an open circuit voltage of 0.63 V with current density of 7 μA/cm^2 under solar illumination. This open circuit voltage is due to the specific nature of the $ZnIn_2S_4$/gel interface. This voltage allows rapid and efficient separation of charge carrier and prohibits recombination even at zero applied bias. Thus, the FTO-$ZnIn_2S_4$-agarose gel-Pt hybrid device is a self-powered hybrid photodetector.

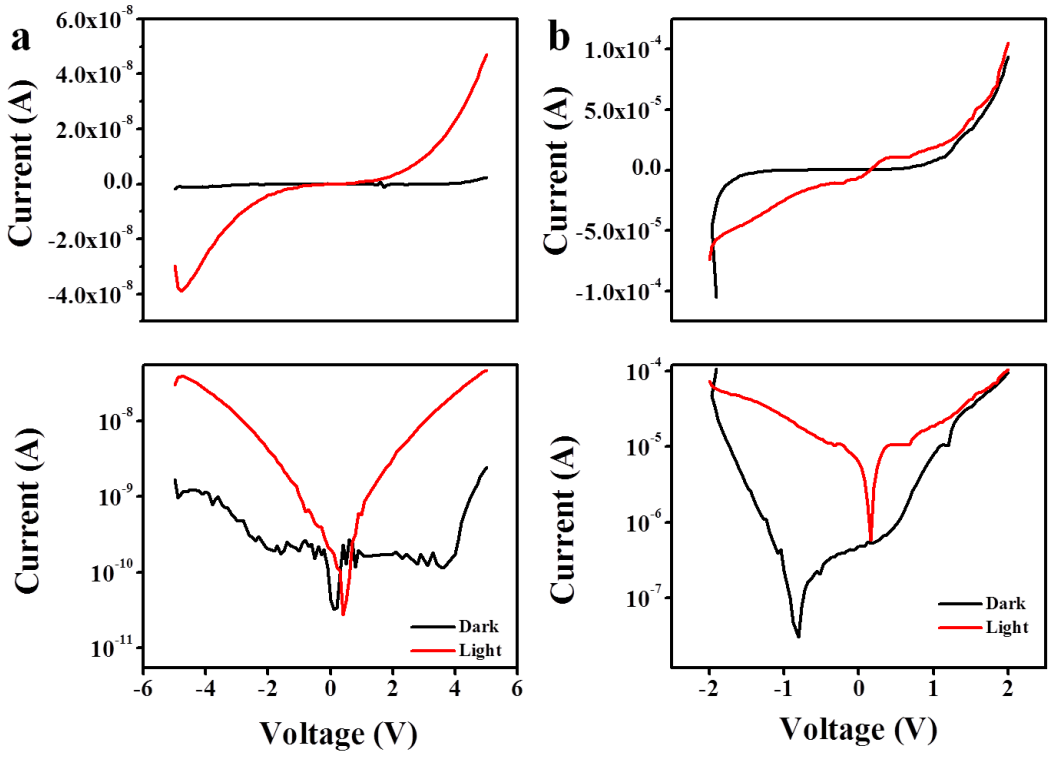

***Figure 4.7: a**. The I-V curves for the FTO-$ZnIn_2S_4$-Pt device in linear and semi-log scales; and **b**. The I-V curves for the FTO-$ZnIn_2S_4$-gel-Pt device in linear and semi-log scales.*

In the hybrid device it can be seen that in sweeping the bias voltage from -2 V to +2 V in the dark, the current minimum occurs at around -1 V, whereas under illumination it shifts towards positive bias (shown in a semi-log I-V plot in **Figure 4.7**). This can be attributed to the characteristic electronic-ionic nature of the interface. In the $ZnIn_2S_4$ film in contact with an electrolyte, space charge region develops within $ZnIn_2S_4$, Helmholtz EDL develops at the interface with the gel and a diffuse charge layer (Stern layer) develops in the gel due to electron-ion imbalance.[21] The interface is a combination of space charge capacitance, Helmholtz capacitance and the Stern capacitance. When this interface is illuminated, high density of electrons and holes is generated which changes the interface charge distribution, thereby dramatically reducing the capacitances of the interface regions and shifting the current minimum significantly towards positive bias. This is further confirmed by impedance spectroscopy.

Figure 4.6 b shows the dynamic performance of the $ZnIn_2S_4$/gel hybrid device under AM 1.5 1 Sun illumination for zero bias condition. The device shows a remarkably strong photoresponse (I_{light}/I_{dark}) of 3 orders of magnitude (a factor of 1000) and thus works as a highly efficient self-powered photodetector. In the FTO-$ZnIn_2S_4$-Pt device without gel the highest photocurrent value was only in the region of 10^{-9} A, which is very low and does not meet the requirements of practical application.

When the light is on the current increases rapidly reaching a maximum and then decreasing gradually to reach a stable value. The decrease in current after reaching the maximum is due to the recombination of the photogenerated charge carriers. In the hybrid ($ZnIn_2S_4$ / gel) device there is diffusion and drift of charge carriers on the gel and $ZnIn_2S_4$ sides, respectively, and diffusion being a slow process the accumulation of charge carriers can occur near the interface causing higher rate of recombination under constant illumination, especially under zero bias. When the light is off, the current initially decreases rapidly and then gradually reaches saturation. The rise time for hybrid device is about 25 ms. Decay response time constant of the device is 120 ms as shown in **Figure 4.8**. The initial fast response is attributed to the photo-excited carrier generation, and the

slow response at the second stage is mainly ascribed to photo desorption of the chemisorbed oxygen ions and water molecules from the surface of the $ZnIn_2S_4$.

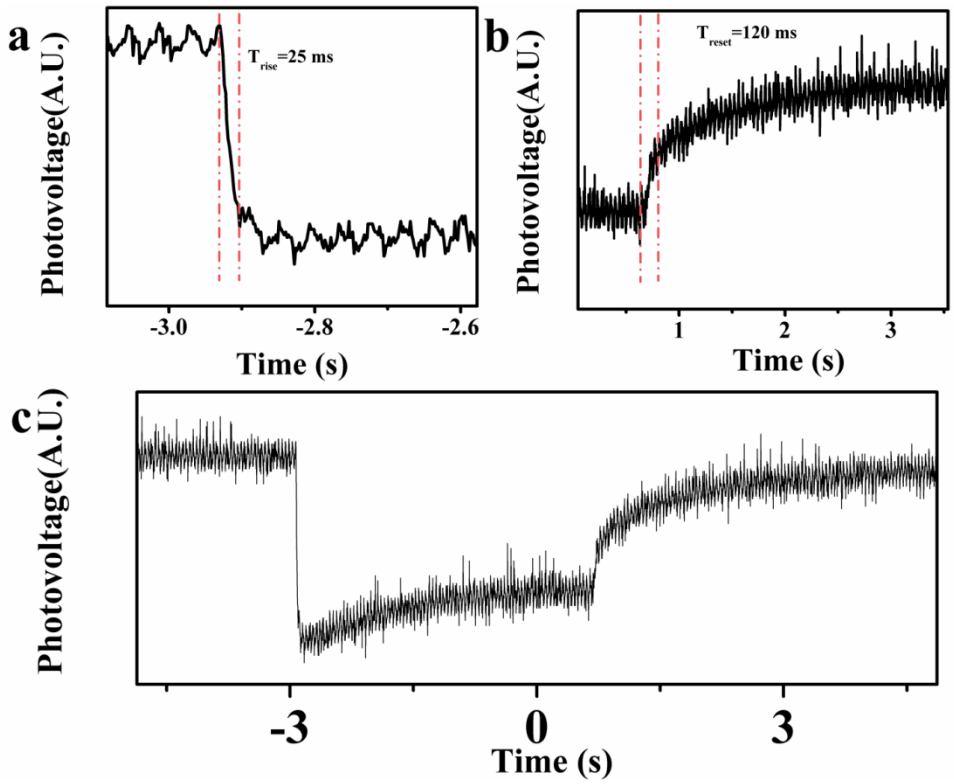

Figure 4.8: *Estimation of the* ***a****. rise and* ***b****. reset times* ***c****. the full dynamic photoresponse of FTO- $ZnIn_2S_4$-gel-Pt device.*

The response time of the hybrid device is understandably slower as compared to the $ZnIn_2S_4$ device without gel. The $ZnIn_2S_4$ device without gel is a pure electronic device as against the $ZnIn_2S_4$-gel device which is a Hybrid device working at zero bias. In the hybrid device the transport of charges through the gel occurs by diffusion, which is a slower process than pure electronic transport, hence the response is somewhat slower.

To gain a better understanding of the electronic–ionic interface of the hybrid devices the electrochemical impedance spectroscopy (EIS) was performed in the dark and under AM1.5 1 Sun illumination in the frequency range of 10 mHz to 10^6 Hz at an ac voltage of 10 mV. The impedance was recorded in a two-electrode set up. **Figure 4.9 a** shows the Nyquist plot for the $ZnIn_2S_4$ gel system. The enhanced performance of the

hybrid device can be noted from the difference in the impedance spectra in dark and under illumination. In the dark, the impedance plot shows a roughly straight (slightly bowing) line over the entire frequency regime. Under illumination the impedance plot shows one semicircle. The obtained data was fitted into an equivalent circuit and the fitted values are given in **Table 1**. R_S represents the contact resistance between FTO/$ZnIn_2S_4$ and gel / Pt, and it remains nearly constant under dark and illumination. R_{P1} represents the charge transfer resistance, and its value is drastically reduced+ from 2.54 MΩ in dark to 61.3 kΩ under illumination.

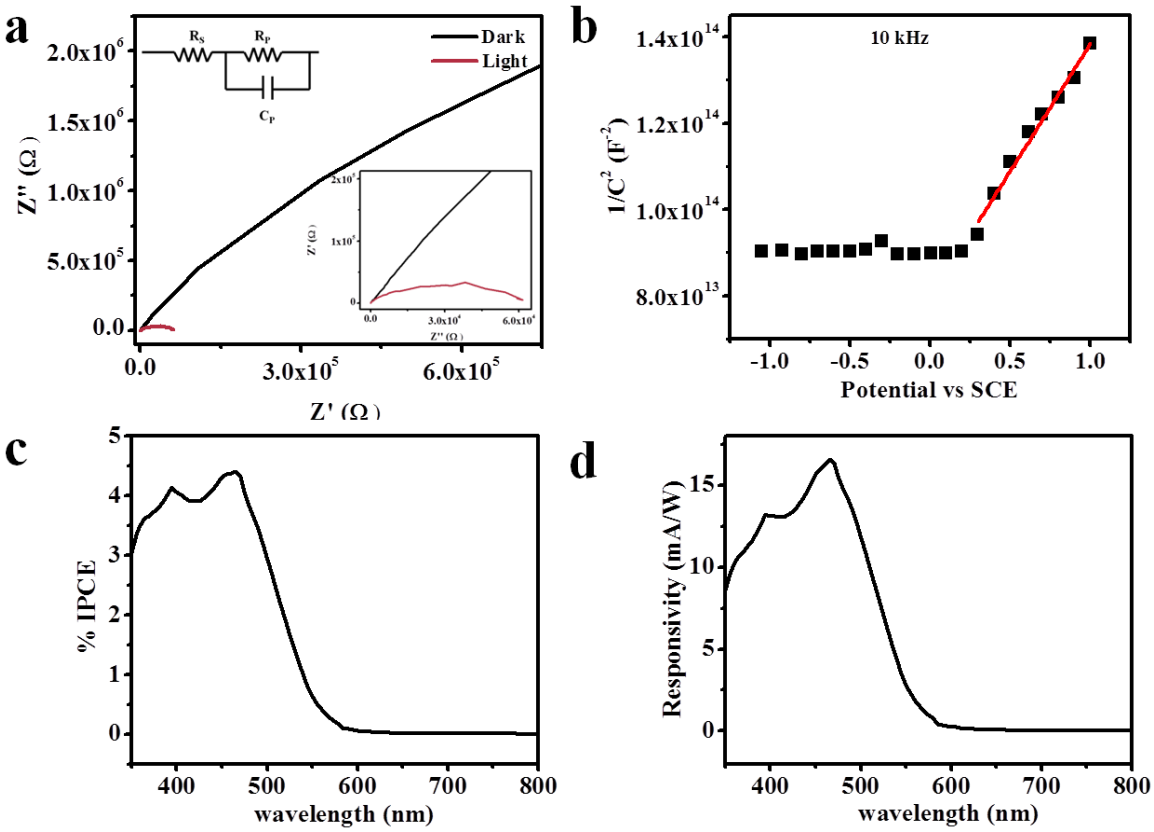

Figure 4.9: a*. Impedance plot inset shows magnified response at high frequency and fitted equivalent circuit.* ***b****. Mott-Schottky Plot of* $ZnIn_2S_4$ *agarose gel* ***c****. IPCE of FTO-*$ZnIn_2S_4$*- agarose gel- Pt under dark and illumination* ***d****. Responsivity as function of wavelength* $ZnIn_2S_4$ *agarose gel.*

	R_S [Ω]	R_P[kΩ]	C_P[μF]
Dark	**27.9**	**2540**	**4**
Light	**27.2**	**61.3**	**4.7**

Table 1: *Fitted impedance parameter.*

In Table 1, R_S represents the contact resistance and R_{P1}, represents the charge transfer resistance and Cp capacitance.

The flat band potential, carrier type and carrier density were calculated by recording Mott-Schottky plot for the $ZnIn_2S_4$ / gel based hybrid system.[20] In the Mott Schottky plot $1/C^2$ is plotted against the applied potential. The intercept of the linear portion of $1/C^2$ on the x-axis gives the value of the flat band potential, and the slope of the curve gives the charge carrier density. **Figure 4.9 b** shows the Mott-Schottky plot for the case of $ZnIn_2S_4$ / gel. The positive slope of the Mott Schottky plot shows that the as-grown $ZnIn_2S_4$ is n-type. The charge density can be calculated by,

$$N_d = \left(\frac{2}{e_0 \varepsilon \varepsilon_0}\right)\left[\frac{d\left(\frac{1}{C^2}\right)}{dV}\right]^{-1}$$

Where, ε_0 is permittivity of free space, ε is the dielectric constant of $ZnIn_2S_4$, e_0 is electronic charge, N_d is carrier density, and V_{FB} is the flat band potential. The calculated carrier density of $ZnIn_2S_4$ in the presence of agarose gel is 5.5×10^{16} cm^{-3}. The flat band potential calculated from the intercept is -0.16 V.

The incident photon to current conversion efficiency (IPCE) for the $ZnIn_2S_4$ / gel system in the spectral range of 350-800 nm is shown in **Figure 4.9 c**. To measure the IPCE a $ZnIn_2S_4$ film of area 0.25 cm^2 was first protected on all the sides by a scotch tape, and then the film was covered with a thin layer of agarose gel. Transparent platinized FTO was used as counter electrode. The IPCE shows that the hybrid $ZnIn_2S_4$ / gel system

absorbs mostly in UV and visible up to 600 nm. The IPCE corresponds well with the DRS spectrum for the $ZnIn_2S_4$ film. The IPCE however shows two maxima corresponding to 3.13 eV and 2.61 eV which can be attributed to the complex band structure due to changes in the concentration and types of structural defect in these $ZnIn_2S_4$ films. [22] The IPCE gives the external quantum efficiency (EQE) as a function of wavelength for zero bias.[23]

Figure 4.9 d shows the spectral responsivity of the $ZnIn_2S_4$-gel-Pt photodetector at zero bias. Spectral responsivity is a measure of photocurrent flowing in the detector divided by incident optical power. The responsivity was calculated from EQE taking the photoconductive gain as 1.

$$R_\lambda = \frac{(EQE)}{h\nu}$$

As can be seen, the $ZnIn_2S_4$-gel-Pt hybrid photodetector has a responsivity of 16.5 mA/W at 470 nm even for zero bias. This is due to the efficient separation of charge carrier at the interface by the open circuit voltage. The spectral responsivity of the device is indeed good.

Figure 4.10 a show the band diagram for the FTO-$ZnIn_2S_4$-Pt system. The photoconduction in $ZnIn_2S_4$ occurs due to the generation of electron-hole pairs in the presence of light. The holes get trapped by the acceptor level existing above the valence band of $ZnIn_2S_4$. Trapping of holes creates charged acceptor levels. These charged acceptor levels repel the electron, thereby preventing the recombination. Thus electron can move freely through the material leading to an increase in conductivity in the presence of light.[7]

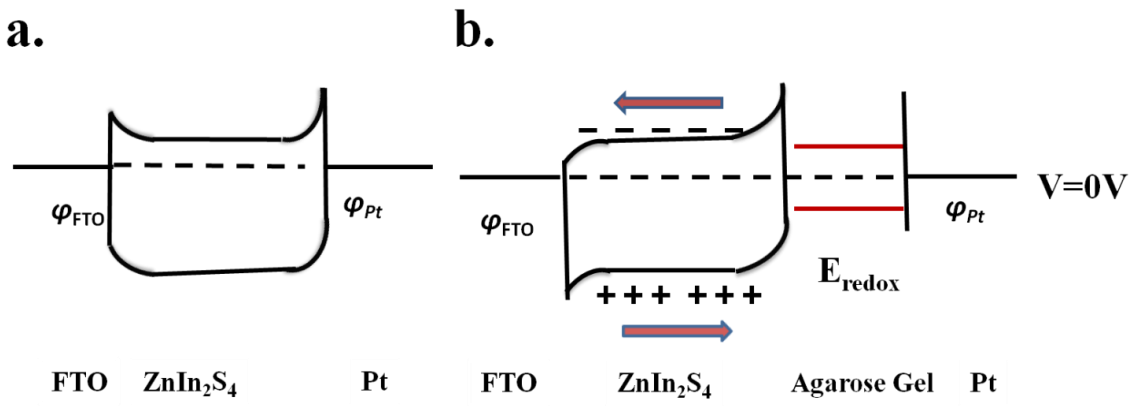

Figure 4.10: *Band diagram:* ***a.*** *$ZnIn_2S_4$ nanopetal device,* ***b.*** *$ZnIn_2S_4$ nanopetal –agarose gel hybrid device at 0 V.*

The $ZnIn_2S_4$ agarose gel device basically acts as Metal insulator-semiconductor (MIS) photo-capacitor. The electronic/ionic nature of the interface of $ZnIn_2S_4$ and agarose gel is expected to be defined by the differences in the Fermi level of $ZnIn_2S_4$ and the redox potential of agarose gel.[24] This leads to band bending in $ZnIn_2S_4$ resulting from the transfer of carriers across the interface; in this case electron transfer from $ZnIn_2S_4$ to the agarose gel and hole transfer in the opposite direction. This would cause a depletion region in $ZnIn_2S_4$, and an electric double layer plus a Stern layer in the gel with accumulation of OH^- at the $ZnIn_2S_4$ surface. Thus, at the interface an in-built potential develops as confirmed by V_{oc} of 0.63 V. This built-in electric field causes the charge carriers of opposite sign to move in opposite directions depending upon the external circuit. When the interface is illuminated by light the electron-hole pairs are generated within the $ZnIn_2S_4$. The electron hole pairs generated at the interface are efficiently separated by the built-in potential due to the depletion region at the interface. The electron gets transferred to the FTO from $ZnIn_2S_4$ and the holes move through the gel.

Photodetector	Type	Photosensitivity	Rise/Fall time	Operating voltage (V)	Responsivity (A/W)	Reference
MoS_2	Phototransistors	-	50ms	-	7.5×10^{-3}	2
GaS Nanosheet	Photoconductor	1.5×10^4	30ms	2	4.2	3
GaSe Nanosheets	Photoconductor	0.38	0.02 s	2	2.8	4
Sb-doped ZnO	Schottky	2200	100 ms	0	-	11
ZnO/GaN	p-n	10^6	20/219 µs	0	-	12
ZnO nanorods/CuSCN	p-n	10^5	500ns/6.7µs	0.1mV	$1x10^{-3}$	13
TiO_2 /SnO_2	PECC	4550	0.03 s/0.01 s	0	0.6	14
TiO2	PECC	2698	0.08s/0.01s	0	-	15
ZnO/Agarose gel	Hybrid	>1000	250/100 ms	2	$1.3x10^{-2}$	7
$ZnIn_2S_4$ without gel	Schottky	>10	2 ms/2ms	1.5 V	-	Present work
$ZnIn_2S_4$/Agarose gel	Hybrid	>1000	25ms/120ms	0	$1.6x10^{-2}$	Present work

Table 2: *Comparison of the Critical Parameters for the Photodetectors.*

Table 2 presents a comparison of critical parameters for various photodetectors reported and the present work. When the performance of only $ZnIn_2S_4$ photodetector (i.e. without gel) is compared to other sulphide (MoS_2, GaS, GaSe) based detectors[2-4] it shows relatively faster response. The $ZnIn_2S_4$ device also shows better photosensitivity as compared to a GaSe photodetector at comparable operating voltage.[4] The $ZnIn_2S_4$-gel photodetector can now be compared to other photodetectors based on the use of p-n junction, Schottky junction, and PECC (Photoelectrochemical cell). The Hybrid device shows a comparable response time and sensitivity to Schottky and PECC type photodetectors at zero bias. However, the response time of p-n photodiode is better than our hybrid photodetector.

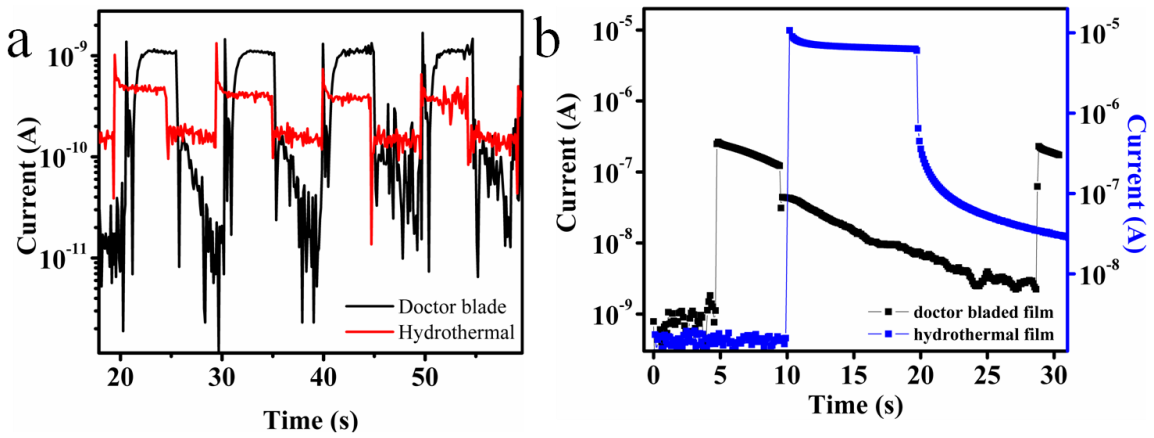

Figure 4.11: a. *comparison of Doctor-bladed thin film performance with hydrothermal nanopetal photodetector performance a* $ZnIn_2S_4$ *only;* ***b.*** $ZnIn_2S_4$*-gel.*

We also evaluated the performance of a doctor-bladed thin film of $ZnIn_2S_4$ with that of the vertically aligned $ZnIn_2S_4$ nanopetal film (**Figure 4.11**) and the corresponding results are discussed. This was done to understand the possible negative consequences of the petal-like morphology and related light shadowing effects. It was found that the performance of the doctor-bladed $ZnIn_2S_4$ thin film *without gel* is seen to be better than that of the vertically aligned nanopetals film *without gel*. However, in the case of gel-based devices, interestingly the performance of the $ZnIn_2S_4$ nanopetal-gel photodetector is found to be better in comparison to the doctor-bladed $ZnIn_2S_4$ thin film-gel photodetector. This can be attributed to nanopetal morphology which enhances the interfacial area between the $ZnIn_2S_4$ and agarose gel. It should be noted that after pouring of gel there is ample opportunity for internal refraction effects within the configuration which can access the so-called shadow regions in the absence of the gel.

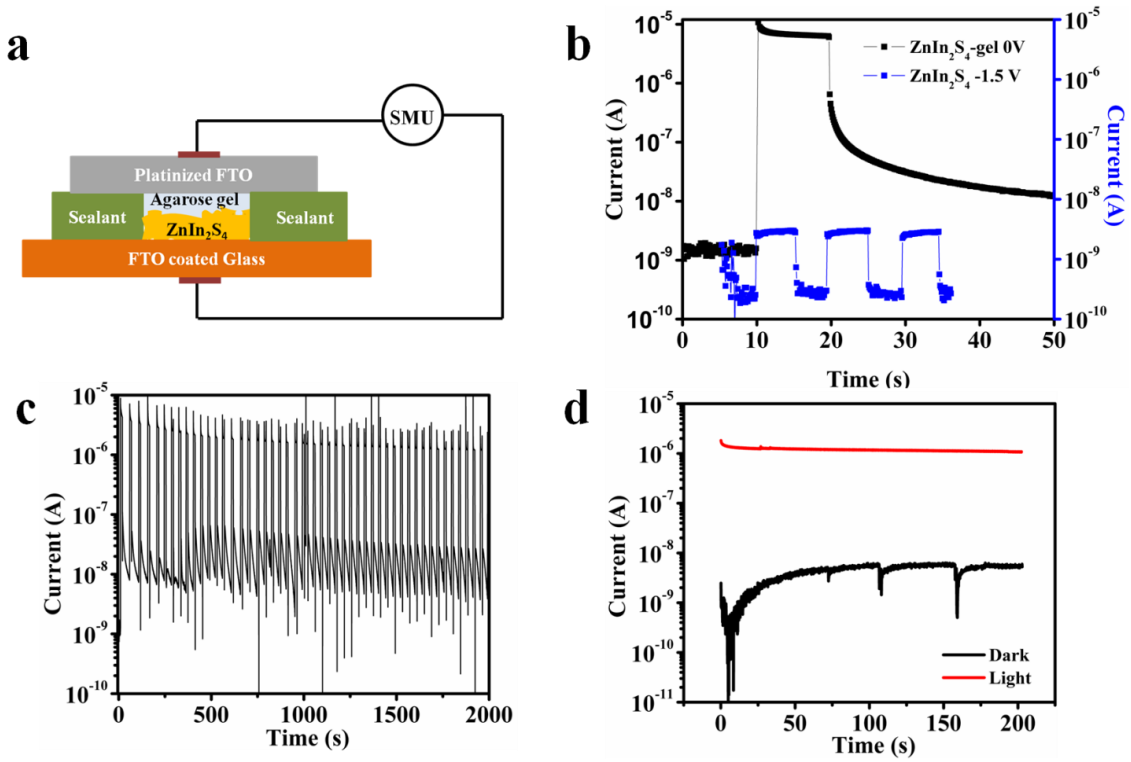

Figure 4.12: a. *schematic of $ZnIn_2S_4$–gel sealed hybrid device* ***b.*** *Comparison of photoresponse of $ZnIn_2S_4$ –gel hybrid device at 0 V with $ZnIn_2S_4$ device at -1.5 V* ***c.*** *and* ***d.*** *shows the stability of the sealed device.*

Figure 4.12 b shows the photoresponse comparison of the FTO-$ZnIn_2S_4$–gel–Pt hybrid device at zero bias and the FTO-$ZnIn_2S_4$–Pt device at -1.5 V bias. The response of the hybrid device even for zero bias is 100 times higher than that of the only $ZnIn_2S_4$ device. To make a robust and realistic device we covered the $ZnIn_2S_4$ nanopetals film of area 0.5 × 0.5 cm^2 on all the sides by a sealant; and then a Platinized-FTO with two drilled holes was applied as a top contact. The device was thus sealed. Finally, agarose gel was dispensed on the surface of the $ZnIn_2S_4$ nanopetals through the holes with the help of vacuum pump. These holes were also sealed using the same sealant. **Figure 4.12 a** shows the schematic of this device and the corresponding photoresponse as a function of time during alternating light on/off in air at zero bias. The device shows a stable performance as confirmed by **Figure 4.12 c** and **d. Figure 4.12 c** shows the light chopping data for 50 cycles.

4.6 Conclusions

We have demonstrated fabrication of a highly efficient self-powered UV-Vis photo-detector based on $ZnIn_2S_4$ nanopetal film with surface-dispensed agarose gel. The $ZnIn_2S_4$ nanopetals films are grown on FTO-coated glass hydrothermally. The photoresponse of the $ZnIn_2S_4$/gel hybrid device is seen to be higher by a factor of ~100 even for zero bias as compared to the photodetector without gel powered at -1.5 V. The response times (rise and fall) for the $ZnIn_2S_4$ only (i.e. without gel) photodetector is 2 ms (for both) whereas the response time for the $ZnIn_2S_4$-gel hybrid device is 25 ms and 120 ms, respectively. Impedance spectroscopy shows a drastic change in the charge transfer resistance and capacitance in the hybrid device under illumination. The hybrid photodetector shows good responsivity of 16.5 mA/W even at zero bias.

4.7 References

1. Z. Yin, H. Li, H. Li., L. Jiang, Y. Shi, Y. Sun, G. Lu, Q. Zhang, X. Chen, H. Zhang, *ACS Nano*, **2012**, 6,74.
2. P. A. Hu, L. Wang, M. Yoon, J. Zhang, W. Feng, X. Wang, Z. Wen, J. C. Idrobo, Y. Miyamoto, D. B. Geohegan, K. Xiao, *Nano Lett.* **2013**, 13, 1649.
3. P.A. Hu, Z. Wen, L. Wang, P. Tan, and K. Xiao, *ACS Nano* **2012**, 6, 5988.
4. S. Peng, P. Zhu, V. Thavasi, S. G. Mhaisalkar, and S. Ramakrishna, *Nanoscale*, **2011**, 3, 2602.
5. S.Peng, P. Zhu, S. G. Mhaisalkar, and S. Ramakrishna, S. *J. Phys. Chem. C* **2012**, 116, 13849.
6. N. S. Chaudhari, A. P. Bhirud, R. S. Sonawane, L. K. Nikam, S. S. Warule, V. H. Rane and B. B. Kale, B. B. *Green Chem.*, **2011**, 13, 2500.
7. N. Romeo, A. Dallaturca, R. Braglia, and G. Sberveglieri, G. *Appl. Phys. Lett.* **1973**, 22, 21.
8. Y. Chen, R. Huang, D. Chen, Y. Wang, W. Liu, X. Li, Z. Li, *ACS Appl. Mater. Interfaces* **2012**, 4, 2273.

9. Y. Chen, S. Hu, W. Liu, W. Chen, L. Wu, X. Wang, P. Liua, Z. Li, *Dalton Trans.* **2011**, 40, 2607.
10. Y. Yang, W. Guo, J. Qi, J. Zhao, and Y. Zhang, *Appl. Phys. Lett.* **2010**, 97, 223113.
11. Y.-Q. Bie, Z.-M. Liao, H.-Z. Zhang, G.-R. Li, Y. Ye, Y.-B. Zhou, J. Xu, Z.-X. Qin, L. Dai and D.-P. Yu, *Adv. Mater.* **2011**, 23, 649..
12. S. M. Hatch, J. Briscoe, and S. Dunn, *Adv. Mater*. **2013**, 25, 867.
13. X. Li , C. Gao , H. Duan , B. Lu , Y. Wang , L. Chen ,Z. Zhang , X. Pan , E. Xie, *Small*, **2013**, 9, 2005.
14. X. Lia, C. Gaoa, H. Duanb, B. Lua, X. Pana, E. Xie, *Nano Energy* **2012** 1, 640
15. H.-J. Koo, S. T. Chang, O. D. Velev, *Small* **2010**, 6, 1393.
16. O. J. Cayre, S.T. Chang, O. D. Velev, *J. Am. Chem. Soc.* **2007**, 129, 10801.
17. H.-J. Koo, J.-H. So, M. D. Dickey, O. D. Velev, *Adv. Mater.* **2011**, 23, 3559.
18. H.-J. Koo, S. T. Chang, J. M. Slocik, R. R. Naik, O. D. Velev, *J. Mater. Chem.* **2011**, 21, 72.
19. J.-H. Han, K. B. Kim, H. C. Kim, T. D. Chung, *Angew. Chem*. **2009**, 121, 3888.
20. L. Mandal, M. Deo, A. Yengantiwar, A. Banpurkar, J. P. Jog and S. Ogale, *Adv. Mater.* **2012**, 24, 3686.
21. V. Gautam, M. Bag, K. S. Narayan, *J. Phys. Chem. Lett*. **2010**, 1, 3277.
22. A. A. VaÏpolin, Y. A. Nikolaev, V. Y. Rud, E. I. Terukov and N. Fernelius, *Semiconductors*, **2003**, 37, 178-191.
23. F. Guo, B. Yang, Y. Yuan, Z. Xiao, Q. Dong, Y. Bi and J. Huang, J. *Nat. Nanotech*. **2012**, 7, 798.
24. M. Ghosh, A. K. Raychaudhuri, *Appl. Phys. Lett*. **2011**, 98, 153109.

CHAPTER 5

Nonvolatile Memory Transistor Using Poly (vinylidene-hexafluoropropylene)-Clay Nanocomposite

We report a nonvolatile memory transistor using zinc oxide (ZnO) as the channel and Poly(vinylidene fluoride-co-hexafluoropropylene) (PVdF-HFP) clay nanocomposite as the gate dielectric. Field effect transistor (FET) made with pure PVdF-HFP gate dielectric is linear since in this case PVDF-HFP is in the α-phase, a linear high κ form. Addition of clay induces formation of the ferroelectric β-phase in the nanocomposite. The corresponding nonvolatile memory thin film transistor made on glass substrate shows maximum operating voltage of 100 V and mobility of 1 $cm^2V^{-1}s^{-1}$.

5.1 Introduction

Nonvolatile memory (NVM) transistors have attracted significant interest because of their applications in active nondestructive readout memory devices.[1-4] NVM can be broadly classified into two types: a) Floating gate memory transistor, and b) Ferroelectric memory transistor. In Floating gate memory transistor the bistable state of NVM arises due to tunneling and storage of the charges from the semiconductor into the floating gate[5,6]; whereas in the ferroelectric FETs (Fe-FET) the bistable state of the NVM arises due to the two states of polarization of the ferroelectric which can be controlled by the gate voltage.[1-4]

NVMs based on ferroelectric polymers (like poly(vinylidene difluoride) (PVdF) and its copolymers such as PVdF-TRFE) are very interesting as they can be solution processed on plastic and glass substrates, and are flexible in comparison to their inorganic counterpart like PZT. Solution processed NVM devices can be made using these ferroelectric polymers with both, organic or inorganic channels. PVdF and its copolymers are also well known to be high κ and high breakdown strength polymers.[7-9] Due to these property features PVdF, its copolymer, and their nanocomposites are used in high energy density capacitors and linear transistors with low operating voltage. PVdF-HFP is another copolymer of PVdF with high κ and high energy density with 4 possible polymorphs, namely α, β, γ and δ as for PVDF. Depending on the processing conditions the polymer can go into one of these forms, but due to the bulky HFP group the copolymer is a relaxor ferroelectric and generally stays in α phase.

More recently high performance enhancement was shown in a TFT using n-type organic semiconductor channel with high κ PVdF-TrFE as the gate dielectric.[10] Another high-κ copolymer of PVdF; poly(vinylidene fluoride-trifluoroethylene-chlorofluoroethylene) (P(VDF-TrFE-CFE)), used as a gate dielectric, has also been shown to yield a low operating voltage pentacene based FET.[11,12] Flexible non-volatile multilevel ferroelectric memory has also been demonstrated using PVdF-TrFE as the ferroelectric gate dielectric with P3HT channel.[2] Further, ferroelectric nonvolatile memory transistor is shown using PVdF-CTFE as a dielectric.[6] Similarly, an ion gel

made from an ionic liquid and PVdF-HFP has been employed as an electric double layer (EDL) dielectric in a P3HT based FET.[14]

Various NVM transistors have been reported with PVdF and PVdF-TrFE but none with PVdF-HFP to the best of our knowledge. Herein, we show a successful implementation of a non-volatile memory transistor with PVdF-HFP and clay nanocomposite as the gate dielectric and zinc oxide semiconductor as the channel. The dielectric layer was deposited by spin coating while the ZnO layer was grown by radio frequency (rf) sputtering. The FETs made with pure PVdF-HFP as dielectric were found to be linear (no hysteresis) with saturation mobility of 2 $cm^2V^{-1}s^{-1}$; whereas the FET with PVdF-HFP/10 wt.% clay nanocomposites were found to be the NVM-FETs with saturation mobility of 1 $cm^2V^{-1}s^{-1}$.

5.2 Experimental Section

Material

Poly(vinylidene-co-hexafluoropropylene) (PVdF-HFP), a random copolymer of PVdF with 4 - 6% HFP as confirmed by NMR, was procured from Sigma Aldrich. Commercially available organically modified clay Cloisite 20A was procured from Southern clay (USA). Zinc oxide pellet for sputtering was made by using high purity ZnO nanopowder obtained from Sigma Aldrich. Research grade organic solvent acetone was also purchased from Sigma Aldrich.

ZnO thin film deposition

The devices were made using corning 1737 glass as the substrate. First, these glass substrates were cleaned with a detergent, DI water and acetone sequentially, by sonication for 15 minutes each. ZnO films were deposited on the cleaned glass substrates at room temperature by radio frequency (rf) sputtering at 6×10^{-3} mbar pressure in Ar/O_2 (9:1) mixture at 100 W rf power for 5 minutes.

Device Fabrication

All the devices were made in the top gate bottom contact configuration with ZnO as the active channel material. The inset of **Figure 5.2 d** shows the device structure of this ZnO based thin film transistor. The source drain electrodes were made using aluminum deposited by thermal evaporation (at a base pressure 7×10^{-6} mbar) by keeping a metal wire as shadow mask to define the channel. The length and width of the as-formed channel were 90 and 2000 µm, respectively. Various devices were made using (i) PVdF-HFP and (ii) PVdF-HFP/10 wt. % clay nanocomposite as dielectric. For dielectric layer the 10 wt. % solution of PVdF-HFP or PVdF-HFP/clay nanocomposite in acetone was made; the solution was kept for stirring for 2-3 hours. Then the polymer film was deposited by spin coating the solution at 3000 rpm for 60 s. The as-formed film was then annealed in a vacuum oven at 135 ^{o}C for 2 hour, and then allowed to cool to room temperature. Annealing was done to increase the crystallinity of the film (as PVdF-HFP is a semi-crystalline polymer). Finally, the device was completed by top aluminum gate electrode deposited by thermal evaporation.

To measure the capacitance per unit area C_i and ferroelectric loop, metal insulator metal (MIM) structures were fabricated using Al as top and bottom contacts sandwiching the polymer layer.

5.3 Characterization

Electrical Characterization

All the current voltage (I-V) measurements on the TFTs were performed under ambient conditions using Keithley 2400, 2410 source measure units and 6517 electrometer. The capacitance-voltage (C-V) measurement was taken in Novo control impedance analyzer.

The film thickness was measured by Dektak profilometer. Spin-coated PVdF-HFP and its clay nanocomposites were characterized by X-ray diffraction (XRD) (Philips

X'pert pro), and Attenuated Total Reflectance (ATR) (Perkin Elmer). The ferroelectric properties of the PVdF-HFP/10 wt.% clay nanocomposites were checked by fabricating metal insulator metal structure using Al top and Bottom electrode on PVdF-HFP/10 wt.% clay film using Aixact ferroelectric loop tracer.

5.4 Results and Discussion

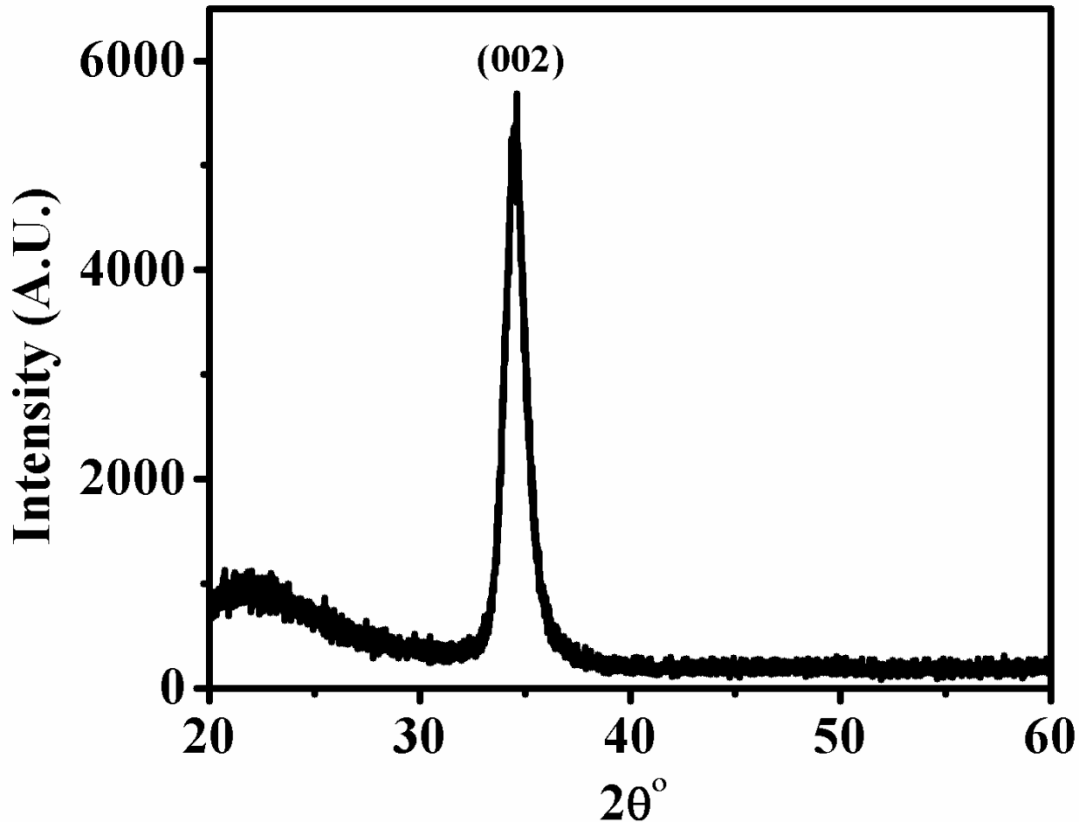

Figure 5.1: *XRD of ZnO thin film deposited by rf Sputtering*

The as-deposited ZnO films were transparent, and polycrystalline as confirmed by X-ray diffraction (XRD) with preferential (002) orientation normal to the film plane see **Figure 5.1** The thickness of ZnO film was about 70 nm as measured by Dektak profilometer.

Figure 5.2 a show the ATR spectra of the pure PVdF-HFP polymer film. The vibration bands at 612,763,796,855, 970, 1150, 1214 and 1383 cm^{-1} are assigned to the α phase of the polymer whereas the vibration bands at 840 and 1278 cm^{-1} are assigned to the β phase of the polymer. All the α phase peaks present in the spectrum with only small peaks or a hump at 840 cm^{-1} indicate that the spin-coated PVdF-HFP film predominantly goes into paraelectric α phase. As the spin-coated film goes into the paraelectric α phase the characteristics of FETs made using PVdF-HFP as a dielectric are expected and found to be linear (the I-V does not show hysteresis).

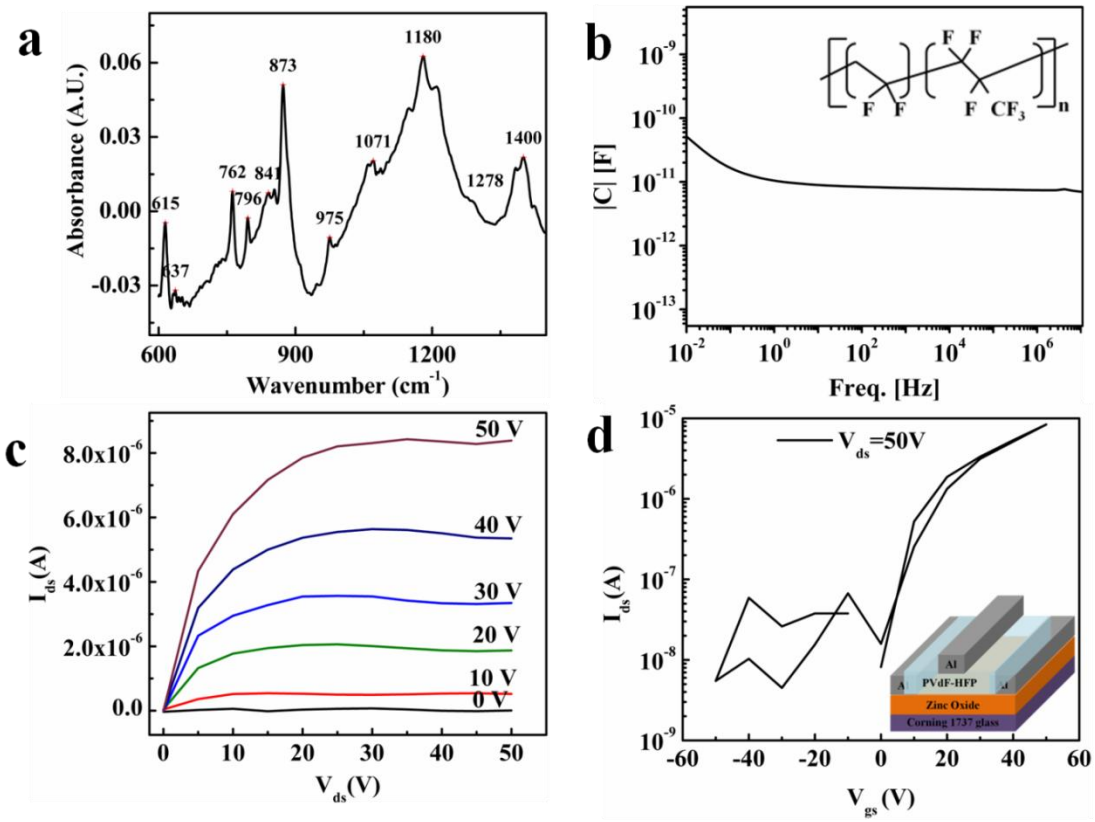

***Figure 5.2: a**. ATR spectrum of spin coated and annealed PVdF-HFP film; **b**. The capacitance of PVdF-HFP spin coated film as function of frequency, inset shows the chemical structure of the copolymer; **c**. output (I_{ds} - V_{ds}) characteristics of FET; **d**. Transfer characteristics (I_{ds} – V_g) curve, inset shows the schematic of ZnO as channel PVdF-HFP as dielectric based thin film transistor.*

The inset of **Figure 5.2 d** depicts the schematic of the as-fabricated TFTs with pure PVdF-HFP polymer as dielectric. **Figure 5.2 c** shows the output (I_{ds} - V_{ds}) characteristics of the TFT. The maximum "on" state current of this device is larger than 5 × 10^{-6} A for operating voltage of 50 V applied to the transistor corresponding to a field of 0.3 MV/cm. PVdF and its copolymers are well known for high dielectric constant and high DC breakdown strength.[7-9] The copolymer PVdF-HFP and its nanocomposites show high breakdown voltage and are used in high energy density capacitors. This PVdF-HFP transistor can thus work even for 200 V. Here, the thickness of PVdF-HFP layer used was 1 μm, hence high voltage was required.

The output characteristics show that these TFTs work as n-type transistors working in enhancement mode. When the gate voltage is increased above the threshold voltage, the charges accumulate on the ZnO at the ZnO/PVdF-HFP interface. **Figure 5.2 d** shows the transfer characteristics (I_{ds} - V_g) for the same transistor at V_{ds} = 50 V. When the transfer curve is taken in double mode (i.e. V_g is increased from 0 to 50 V and back to 0 V), no or negligible hysteresis is seen as shown in **Figure 5.2 d**.

The mobility in the saturation region is calculated using the equation given below

$$\mu_{sat} = \left(\frac{\partial\sqrt{I_{ds}}}{\partial V_g}\right)^2 \frac{2L}{WC_i}$$

Here, W and L are respectively the length and width of the channel. C_i is the capacitance per unit area of the insulator layer, and V_{th} is the threshold voltage for the transistor.[4] The saturation mobility is calculated by plotting $\sqrt{I_{ds}}$-V_g in the saturation region and taking the slope. The device shows effective saturation mobility of 2 $cm^2V^{-1}s^{-1}$. The threshold voltage was calculated by fitting a straight line to the plot of $\sqrt{I_{ds}}$ vs. V_g and extrapolating the straight line to y = 0. The calculated V_{th} is thus 7 V. The device shows an I_{on}/I_{off} ratio of 10^3.

Clay is known to induce ferroelectric β phase in PVDF [15] and PVDF-HFP[16]. **Figure 5.3 a** shows the ATR of PVdF-HFP/10 wt.% clay nanocomposite melt pressed film and spin coated film. The ATR shows transformation from α phase to β phase due to

the addition of clay (i.e. clay induces phase transformation in PVdF-HFP). The peaks at 762 and 796 cm^{-1} correspond to α phase of the polymer, whereas the peak at 840 cm^{-1} corresponds to ferroelectric β phase of the polymer. The nanocomposite shows predominantly the peak at 840 cm^{-1} (corresponding to β phase), whereas the peaks at 762 and 796 cm^{-1} are suppressed. The peak at 870 corresponds to amorphous phase of the polymer.

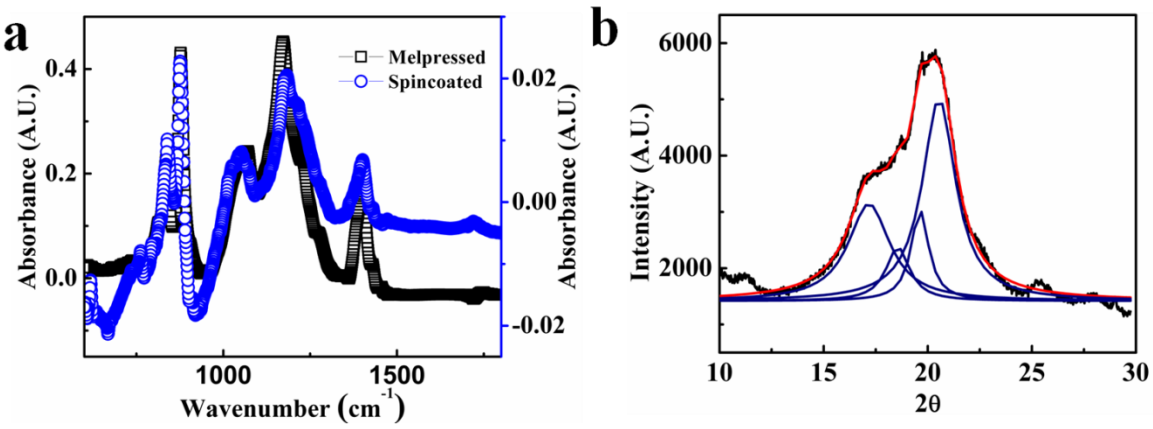

Figure 5.3: a*. Comparison of ATR spectra of melt-pressed and spin-coated PVdF-HFP +10 wt.% clay composite;* ***b.*** *XRD of spin-coated PVdF-HFP+10 wt.% clay composite.*

Figure 5.3 b shows the XRD pattern for the PVdF-HFP/10 wt.% clay nanocomposite. It indicates that the nanocomposite is predominantly in the ferroelectric β phase (as the peak at 20.5˚ is assigned to β phase and its intensity is much higher in the nanocomposite. The copolymer is less crystalline than the PVdF homo-polymer due to the bulky HFP group. Clay induces the ferroelectric phase (β) due to the confinement of the polymer between the rigid clay nano-filler, and PVdF is known to go into ferroelectric phase under confinement. Other nanofillers like CNT, graphene and Ag nanoparticle are also known to induce ferroelectric phase in PVdF.

A nonvolatile memory field effect transistor could thus be made using the PVdF-HFP/10 wt. % clay nanocomposites as gate dielectric (The device using PVdF-HFP/Clay nanocomposites shows hysteresis). **Figure 5.4** shows the output and transfer curves of the

nonvolatile memory transistor. Inset shows the device schematic. The bistability due to nonvolatile memory effect is clearly seen in the transfer characteristics in **Figure 5.4 b** The drain voltage was fixed at 80 V and the gate voltage was swept between -100 to 100 V starting from 0V to 100 V then -100V keeping the source grounded. The gate current was < 0.1% of the drain current for every gate voltage i.e. there is negligible leakage current and the drain current is predominantly due to charge flow through the semiconductor. The drain current is negligible for negative gate voltage since zinc oxide is n-type conductor and at negative gate voltages there are no mobile charges at the ZnO and dielectric interface. Here we observe that when V_g is 0, I_{ds} is still saturated due to the nonpolar H-F dipole with the F-atom oriented toward ZnO. When a negative voltage is applied the current starts decreasing due to reversal of H-F dipole orientation. It is observed that the transistor maintains the on or off state even after the removal of gate voltage.

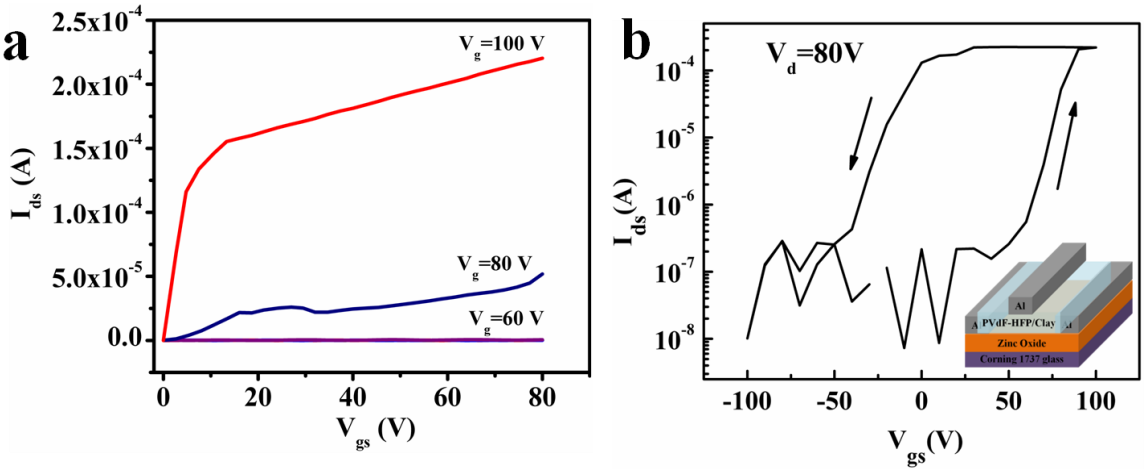

Figure 5.3: a. *I_{ds}-V_{ds} and* ***b.*** *I_{ds}-V_g curves for the device with PVdF-HFP+10 wt.% clay as the dielectric and ZnO as the channel in FET, inset shows the schematic of the device*

Figure 5 a show the I-V curve for the dielectric. The capacitance of the nanocomposite film was calculated in MIM structure using Nova control impedance analyzer. The calculated capacitance value of a dielectric layer of thickness 1 μm is C_i = 5.26 nF/cm^2. Using device parameters of channel length 90 μm, and channel width 2500 μm, the calculated mobility is 0.95 cm^2/Vs and I_{on}/I_{off} > 10^3.

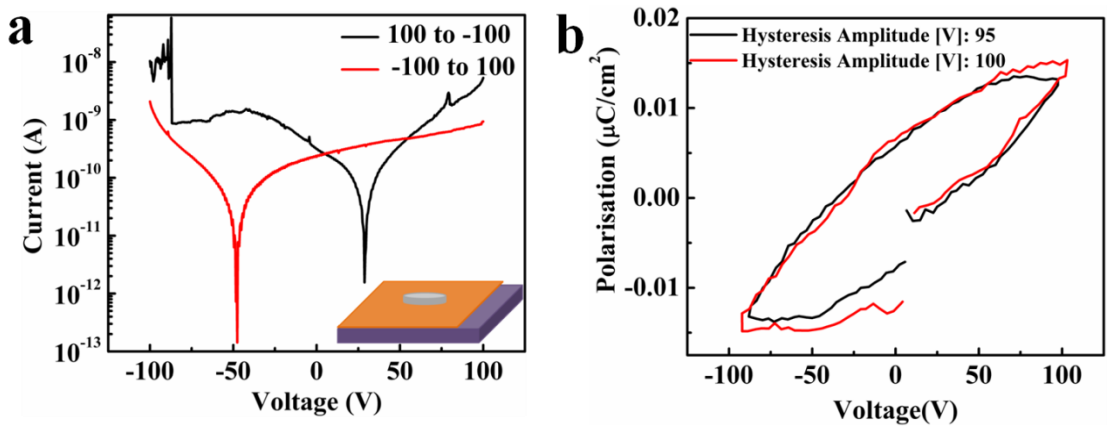

Figure 5.4: a*. I-V of PVdF-HFP clay nanocomposite dielectric; The inset shows the MIM schematic, and* ***b****. The polarization electric field (PE) loop PVdF-HFP/10 wt.% clay spin coated film in MIM configuration.*

In an ideal ferroelectric field effect transistor the density of charges at the semiconductor dielectric interface should be controlled by the electric field applied to the gate and the polarization of the ferroelectric domain of the dielectric layer (due to ferroelectricity). There should be no trapping of charges (bound charges) or interface states (as they can also lead to a hysteresis in the transfer characteristics). Indeed, trapping of charges at the semiconductor dielectric interface is another mechanism for nonvolatile memory FETs.[5,6]

To establish that the hysteresis is because of ferroelectricity, the PE loop in MIM configuration was taken for the PVdF-HFP/clay nanocomposite by AIXAact ferroelectric loop tracer at 100 V, as shown in **Figure 5.4 b** The polarization value is low. However the transfer curve (I_{ds} - V_g) shown in **Figure 5.4 b**, confirms that NVM is due to ferroelectricity of the dielectric. We also observed the current changes in anticlockwise direction for a complete gate voltage cycle from 100 to -100 V. This increase in I_{ds} during backward scan is due to the ferroelectric nature of the dielectric.[1-4] Once the dielectric reaches it saturation polarization, Ids also reaches it saturation. Then the dielectric retains its polarization (I_{ds} is maintaining its saturation value) till a coercive field is applied to reverse the polarization direction. In the case of floating gate NVMFETs, the current changes in clockwise direction for a complete gate voltage cycle (i.e. the current is high

in the forward scan direction and decreases in backward scan due to trapping).[5,6] In our nonvolatile memory transistor we observe the same. The I_{ds} - V_{ds} curve also indicates that on increasing the gate voltage the drain voltage for which the drain current starts to increase decreases drastically. This can be due to the permanent polarization creating more carriers at the interface. In particular, the formation or rearrangement of dipoles at the dielectric-semiconductor interface would have a profound effect on the channel-formation processes that are necessary for the transistor to reach a decidedly "ON" state.

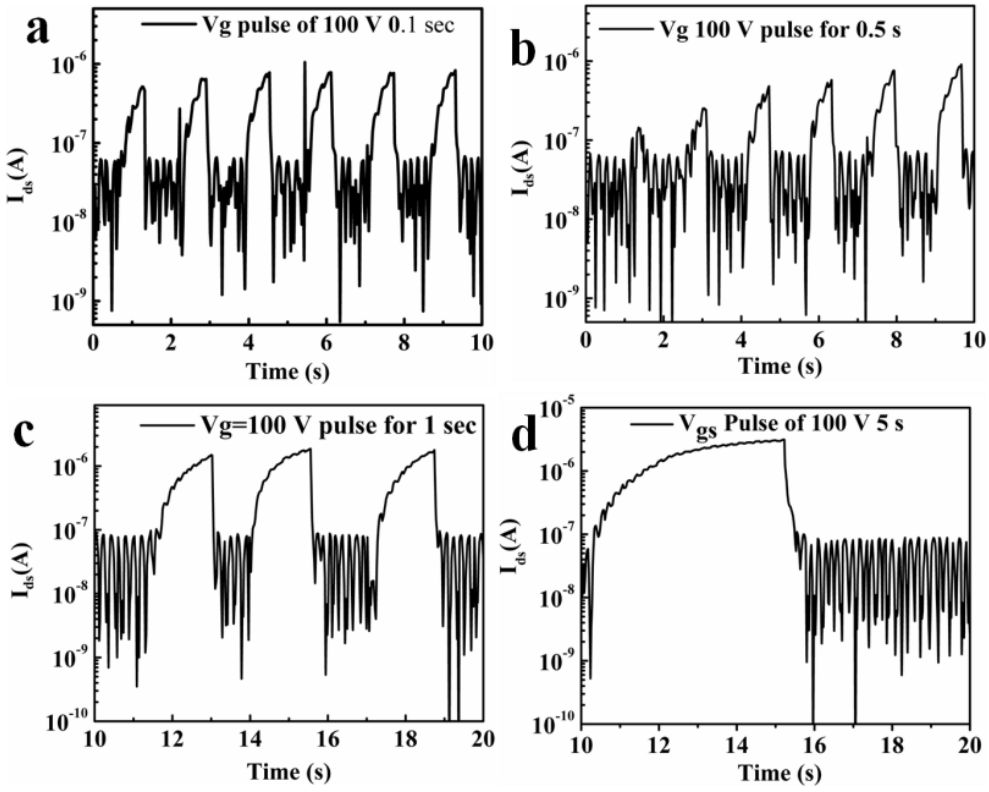

Figure 5.5: *Programmability of the memory FET using PVdF-HFP/10 wt. % clay nanocomposite as a dielectric. Pulsed gate voltage of 100V was applied for different pulse widths:* ***a****. 100 ms,* ***b****. 500 ms,* ***c****. 1 s and* ***d****. 5s.*

In nonvolatile memory FET, the memory is established by writing or erasing using external gate voltage. The dynamic nonvolatile memory property of the PVdF-HFP/10 wt. % clay nanocomposite FET was also studied. **Figure 5.5** shows the result of such study. Repetitive pulses of ± 100V with varying pulse widths of 100 ms, 500 ms, 1 s and 5 s were applied. For a pulse width of 100 ms, our FET showed good differential

I_{on}/I_{off} ratio of around 50. For a pulse width of 5 s the differential I_{on}/I_{off} ratio was seen to increase to 1000. The reported I_{on}/I_{off} retention ratio of 10^3 for nonvolatile memory with ZnO and PVdF-TrFE is 30 with a repetitive 300 ms voltage pulse of ± 20 V. An I_{on}/I_{off} retention ratio of 1000 was noted when a pulse of 20 V was used for 1 s. **Figure 5.6** shows the dynamic retention I_{ds} (I_{on}/I_{off}) as a function of pulse width for ZnO/PVdF-HFP clay composite FET.

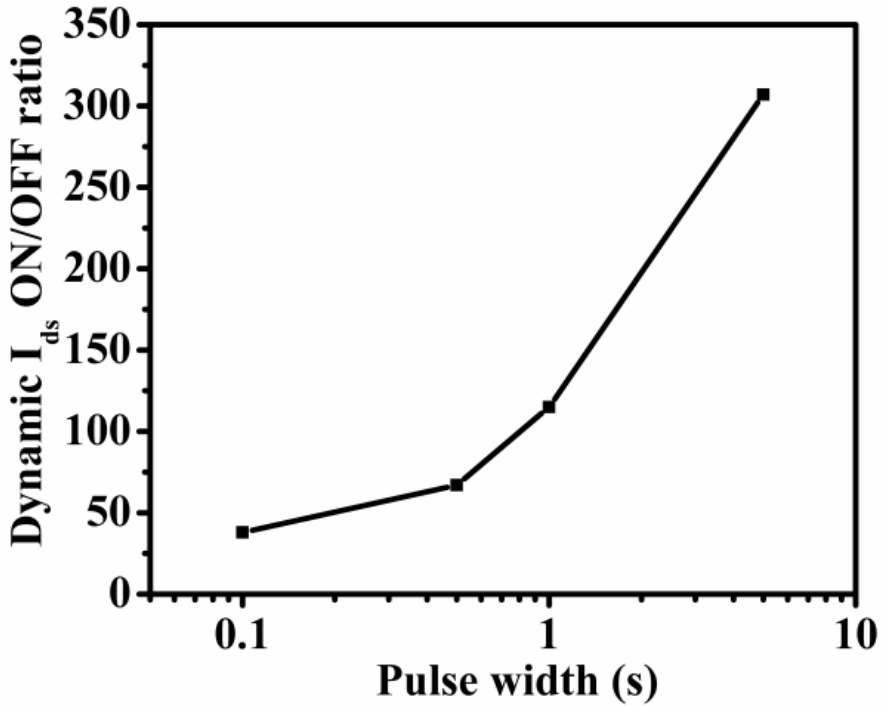

Figure 5.6: *Dynamic I_{on}/I_{off} ratio as function of V_g pulse width.*

5.5 Conclusions

In conclusion we report a nonvolatile memory (NVM) transistor using zinc oxide (ZnO) as the channel and Poly(vinylidene fluoride-co-hexafluropropylene) (PVdF-HFP) clay nanocomposite as the gate dielectric. Addition of clay induces formation of the ferroelectric β-phase in the nanocomposite. The corresponding NVM thin film transistor made on glass substrate shows maximum operating voltage of 100 V and mobility of 1 $cm^2V^{-1}s^{-1}$.

5.6 References

1. S. Mathews, R. Ramesh, T. Venkatesan, J. Benedetto, *Science* **1997**, 276, 238.
2. S. K. Hwang, I. Bae , R. H. Kim, C. Park, *Adv. Mater.* **2012,** 24, 5910
3. K. H. Lee, G. Lee, K. Lee, M. S. Oh, S.I Im, and S.-M. Yoon, *Adv. Mater.* **2009**, 21, 4287.
4. K.-J. Baeg, Y.-Y. Noh, H. Sirringhaus, and D.-Y. Kim, *Adv. Funct. Mater.* **2010**, 20, 224.
5. R.C.G. Naber, C. Tanase, P.W.M. Blom, G.H. Gelinck, A.W. Marsman, F.J. Touwslager, S. Setayesh, D.M. de Leeuw, *Nat. Mater.* **2005,** 4, 243.
6. T.-W. Kim, Y. Gao, O. Acton, H.-L. Yip, H. Ma, H. Chen, and A. K.-Y. Jen, *Appl. Phys. Lett.* **2010,** 97, 023310.
7. F. Guan, J. Pan, J. Wang, Q. Wang and L. Zhu, *Macromolecules* **2010,** 43, 384 .
8. X. Zhou, X. Zhao, Z. Suo, C. Zou, J. Runt, S. Liu,S. Zhang, and Q. M. Zhang, *Appl. Phys. Let*. **2009,** 94,162901.
9. P. Kim, N. M. Doss, J. P. Tillotson, P. J. Hotchkiss, M.-J. Pan, S. R. Marder, J. Li, J. P. Calame, and J. W. Perry, *ACS nano* **2009,** 3 ,2581.
10. K.-J. Baeg, D. Khim, S.-W. Jung, M. Kang, I.-K. You, D.-Y. Kim, A. Facchetti , and Y.-Y. Noh, *Adv. Mater.* **2012,** 24, 5433.
11. J. Li, D. Liu, Q. Miao and F.Yan, *J. Mater. Chem*. **2012,** 22, 15998.
12. S. Wu, M. Shao, Q. Burlingame, X. Chen, M. Lin,K. Xiao, and Q. M. Zhang, *Appl. Phys. Lett*. **2013** 102, 013301
13. R. H. Kim, S. J. Kang, I. Bae, Y. S. Choi, Y. J. Park, C. Park, *Organic Electronics* **2012,** 13 491.
14. K. H. Lee, M. S. Kang , S. Zhang , Y. Gu , T. P. Lodge , and C. D. Frisbie, *Adv. Mater.* **2012,** 24, 4457.
15. L. Priya, J. P. Jog, Journal of *Appl. Polym. Sci*. **2003,** 89, 2036.
16. A. Kelarakis, S. Hayrapetyan, S. Ansari, J. Fang, L. Estevez, E. P. Giannelis, *Polymer* **2010,** 51, 469.

CHAPTER 6

Effect of Semiconductor-Dielectric Interface on Charge Transport Properties of High Performance, Low Temperature Solution Processed, Indium Oxide Thin Film Transistors*

We report the fabrication of low temperature solution processed indium oxide thin film transistor (TFTs) on SiO_2 and Al_2O_3 dielectrics. In_2O_3 TFTs fabricated at low temperature by combustion method showed field effect mobility (μ_{sat}) = 2.2 cm^2/Vs, on/off ratio of 7×10^6 and threshold voltage V_{th} of 0 V. Low temperature field effect mobility and activation energy for TFTs fabricated on different dielectric was evaluated between 90K to 300 K, resulting in an activation energy of 84 meV on Al_2O_3 dielectric, compared to activation energy of 235 meV on SiO_2 dielectric. Transmission line analysis showed contact resistance to be 25 kΩ-cm.

.

*These experiments were performed at ERI@N, Nanyang Technological University, Singapore.

6.1 Introduction

The demonstration of transparent metal oxide semiconductor based thin film transistors (TFTs) at room temperature on flexible polymer substrate[1] have led to intensification of research in this field. Transparent metal oxide semiconductors (TMOS) are used as alternate for amorphous silicon[2] as the channel materials in TFTs to drive the back panel circuit of commercial flat panel displays. Transparent metal oxide semiconductors are deposited by physical vapor deposition process like RF magnetron sputtering,[3] pulsed laser deposition[1] and chemical vapor deposition.[4] The TMOS based TFTs have wide processing temperature window, high mobility, and can be deposited over large area. Moreover they can be operated at low bias voltage.

Recently, there is a surge of interest to deposit these TMOS systems by solution process methodologies such as spin coating,[5,6] ink-jet printing[7] and dip coating.[8] They can also be deposited by colloid based, sol-gel based and metal salt based processes.[5,9] These methodologies require the deposited film to be annealed at high temperature to undergo condensation, densification and impurity removal to form metal oxide making them incompatible with flexible substrates. Recent reports on lowering the annealing temperature have involved use of metal alkoxide,[10] annealing in O_2/O_3 rich atmosphere,[11] or photochemical oxidation of sol gel films by deep UV irradiation.[12] Chemical process assisted annealing is one such method to lower the annealing temperature.[7,13] It uses acetylacetonate or urea as fuel and metal nitrate salt as oxidizing agent to form metal oxide at lower temperatures.

High κ dielectrics such as Yttrium oxide,[1] Zirconium oxide,[14] Hafnium oxide,[15,16] sodium β Alumina[10] and organic inorganic hybrid dielectrics[13,17] have been explored for the transparent metal oxide TFTs for improved performance. The use of the high κ gate dielectrics for TFTs requires investigation on the high leakage currents, low band gap, interfacial reactions, and surface traps. Charge transport mechanism in amorphous metal oxide semiconductor (AMOS) depends upon various factors such as the mode of metal oxide formation, metal ion ratio, annealing temperature[18] and the gate dielectric capacitance[19]; and shows trap-limited percolation transport in AMOS TFTs.

Here, we have used the combustion method[7, 13] to synthesize the indium oxide (In_2O_3) at low temperature 250 ˚C and deposited the corresponding films using spin coating. Indium oxide is a transparent, wide band, n-type semiconductor with high electron mobility. TFTs were made using SiO_2 and atomic layer deposited (ALD) Al_2O_3 dielectric. The choice of gate insulator material and preparation method is crucial for the performance of AMOS TFTs. Here, we used high κ dielectric to improve electrical performance. We have performed low temp study as a tool to understand the effect of high κ on the activation energy, the transport mechanism, and interface properties in this combustion synthesized metal oxides.

6.2 Experimental Section

Synthesis of In_2O_3 films

The Indium oxide solution was prepared by using indium nitrate as the oxidizing agent, acetylacetonate as the fuel and 2-methoxyethanol as the solvent. 352 mg of indium nitrate was added to 5 ml of 2-methoxyethanol, followed by the addition of 0.2 ml of acetylacetonate as fuel. Then the salts were allowed to dissolve, followed by 100 µL of ammonium hydroxide and the solution was stirred for 12 hours.

Synthesis of Al_2O_3 films

Al_2O_3 was deposited by plasma enhanced atomic layer deposition (PE-ALD, Cambridge Fiji F200). Al_2O_3 was deposited using trimethyl aluminum [$Al(CH_3)_3$] (TMA) and H_2O vapor. TMA and oxygen radicals created by plasma were alternatively released into the reaction chamber under the argon gas protection with the unit cycle of TMA (0.6 s)/waiting (6 s)/ oxygen radical (20 s)/waiting (6 s) to achieve the layer by layer growth of smooth and uniform thin film of Al_2O_3. 500 cycles of deposition resulted in film thickness of 70 nm of Al_2O_3 on silicon substrate verified by profilometry measurement.

Device Fabrication

The In_2O_3 layer was then deposited by spin coating the metal precursor solution on various dielectrics at 3000 rpm for 30 s. The deposited films were annealed at 250 ˚C

on a hot plate in ambient air for 30 minutes. The process was repeated twice to get a final film thickness of 30 nm as confirmed by profilometry measurement. Aluminum source drain contacts were deposited by thermal deposition through physical metal mask to define the channel length and width. The devices were fabricated in bottom gate-top contact configuration.

6.3 Characterization

To confirm the chemical composition and crystallinity of the as formed In_2O_3 film X-ray diffraction (XRD) measurement were carried with using powder XRD (PAN analytical X'pert 1712) with Cu-K_α radiation (wavelength 0.154 nm) operated at 40 kV and 30 mA. The samples were scanned in the 2θ range of 10^o to 50^o.

Electrical Characterization

Transistor measurements were carried out both in air and vacuum using Keithley 4200 semiconductor analyzer. Measurements of temperature dependent mobility of various TFT samples were conducted in the cryogenic probe station (Lakeshore-1200).

6.4 Results and Discussion

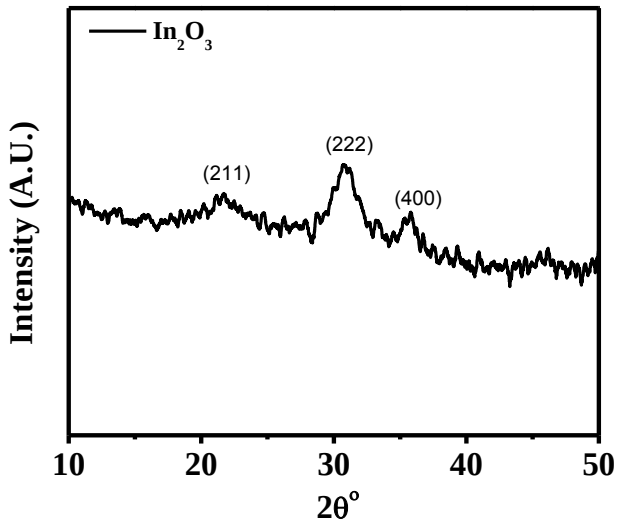

Figure 6.1: *XRD pattern of indium oxide annealed at 250 ^oC on Si/SiO_2 substrate.*

Figure 6.1 shows the XRD pattern of the In_2O_3 film. The XRD data shows that the deposited In_2O_3 film is polycrystalline in nature with (222) and (004) In_2O_3 reflections.[9]

Figure 6.2 a and **b** show the output and transfer characteristics (I_{ds}-V_g) of indium oxide TFT on SiO_2 (600 nm) dielectric having a device dimension of W/L: 75/1000 m. The transfer characteristic was measured in both the linear and saturation region showing n-channel transport behavior. Devices with varying channel width/length (W/L) were fabricated and the summary of their electrical characteristics are presented in **Table 1**. Electrical properties such as $\mu_{sat,}$ I_{on}/I_{off} ratio, threshold voltage, subthreshold sweep and trap density were calculated and are listed in **Table 1** for devices with varying device dimensions. Subthreshold slope is related to the trap states in the channel-dielectric interface and can be calculated by the given equation

$$N_{max} = \left(\frac{C_i}{q}\right)\left(\frac{q.Sloge}{kT} - 1\right)$$

Where q is electron charge, k is Boltzmann constant, T is temperature; C_i is the capacitance per unit area and N_{max} is the interface trap density. The measured trap density for device with L: 100 μm on SiO_2 was $1.7 \times 10^{13}/cm^3$ and Al_2O_3 to be $2.6 \times 10^{11}/cm^3$ showing a drop in trap density on high κ Al_2O_3 dielectrics as seen in the **Table 1** for all the varying channel length. Mobility of indium oxide was calculated to be low (~ 10^{-2} cm^2/Vs) and requirement of high voltage for operation was mainly due to the large thickness of 600 nm of SiO_2 dielectric resulting in average performance.

Dielectric	W=1000 µm L(µm)	μ_{sat} (cm^2\Vs)	I_{on}/I_{off}	V_{th} (V)	S.Sweep (mV/dec)	N_{max} Trap density (cm^{-3})
SiO_2	75	4.4×10^{-2}	10^5	-1.6	5.18	1.6×10^{13}
SiO_2	100	3×10^{-2}	10^6	5.3	5.45	1.7×10^{13}
SiO_2	125	3.6×10^{-2}	10^6	-1.1	6.2	1.9×10^{13}
SiO_2	150	2×10^{-2}	10^5	1.5	8.1	2.5×10^{13}
Al_2O_3	75	2.2	7×10^6	0	$2.7 \text{ x}10^{-1}$	12.6×10^{12}
Al_2O_3	100	2.2	10^6	0.4	$2.8 \text{ x}10^{-1}$	2.6×10^{11}
Al_2O_3	125	1.7	10^6	4.5	$9 \text{ x}10^{-3}$	1.2×10^{11}
Al_2O_3	195	6.3×10^{-1}	10^5	1.9	$5 \text{ x}10^{-3}$	7.7×10^{10}

Table 1: *Summary of electrical parameters for In_2O_3 TFT measured on SiO_2 and ALD Al_2O_3 dielectric measured at fixed channel width W and different channel length L. µ for Field effect mobility, V_{th} for threshold voltage , S. Sweep for subthreshold sweep and N_{max} for trap density.*

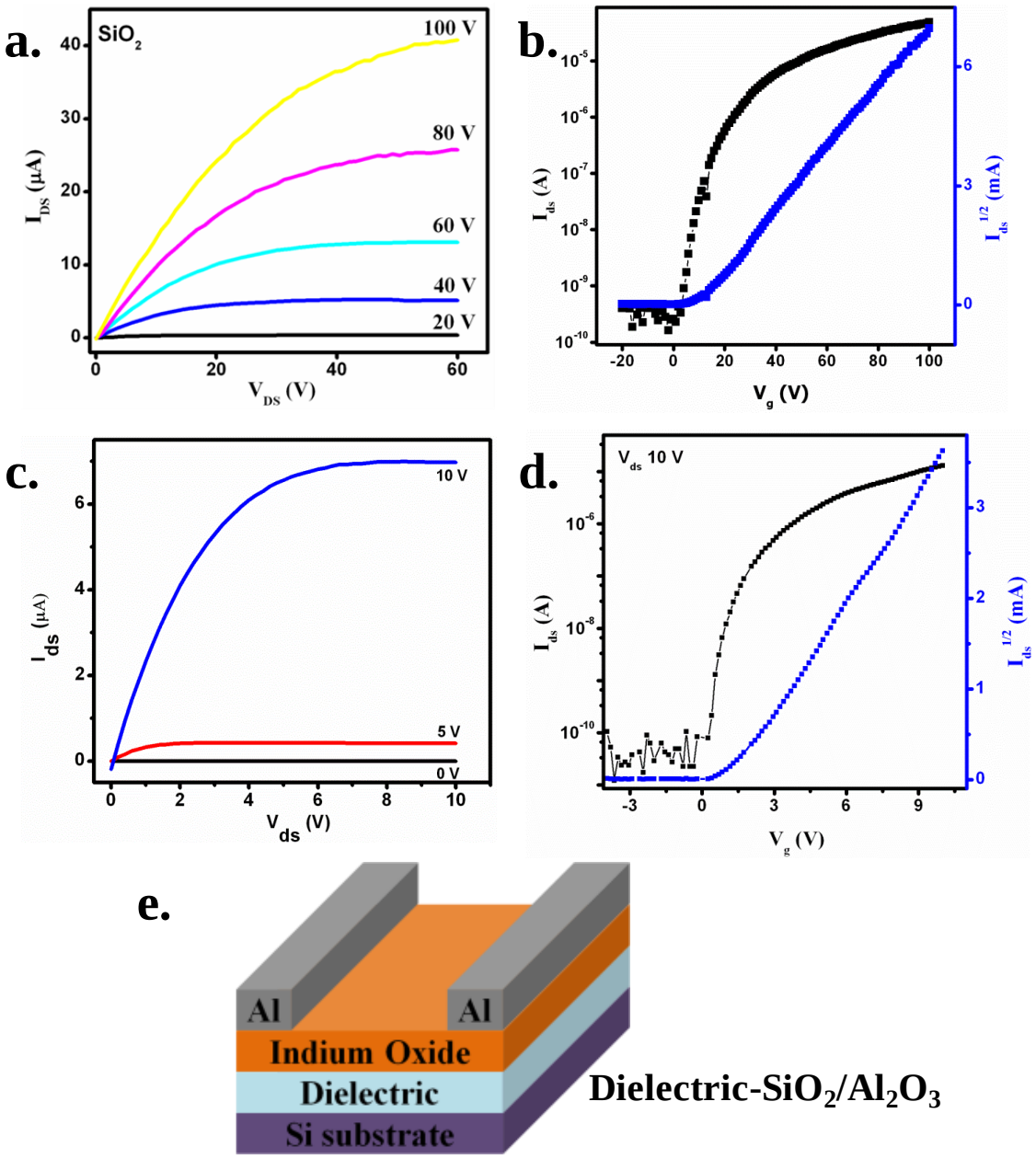

Figure 6.2: a.& b. *The Output characteristics and Transfer characteristics of In_2O_3 TFT fabricated on SiO_2 dielectric with W/L 1000/75 µm ;* ***c.& d.*** *The Output characteristics and Transfer characteristics of device fabricated on 70 nm ALD dielectric having W/L 1000/75 ;* ***e.*** *schematic of TFT.*

Improved device performance was observed with TFTs fabricated on Al_2O_3 dielectric and the areal capacitance of 70 nm ALD dielectric was calculated to be 11.4 nF/cm^2. **Figure 6.2 c, d** show the output and transfer characteristics of the TFTs

measured in the saturation regime (V_{ds} = 10 V), having a channel dimension of W/L = 1000/75 µm. In_2O_3 TFTs on Al_2O_3 dielectrics with different W/L ratio were also studied. The TFT on ALD Al_2O_3 dielectric showed improved performance with a maximum saturation mobility of μ_{sat} = 2.2 cm^2/Vs , on/off ratio (I_{on}/I_{off}) of 7×10^6, low threshold voltage V_{th} of 0 V, subthreshold slope S = 9.7 mV/decade and trap density of 12.7×10^{12} $/cm^3$ for device with W/L = 1000/75 µm. The electrical parameters such mobility, current on/off ratio, threshold voltage, sub-threshold slope and operating voltage all showed improvement just by changing the dielectric material from SiO_2 (κ = 3.9) to Al_2O_3 (κ = 8 - 10). Hysteresis between forward and backward sweep is negligible indicating good interface between both dielectrics and semiconductors.

TFTs with polycrystalline channels generally exhibit an increase in mobility with gate electric field. This increase is attributed to successful filling of gap states at higher gate biases. The improvement in mobility of In_2O_3 TFT on Al_2O_3 as compared to SiO_2 is due to lower density of traps in the former case. In MTR the effective mobility is related to trap density as

$$\mu_{eff}\ \alpha \left(\frac{C_i\left(V_g - V_0\right)}{qN_{trap}}\right)^{\left(\frac{T_c}{T}-2\right)}$$

Where, μ_{eff} is the low-field mobility, C_i is the insulator capacitance per unit area, V_g is the gate voltage, T_c is a characteristic temperature, and N_{trap} is the total density of trap states.

Table 1 show that with Al_2O_3 the trap density is two orders lower than SiO_2.The improvement in mobility has been observed across numerous metal oxide TFT systems, and has generally been explained by higher carrier concentrations achievable at lower voltages using the high-κ. Some of these carriers fill localized states, resulting in devices with higher mobility and more band-like transport.

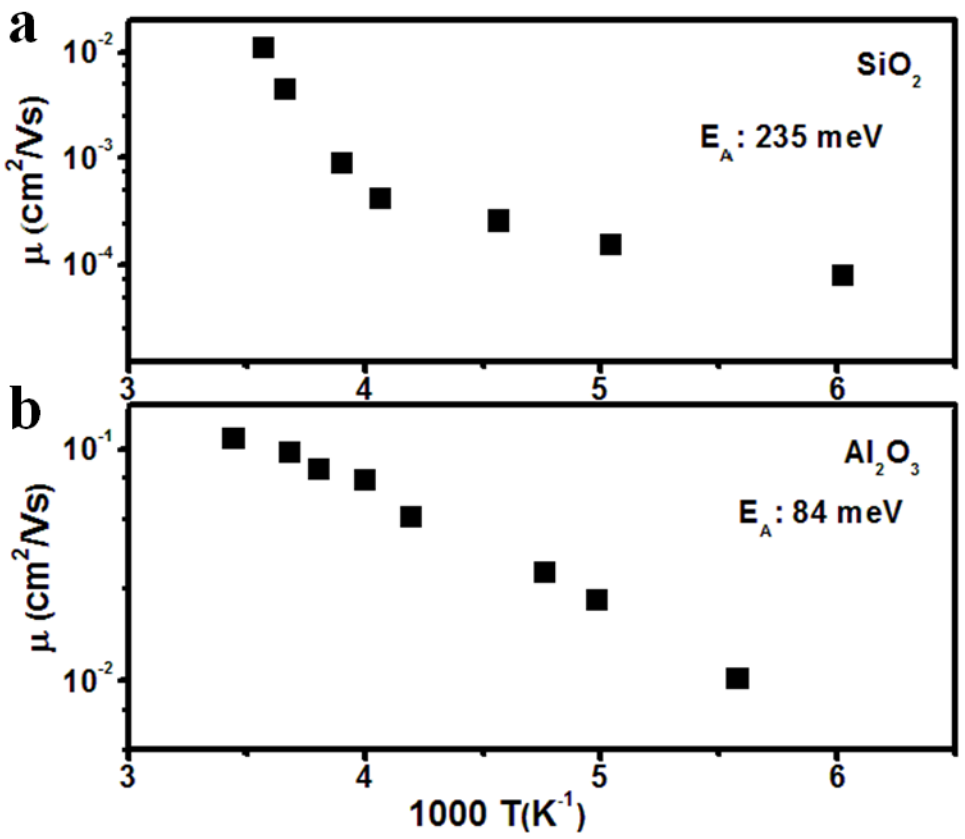

***Figure 6.3**: Temperature dependent mobility for In_2O_3 TFTs on **a**. SiO_2 and **b**. Al_2O_3 dielectric.*

Low temperature studies from 90 K to 300 K were performed to understand the dependence of channel mobility on the semiconductor dielectric interface properties (and traps). **Figure 6.3 a**, **b** shows the semilog plot of μ vs 1000/T on different dielectrics. For TFTs on both the dielectrics, the effective mobility showed strong temperature dependence indicating the thermal excitation of carriers from trap states to the mobility edge. Devices with polycrystalline channels commonly exhibit temperature-dependent transport with an activation energy that is correlated to the grain boundary barrier height, indicative of the defect density at the grain boundaries. For polycrystalline film the mobility is known to be affected by the grain boundaries.[20-22] The mobility in polycrystalline TFTs is given by Levinson's model as,

$$\mu^{-1} = {\mu_0}^{-1} + [\mu_{gb}\left(exp\frac{E_b}{kT}\right)]^{-1}$$

Where, μ_o is the mobility in a crystalline grain, and $\mu_{gb}(exp\frac{E_b}{kT})$ is the contribution accounting for grain boundary scattering. The grain boundary barrier height E_b is given by Levinson model as,

$$E_b = \frac{q^2 N_{trap}^2}{8\varepsilon n}$$

For metal oxides the charge transport can be affected by grain boundaries and high concentration of carriers in the formed channel. The activation energy was found to dependent on gate capacitance yielding 235 meV for SiO_2 and 84 meV for Al_2O_3. Here, In_2O_3 being a polycrystalline film the grain boundary is known to form double Schottky potential barrier by trapping charges and acts as barrier for charge transport (additional source of charge trapping in comparison to AMOS where no grain boundary exist) electrons can either go into the conduction band within the grain or get trapped in the grain boundary. The mobility was found to increase with gate bias, consistent with a standard multiple trapping and release (MTR) model, commonly observed in devices with polycrystalline channels. Most of the polycrystalline TFTs show higher activation energy of 140 meV to 1 eV. The high activation energy for our TFTs is due to the polycrystalline nature of the In_2O_3 film as confirmed by XRD given in **Figure 6.1**. Further on Al_2O_3 the mobility change with 1000/T is 1 order which in SiO_2 case is 2 order in the temperature range of 190 to 300 K this can be due to additional trap states present in SiO_2 as compared to Al_2O_3 which are known to increase the sub-gap density of states (DOS).[19]

This improvement in activation corresponds to improvement in mobility. It has been observed across numerous metal oxide TFT systems, and has generally been explained by higher carrier concentrations achievable at lower voltages using the high-κ. Some of these carriers fill localized states, resulting in devices with higher mobility and more band-like transport.

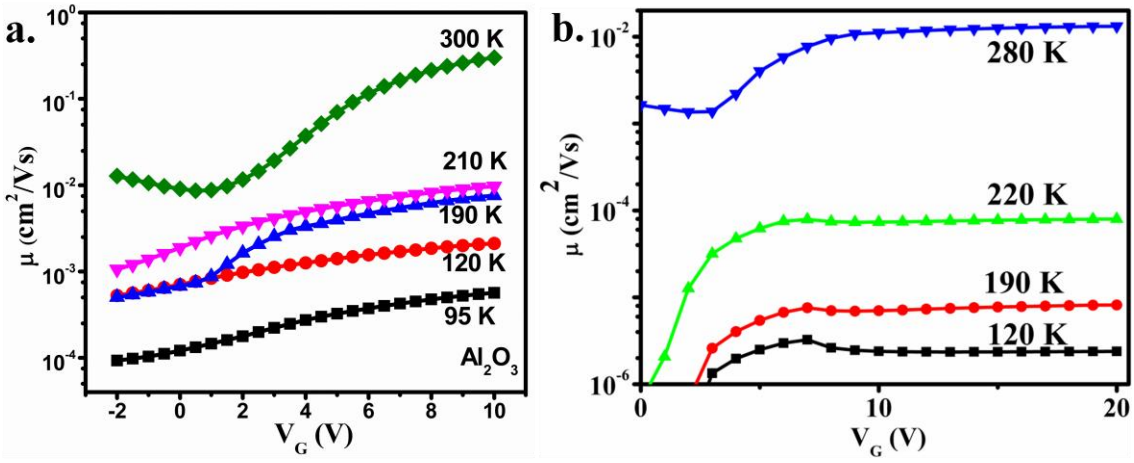

Figure 6.4: a*. Mobility as function of V_g at different temperature for In_2O_3 TFT on Al_2O_3;* ***b.*** *shows mobility as function of V_g at different temperature for In_2O_3 TFT on SiO_2.*

Figure 6.4 a shows linear mobility as function of V_g at different temperature for In_2O_3 Al_2O_3 TFT and **Figure 6.4 b** shows the same plot for In_2O_3 SiO_2 TFT. The effective mobility calculated from trans-conductance increases with both temperature and gate voltage consistent with multiple trap and release model on both the dielectrics. The TFT on Al_2O_3 shows lower activation energy than on SiO_2 indicating much lower trap density in Al_2O_3 which is also supported by high mobility and low subthreshold observed in these devices.

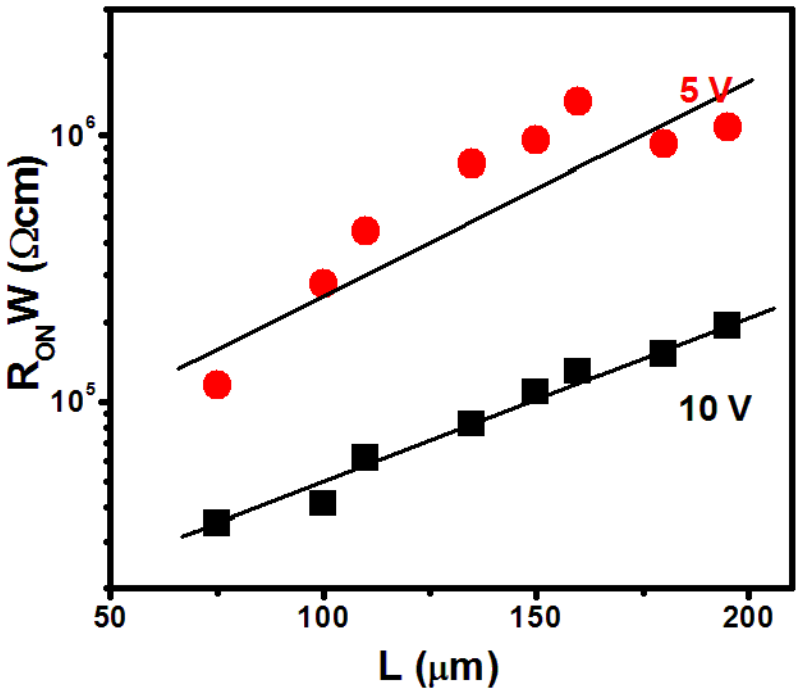

Figure 6.5: *Width normalized total resistance as a function of channel length for In_2O_3 on ALD dielectric.*

In Transparent TFT the contact resistance between source/drain and semiconductor is a key issue to enhance the characteristics such as mobility and threshold voltage. **Table 1** shows the channel length variant properties for indium oxide transistor on both the substrate. To understand the effect of contact resistance on the performance of the TFT the channel length dependent saturation mobility was studied. The parasitic resistance can be calculated by plotting the width normalized contact resistance R_{ON} as function of channel length[23, 24] as shown in **Figure 6.5**. Here, R_{ON} is the total device resistance expressed as

$$R_{ON} = R_C + R_{CH}$$

Where, R_{CH} is channel resistance and R_C is parasitic contact resistance and can be estimated as ordinate extrapolated for zero channel length.[24] **Figure 6.5** shows the $R_{ON}W$ as function of channel length for fixed width of 1000 μm .The contact resistance is dependent on the gate bias and the decrease in contact resistance with higher gate voltage

can be due to higher density of charge carrier in channel at high gate voltage.[25] The width normalized contact resistance comes out as 25 kΩ-cm. The typical value of width normalized contact resistance is~1 for polysilicon, and > 1000 Ω-cm for organic TFTs.[23] Our contact resistance value is higher than that reported for a-IGZO transistor (25 Ω-cm),[3, 26]1550 Ω-cm,[24] 4 kΩ-cm and is responsible for channel length dependence of mobility.

6.5 Conclusions

In this report we have fabricated and studied low temperature synthesized high performance In_2O_3 TFTs on different dielectrics. Improved electrical performance on Al_2O_3 was observed in comparison to SiO_2 dielectrics. Activation energy was evaluated using low temperature studies. The measured mobility follows the simple thermal activated behavior on both the dielectrics. The activation energy was found to have exponential dependency on sheet carrier density. The width-normalized contact resistance comes out as 25 kΩ-cm as calculated from transmission line method and showed gate-voltage dependence.

6.6 References

1. K. Nomura, H. Ohta, A. Takagi, T. Kamiya, M. Hirano and H. Hosono, *Nature*, **2004,** 432, 488 .
2. J. K. Jeong, J. H. Jeong, H. W. Yang, T. K. Ahn, M. Kim, K. S. Kim, B. S. Gu, H.-J. Chung, J.-S. Park, Y.-G. Mo, *J. Soc. Inf. Disp.* **2009,** 17, 95.
3. J. B. Kim, C. Fuentes-Hernandez, W. J. Potscavage, X.-H. Zhang and B. Kippelen, *Appl. Phys. Lett.* **2009,** 94, 142107.
4. K. Remashan, Y.-S. Choi, S.-K. Kang, Je.-W. Bae, G.-Y. Yeom, S.-J.Park, and J.-H. Jang, *Jpn. J. Appl. Phys*. **2010,** 49 04DF20.
5. S. Jeong and J. Moon, *J. Mater. Chem.* **2012,** 22, 1243.
6. C.-G. Lee, B. Cobb, and A. Dodabalapur, *Appl. Phys. Lett.* **2010,** 97, 203505.

7. M.-G. Kim, M. G. Kanatzidis, A. Facchetti and T. J. Marks, *Nat. mater.* **2011,** 10,382.
8. B. N. Pal, B. M. Dhar, K. C. See and H. E. Katz, *Nat. Mater*. **2009,** 8, 898.
9. H. S. Kim, P. D. Byrne, A. Facchetti, and T. J. Marks, *J. Am. Chem. Soc*. **2008,** 130, 12580.
10. K. K. Banger, Y. Yamashita, K. Mori, R. L. Peterson, T. Leedham, J. Rickard and H. Sirringhaus, *Nat. Mater.* **2011,** 10, 45.
11. S.-Y. Han, G. S. Herman, and C.-h. Chang, *J. Am. Chem. Soc.* **2011,** 133, 5166.
12. Y.-H. Kim, J.-S. Heo, T.-H. Kim, S. Park, M.-H.Yoon, J. Kim, M. S. Oh, G.-R. Yi, Y.-Y. Noh and S. K. Park, *Nature* **2012,** 489, 128.
13. J. W. Hennek, M.-G. Kim, M. G. Kanatzidis, A. Facchetti and T. J. Marks, *J. Am. Chem. Soc.* **2012,** 134, 9593.
14. Y. M. Park, J. Daniel, M. Heeney, and A. Salleo, *Adv. Mater.* **2011,** 23, 971.
15. S. Chang, Y.-W. Song, S. Lee, S. Y. Lee, and B.-K. Ju, *Appl. Phys. Lett.* **2008,** 92, 192104.
16. P. F. Carcia, R. S. McLean and M. H. Reilly, *Appl. Phys. Lett*. **2006,** 88, 123509.
17. J. Liu, J. W. Hennek , D. B. Buchholz , Y.-g. Ha , S. Xie ,V. P. Dravid , R. P. H. Chang, A. Facchetti , and T. J. Marks, *Adv. Mater.* **2011,** 23, 992.
18. W. Hu and R. L. Peterson, *J. Mater. Res.* **2012,** 27, TBD.
19. W. Chr. Germs, W. H. Adriaans, A. K. Tripathi, W. S. C. Roelofs, B. Cobb, R. A. J. Janssen, G. H. Gelinck, and M. Kemerink, *Phys. Rev. B* **2012,** 86, 155319.
20. J. Levinson, F. R. Shepherd, P. J. Scanlon, W. D. Westwood, G. Este, and M. Rider, *J. Appl. Phys.* **1982,** 53, 1193.
21. J. Jang, R.t Kitsomboonloha, S. L. Swisher, E. S. Park, H. Kang, and V. Subramanian, *Adv. Mater.* **2012**, 25, 1042.
22. K.-S. Weissenreider and J. Muller, *Thin Solid Films* **1997,** 300, 30.
23. G. Horowitz, P. Lang, M. Mottaghi and H. Aubin *Adv. Funct. Mater.* **2004,** 14, 1069.
24. J. Zaumseil, K. W. Baldwin and J. A. Rogers *J. Appl. Phys.* **2003,** 93, 6117 .
25. S. K. Kim, Y. Xuan, P. D. Ye, S. Mohammadia, J. H. Back and M. Shim *Appl. Phys. Lett.* **2007,** 90, 163108.

26. J. K. Jeong, H.-J. Chung, Y.-G. Mo and H. D. Kim *J. Electrochem. Soc.* **2008,** 155, H873.

CHAPTER 7

Summary and Future Scope

This chapter presents a summary of the work performed during the course of the PhD program with some concluding remarks. It also covers the future scope pertaining to this work.

7.1 Summary of the thesis

The demand for flexible electronic components is increasing in portable handheld displays and communication products due to their light weight, flexibility, shock resistance, low cost and transparency. Flexible electronics on plastic substrates has been approached quantitatively utilizing amorphous silicon, organic semiconductor materials, carbon nanotubes, and nanowires. There are many studies and research on materials systems and processes that are used to fabricate devices that can be employed in a wide variety of applications such as flexible flat-panel displays, sensors, photovoltaics, photodetectors and electronic paper. Wide range of materials is being investigated starting from polymeric semiconductors to nanotubes to transparent conducting metal oxides in the context of these applications.

Solution-processed optoelectronic devices offer large-area coverage, low cost, and compatibility with a wide range of substrates. This offers the potential for monolithic low-cost large-scale integration with CMOS electronics. In addition, progress in organic transistors and their integration have led to the development of large area flexible image sensors.

Solution-processed, high-performance semiconductors have been considered for the manufacturing of low-cost thin-film transistor (TFT) arrays/circuits through newly developed roll-to-roll processes based on a combination of conventional coating and printing techniques such as ink-jet, screen, and gravure printing. To date, a variety of soluble organic semiconductors have been extensively explored as potential materials providing reasonable electrical characteristics. However, these organic semiconductors still suffer from some drawbacks such as relatively low mobility, bias/environmental-stress induced instability, and process-dependent performance.

Transparent amorphous oxide semiconductors have unique electron transport properties, such as large electron mobility (10–50 $cm^2/V\ s$), wide processing route, simple electrode structure and low off current compared to conventional amorphous semiconductors. This class of materials has been attracting much attention as a channel layer in thin-film transistors (TFTs) utilizing the above features along with the processing advantage that

their thin films can be deposited at low temperatures by conventional sputtering methods. The primary motivation for this trend is a rapidly emerging demand for backplane TFTs that can drive the next generation flat-panel displays.

In this thesis we have mainly studied two device systems, namely photodetectors and field effect transistors, fabricated by solution processible routes. The first work deals with novel photodetector designs using some unique features and properties of the interfaces between one or two dimensional inorganic semiconductors and hydrogel. In addition to the explorations of device performance, experiments have been performed to establish the physical mechanisms of these photodetectors. The second work deals with metal oxide based transistors. The nanocomposite of PVdF-HFP/clay is used as dielectric in nonvolatile memory transistor. Finally the transport studies were done on combustion synthesized indium oxide transistors.

The summary of the work done is as follows:

Chapter 3 We have studied the interface between a quasi-liquid ionic conductor and light harvesting configuration of quasi-1D functional metal oxide (ionic-electronic hybrid). This hybrid device yields a highly efficient photodetector that shows strong photoresponse in the UV as well as partial visible range. The electric field induced band bending at the interface and the light harvesting nature of nanorods configuration are together shown to help realize three orders of magnitude higher photocurrent in this device as compared to the case of bare ZnO-nanorods-Pt. Impedance spectroscopy reveals a significant decrease in the charge transfer resistance as well as capacitance of this hybrid device upon illumination. We have further shown that the gel layer remarkably improves the response time and IPCE of ZnO-gel-Pt system in comparison to bare ZnO-Pt system.

Chapter 4 We have demonstrated fabrication of a highly efficient self-powered UV-Vis photo-detector based on $ZnIn_2S_4$ nanopetal film with surface-dispensed agarose gel. The $ZnIn_2S_4$ nanopetals films are grown on FTO-coated glass hydrothermally. The photoresponse of the $ZnIn_2S_4$/gel hybrid device is seen to be higher by a factor of ~100 even for zero bias as compared to the photodetector without gel powered at -1.5V. The

response times (rise and fall) for the $ZnIn_2S_4$ only (i.e. without gel) photodetector is 2 ms whereas the response times for the $ZnIn_2S_4$-gel hybrid device are 25 ms (rise) and 120 ms (fall). Impedance spectroscopy shows decrease in the charge transfer resistance and capacitance in the hybrid device under illumination. The hybrid photodetector shows good responsivity of 16.5 mA/W even at zero bias.

Chapter 5 We report a nonvolatile memory (NVM) transistor using zinc oxide (ZnO) as the channel and Poly (vinylidene fluoride-co-hexafluoropropylene) (PVdF-HFP) clay nanocomposite as the gate dielectric. Addition of clay induces formation of the ferroelectric β-phase in the nanocomposite. The corresponding NVM thin film transistor made on glass substrate shows maximum operating voltage of 100 V and mobility of $1cm^2V^{-1}s^{-1}$.

Chapter 6 We have fabricated and studied solution processible, high performance, and low temperature synthesized In_2O_3 TFTs on Al_2O_3 and SiO_2 as dielectric. Improved electrical performance is observed on Al_2O_3 as compared to SiO_2 dielectric. Activation energy is evaluated using low temperature studies. The measured mobility follows simple thermal activated behavior on both the dielectrics. The activation energy on Al_2O_3 dielectric is found to 84 meV as compared to 235 meV on SiO_2. The width normalized contact resistance comes out as 25 kΩ-cm as calculated from transmission line method and shows a gate voltage dependence.

7.2 Scope for future work

In the literature various inorganic and organic materials along with their hybrids have been explored for photodetector applications. The organic photoactive materials have effective light absorption from ultraviolet to near-infrared a good photo-generation yield and low-temperature processability over large areas and on most substrates. They enable innovative optoelectronic systems to be targeted for instance in the field of imaging, optical communications or biomedical sensing. Similarly 1D, 2D metal oxides and metal

sulfides have also attracted tremendous attention due to the large surface to volume ratio along with low dimension. Recently, there have been a few interesting reports on hybrid visible light photo-detectors using earth abundant or nontoxic elements but these lack the self-powered mode of operation. Therefore, organic-inorganic hybrid photo-detectors operating under self-sufficient power mode are highly desired.

The electrical properties of metal oxides can be varied from metallic to semiconducting to insulator and accordingly used in thin film transistor as electrode, channel or dielectric. As some semiconductor metal oxides have high carrier mobilities, wide band gaps, broad transparency windows, tunable doping levels, and amenability to room-temperature film growth their innovative use in the device systems discussed in this thesis is likely to grow. There is an impressive body of work reported in the literature on solution processed metal oxides with emphasis on decreasing the processing temperature and the operating voltage of the transistors. But, these solution processible metal oxide TFTs are still lacking behind in performance *Vis a Vis* the vacuum deposited TFT's with inferior device parameters such as mobility, threshold voltage etc.

Based on the work, understanding and inferences from the thesis work, a few directions of research can be outlined as follows:

- Research is needed to develop new and cost effective carbon free solution routes (spin coating, dip coating and inkjet printing) to decrease the temperature needed for conversion of precursor(s) into metal oxides. Another key requirement is also to develop high quality smooth, pin hole free dielectrics by compatible solution routes. Furthermore the conversion temperatures should be compatible to the range of stability of the flexible polymer substrates. This is more critical parameter in the case of dielectrics which nominally require high temperature to get pin hole free and high breakdown sustainable film. Finally it is important to develop solution processed p-type metal oxides in order to realize all-metal-oxide based complementary logic circuits.

- The transparent metal oxide based devices constitute a novel and exciting field with great potential for commercial applications. Similarly understanding the physics of operation of these devices is as crucial as developing new materials and novel device designs. One objective would be to extensively study the stability and transport mechanisms (e.g. effect of the precursor route (sol-gel, combustion etc.) used, metal to ion ratio, and annealing temperature) in these metal oxide transistors, as well as the nature of the dielectric-semiconductor interface(s) and the contact resistance in the context of TFTs.

- Another interesting research area is to combine these metal oxides with gel electrolyte as dielectric and study the performance of these electric double layer transistors. The electric double layer dielectrics have exceptionally large specific capacitances originating from nanometer-thick electrical double layers at electrolyte/electrode interfaces, and wide electrochemical windows. They are used as a tool to study transport behaviour and phenomena such as the insulator-to-metal transition in semiconductors.

- Another area is Ionics - that is, the creation of functional electrical devices based upon the flow of ion or proton currents. These devices are truly bio-inspired since in biological systems electrical signals are generally propagated and communicated by the modulation and control of ions and protons, not electrons. These materials and device architectures have wide applications such as energy, sensing, memory, circuit elements, detectors, displays, interactive medicine and integrated health diagnostics. One such area which is bio-inspired is stretchable electronics and more specifically artificial (or electronic) skin. It consists of mechanical, chemical biosensors and actuators, stretchable control circuitry and memory, power sources and energy harvesting. It will be interesting and useful to integrate such ionic systems with the electronic devices.

- The bio-inspired photodetectors employing biocompatible materials have the potential to broaden applications to biometrics and bionics (e.g. artificial retinas).

It would be interesting to explore other biocompatible organic, inorganic metal oxides and metal sulphide interfaces with hydrogel/ionic gel as potential photodetectors and synaptic devices.

- Dielectric materials with high energy storage density are of great importance for the power electronics in pulsed-power, power capacitors, hybrid electric vehicles, medical devices, and electrical weapon systems. Presently polymers and their composites with ceramic particles are preferred for high energy density capacitors because of the combination of high breakdown strength, low cost, and failure-resistant characteristics. It will thus be useful to explore the possibilities of applying high k polymer nanocomposites for non-volatile memory and high energy density applications.

APPENDIX

Optimization Studies on Low Temperature Solution-Processed Indium Zinc Oxide Thin Film Transistors*

Low temperature solution processed Indium Zinc Oxide (IZO) thin film transistors are studied by optimizing the molar ratio of metal salt precursors and the gate dielectric layer. InZnO (saturation mobility: 0.6 cm^2/Vs) channel layer showed a performance intermediate between that of pristine In_2O_3 and ZnO TFTs.

*These experiments were performed at ERI@N, Nanyang Technological University, Singapore.

7.1 Introduction

Metal oxide thin film transistors (TFTs) have attracted great attention in view of their projected applicability in advanced and flexible display systems, where presently amorphous silicon dominates.[1] Due to their high mobility, stability, electrical uniformity over large area and low temperature processability, they are replacing organic semiconductors[2] and hydrogenated silicon [3] as channel materials of interest. Amorphous metal oxide based semiconductors (AMOS) consisting of heavy metal cations with (n-1) $d^{10}ns^0$ ($n \geq 4$) electronic configuration have already shown improved performance over hydrogenated a-Si and organic semiconductors. Most AMOS TFTs are fabricated using vacuum deposition techniques such as pulsed laser deposition,[2] chemical vapor deposition,[4] and RF sputtering.[5] In comparison to the vacuum processing methods the solution processed approaches require high sintering temperature to form metal oxide film. Though vacuum coating methodologies have rendered high performance AMOS TFTs, solution processed techniques have enabled exploration of broad classes of oxide materials and are far less expensive from the fabrication perspective.

When a binary metal oxide (ZnO, In_2O_3 or SnO_2) film is synthesized, it has a tendency to crystallize even at room temperature. However, ternary oxides (InZnO, ZnSnO) and quaternary oxides (InGaZnO) can form either amorphous or polycrystalline thin films depending on the metal ion ratios in the film. Studies have therefore been carried out to understand the effect on metal cation ratio variation on the transport properties of AMOS TFTs.[6] In a-InGaZnO the bonding energy varies as Ga-O > Zn-O > In-O. Pure In_2O_3 usually has large carrier density (due to low binding energy of In-O) resulting in high off currents when employed in TFTs.[7] On adding Ga or Zn in In, the carrier density can be decreased, thereby decreasing the off current and improving the on/off ratio. Thus, the ratio of metal ions can strongly affect the transport and electrical properties in AMOS TFTs.[8-10]

Solution based approaches to form metal oxide films involve dissolving metal salts in either aqueous or organic solvents to form sols. Metal cations are hydrolyzed to

form the solvation shell and then condensed to obtain the metal-oxygen network through the olation or oxalation process.[11] Although solution processed AMOS TFTs show comparable performance to vacuum-processed devices,[12-14] the densification and impurity removal steps for metal oxide formation require high annealing temperature (≥ 400 ^{o}C), making the approach incompatible with flexible substrates. Recent reports have demonstrated a general method to overcome high temperature requirement for metal oxide film formation using deep-ultraviolet photochemical activation of sol-gel films, which allows for efficient condensation and densification of oxide films at low temperature.[15] Another approach involves using self energy generating combustion chemistry which provides localized energy supply, eliminating the need for external high temperature. Such an approach uses metal nitrate salts as oxidizers and acetylacetone as the fuel to form metal oxides.[16]

In this Appendix, we report initial results of our studies of TFTs in solution processed films of $In_xZn_{1-x}O$ with x = 0, 0.5, 0.7 and 1.0 in conjugation with two gate dielectric systems, namely SiO_2 and Al_2O_3.

7.2 Experimental Section

Device Fabrication

The metal oxides used in this work were synthesized using combustion chemistry.[16] Zinc oxide and indium oxide precursor solutions were made by dissolving 297 mg and 352 mg quantities of zinc nitrate and Indium nitrate, respectively, in 5 ml 2-methoxyethanol and 0.2 ml of acetylacetonate. The solutions were kept for stirring to dissolve the metal salts and 100 µL of ammonium hydroxide was added to each metal precursor solution followed by further stirring for 12 hrs. Indium zinc oxide precursor ($In_xZn_{1-x}O$) solution was then prepared by mixing Indium oxide precursor and zinc oxide precursor solutions in ratios of (7:3) and (5:5) and stirred for 1 hour prior to film deposition. The precursor solution in each case was spin-coated at 3500 rpm on 600 nm SiO_2 dielectric and annealed at 250 ^{o}C in ambient air for 30 minutes to form the metal oxides. The process was repeated twice to form a film thickness of ~ 30 nm as measured using profilometer. Identical procedure was repeated on plasma enhanced atomic layer

deposited Al_2O_3 dielectric (Cambridge Nanotech-ALD system) having 70 nm thickness. Aluminum, used as the source-drain electrodes, was thermally evaporated through a physical mask to obtain devices with varying channel length and width.

7.3 Characterization

Electrical Characterization

The devices were fabricated in a bottom-gate, top-contact configuration, and electrical measurement were carried out in Lakeshore Cryo probe station connected to Keithley 4200 semiconductor parameter analyzer.

Film Characterization

To confirm conversion of precursor into the desired oxide the chemical composition and crystallinity of the as-formed thin film; X-ray diffraction (XRD) measurement were carried with using powder XRD (PAN analytical Xpert 1712) with Cu-K_α radiation (wavelength 0.154 nm) operated at 40 kV and 30 mA. The samples were scanned in the 2θ range of 10^o to 50^o.

7.4 Results and Discussion

In transparent metal oxide TFT, the metal oxide film can be amorphous or polycrystalline depending on the metal ion ratio and annealing temperature. **Figure 1** shows the semi-log XRD plot of the combustion synthesized ZnO, In_2O_3 and IZO films. The XRD data confirm that the deposited ZnO film is polycrystalline in nature with (100), (002) and (101) ZnO reflections. The deposited In_2O_3 film is also polycrystalline with (211), (222) and (400) reflections. However, the deposited IZO ternary oxides film is amorphous in nature. All the films show high optical transparency in the visible region with Absorbance < 30% as shown in **Figure 1 d.**

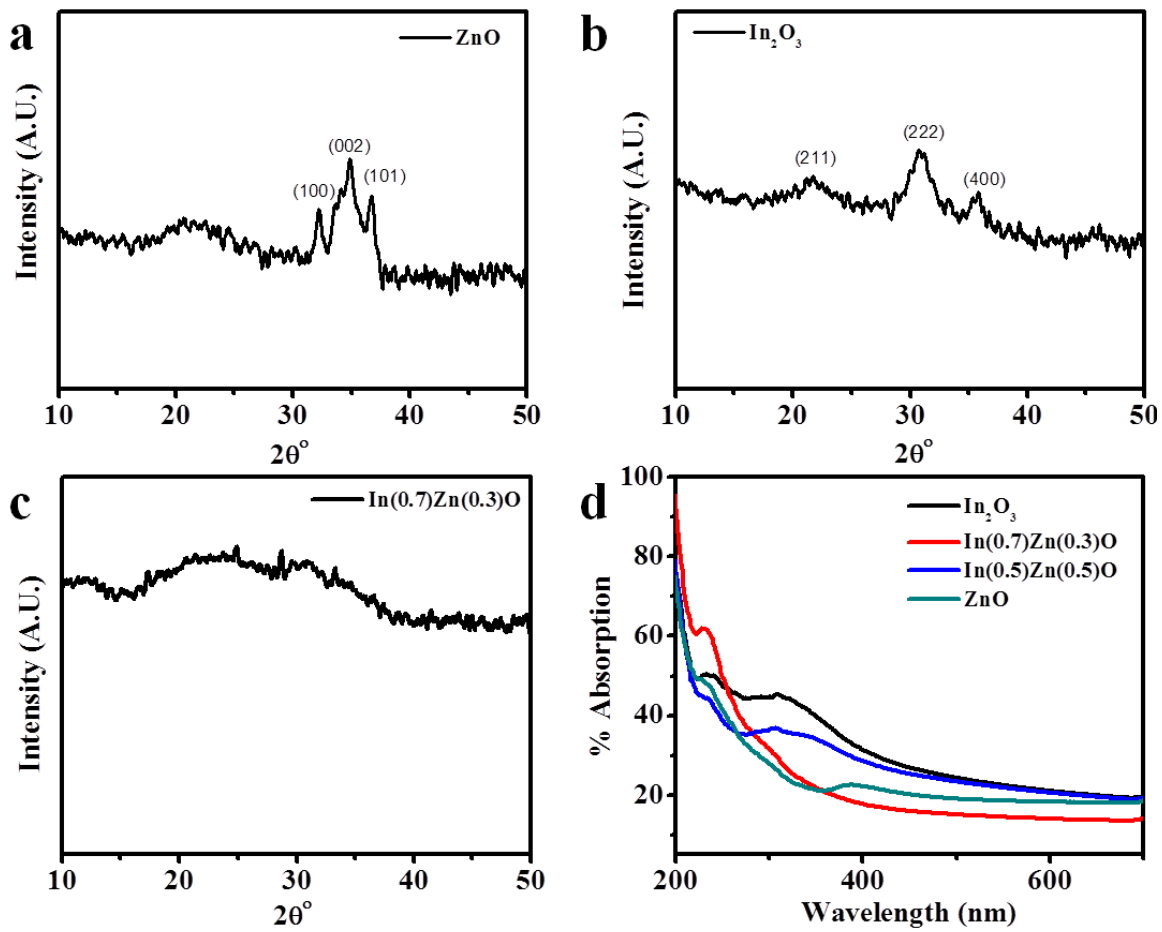

Figure 1: *XRD of combustion synthesized films annealed at 250 °C* ***a****. ZnO,* ***b****. In_2O_3, and* ***c****. IZO;* ***d****. DRS spectra of all the films*

The electrical characteristics of the TFTs were measured under ambient conditions at room temperature. The transfer characteristic was measured in the both the linear and saturation region showing n-channel transport behavior. **Figure 2 a** shows the I_{ds}-V_{ds} output characteristics of $In_{0.5}Zn_{0.5}O$ fabricated on SiO_2 dielectric showing n-channel transport in enhancement mode. The I_{ds}-V_g transfer characteristics of In_2O_3, ZnO and IZO with varying molar ratio measured at V_{ds} 60 V are shown in **Figure 2 b. Table 1** summarizes the extracted parameters for different TFTs fabricated on the SiO_2 substrate. The device dimension W/L for the TFT measured on SiO_2 dielectric was 1000/125 µm. The saturation field effect mobility μ_{sat} was extracted from $\sqrt{I_{ds}}$-V_g plot and was calculated for TFTs with varying molar ratio. Indium has a strong influence on the electrical properties of the TFT acting as a conductive component. Pristine ZnO and

In_2O_3 showed saturation mobility of 3.5 × 10^{-2} cm^2/Vs and 2.8 × 10^{-2} cm^2/Vs, respectively. IZO with equimolar ratio of Zn:In resulted in an improved performance with max mobility of 6.7 × 10^{-2} cm^2/Vs, on/off ratio of 10^5 and threshold voltage of V_{th} 6.7 V. Mobility of all oxide was calculated to be low (~ 10^{-2} cm^2/Vs). The requirement of high voltage operation was mainly due to the large thickness of 600 nm of SiO_2 dielectric.

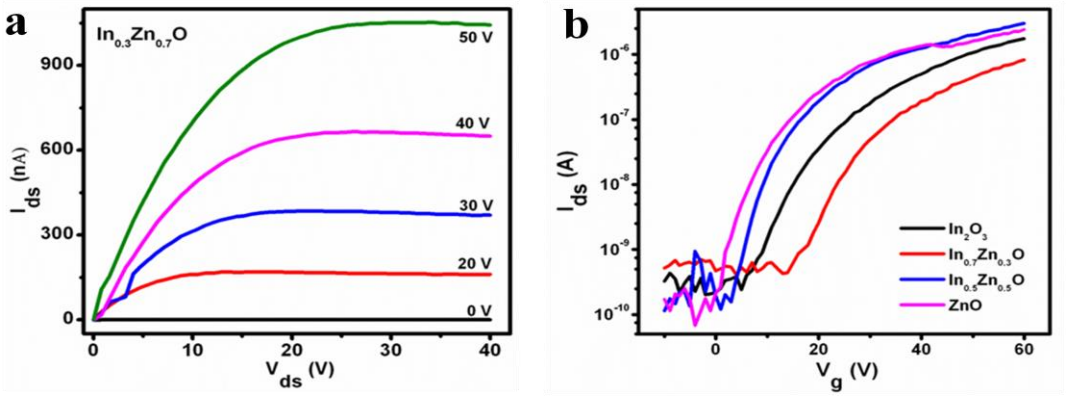

Figure 2: *a) Output characteristics for $In_{0.5}Zn_{0.5}O$ TFT on SiO_2 dielectric with W/L ratio of 1000/125 µm, (b) Transfer characterstics of TFTs with varying molar ratio of In:Zn having W/L ratio of 1000/125 µm*

Zn Conc. (%)	**In Conc. (%)**	**W/L (µm)**	**μ_{sat} (cm^2\Vs)**	**I_{on}/I_{off}**	**V_{th} (V)**	**S.Slope**	**S.Sweep (mV/dec)**	**N^{max} Trap density**
100	**0**	**1000/125**	**0.035**	**5 × 10^4**	**-0.56**	**0.26**	**3.78**	**1.2 × 10^{13}**
30	**70**	**1000/125**	**0.024**	**1 × 10^4**	**6.20**	**0.14**	**6.95**	**2.2 × 10^{13}**
50	**50**	**1000/125**	**0.067**	**1 × 10^5**	**-2.05**	**0.17**	**5.72**	**1.8 × 10^{13}**
0	**100**	**1000/15**	**0.028**	**1 × 10^4**	**0.5**	**0.26**	**3.78**	**1.1 × 10^{13}**

Table 1: *Electrical parameters for the various fabricated TFTs on SiO_2 dielectric measured at different In:Zn metal ion ratio. µ is the field effect mobility, V_{th} is the threshold voltage, and N^{max} is the trap density, S.Slope is $\frac{\partial I_{ds}}{\partial V_{gs}}$, S Sweep is subthreshold slope.*

To further improve the performance and study the effect of a gate dielectric with higher dielectric constant, identical metal oxide TFTs with different metal ion ratios were fabricated on 70 nm ALD deposited Al_2O_3 on silicon substrate. **Figure 3 a** shows the output and transfer curve of IZO TFT made on Al_2O_3. **Table 2** summarizes the extracted parameters for different TFTs fabricated on the ALD Al_2O_3 substrate. The device performance is seen to be enhanced and operating voltage lowered upon changing the dielectric from SiO_2 to Al_2O_3 substrate. Higher dielectric constant (κ ~3.9/9 SiO_2/Al_2O_3) and improved dielectric-semiconductor interface resulted in better electrical performance. Trap density was calculated using subthreshold slope (SS) by,

$$N_{max} = \left(\frac{C_i}{q}\right)\left(\frac{q.Sloge}{kT} - 1\right).$$

Where q is electron charge, κ is Boltzmann constant, T is temperature, C_i is the capacitance per unit area and N_{max} is the interface trap density. **Table 1** and **2** shows the measured trap density for all metal ion ratio devices; the trap density shows a drop on high κ Al_2O_3 dielectric, this is due to additional trap states present in SiO_2 as compared to Al_2O3 known to increase the sub-gap density of states (DOS)

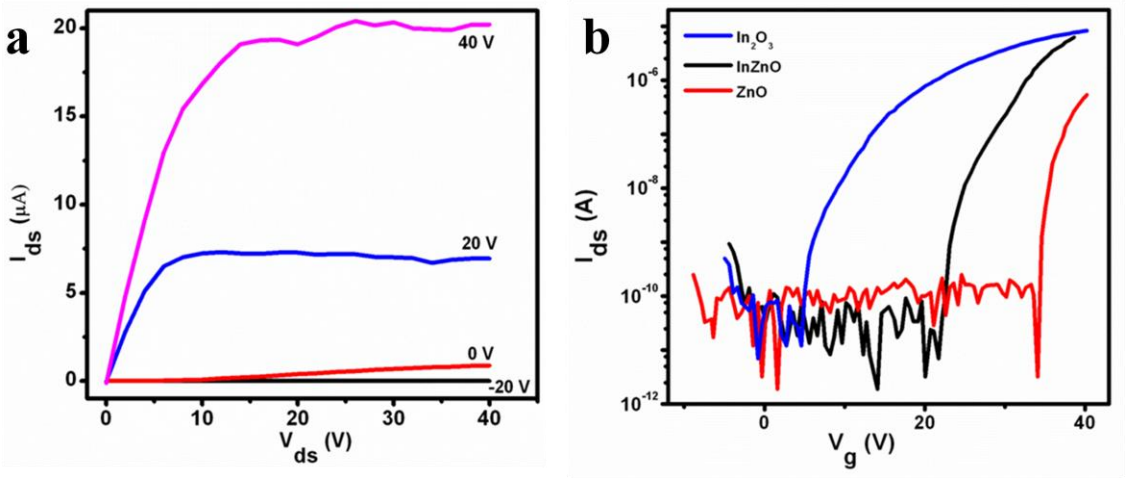

***Figure 3: a**. Output characteristics for $In_{0.5}Zn_{0.5}O$ TFT on Al_2O_3 dielectric with W/L ratio of 1000/195 µm. **b**. Transfer characteristics of TFTs with varying molar ratio of In:Zn having W/L ratio of 1000/195 µm on Al_2O_3 dielectric with W/L ratio of 1000/195 µm*

On Al_2O_3 dielectric, there is a systematic increase in mobility for the channel with higher In concentrations, as indicated in **Table 2**. Here, on addition of In, the trap density reduces nearly by 2 orders of magnitude, going from 2.2×10^{13} cm^{-3} (ZnO) to 7.79×10^{10} cm^{-3} for In_2O_3. The subthreshold swing decreases with In content, indicating that the extremely low mobility and low subthreshold slope in ZnO TFTs can be attributed to low carrier concentration and high density of surface states at the interface between the channel and gate dielectric.

Zn Conc. (%)	**In Conc. (%)**	**W/L (μm)**	**μ_{sat} (cm^2\Vs)**	**I_{on}/I_{off}**	**V_{th} (V)**	**S.Slope**	**S.Sweep (mV/dec)**	**N^{max} Trap density (cm^{-3})**
0	100	1000/195	3.72	1×10^6	6.2	5.71	5.52×10^{-3}	7.79×10^{10}
30	70	1000/195	0.6	1×10^4	7.2	3.11	3.22×10^{-1}	1.97×10^{12}
100	0	1000/195	0.023	1×10^4	34	0.14	6.95	2.2×10^{13}

Table 2: *Summary of electrical parameters for TFT measured on ALD Al_2O_3 measured at different In:Zn metal ion ratio. μ is the field effect mobility, V_{th} is the threshold voltage, and N^{max} is the trap density.*

For metal oxides used for solution-processed TFTs the electrical properties such as resistivity, carrier concentration, and mobility are strongly dependent on oxygen vacancy, metal ion ratio as well as the temperature used (for complete conversion into the oxide). Herein, we have synthesized all the transistors at 250 ˚C. Due to low strength of In-O bond higher carrier density can be generated due to higher oxygen vacancies in comparison with ZnO and InZnO formed at the same temperature, as oxygen vacancy is the main cause of carrier generation in AMOS. This attribute is responsible for the changes in the electrical characteristics as observed for In_2O_3, ZnO and InZnO. The exact nature of the amorphous metal oxides-dielectric interaction and the influence of metal cation ratio on this interaction are currently under investigation.

7.5 Conclusion

In summary, low temperature metal oxide TFTs with varying molar ratio of In:Zn were fabricated. The electrical characteristics showed better performance of pristine In_2O_3 over that of IZO and pristine ZnO TFTs. The performance of the TFTs was also tested on different dielectrics (SiO_2 and Al_2O_3) and it was shown to be improved for higher κ dielectric.

7.6 References

1. N.C. Su, S.J. Wang, C.C. Huang, Y.H. Chen, H.Y. Huang, C.K. Chiang, and A. Chin, *IEEE Electron Devices Lett.*, **2010,** 31, 680.
2. K. Nomura, H. Ohta, A. Takagi, T. Kamiya, M. Hirano and H. Hosono, *Nature*, **2004,** 432, 488.
3. K. Nomura, H. Ohta, K. Ueda, T. Kamiya, M. Hirano and H. Hosono, *Science*, **2003,** 300, 1269.
4. K. Remashan, Y.-S. Choi1, S.-K. Kang, Je.-W. Bae, G.-Y. Yeom, S.-J.Park, and J.-H. Jang, *Jpn. J. Appl. Phys.* **2010,** 49, 04DF20.
5. B. Yaglioglu, H. Y. Yeom, R. Beresford, and D. C. Painea *Appl. Phys. Lett.* **2006,** 89, 062103-1.
6. Y.-H. Kim, J.-I.Han, and S. K. Park, *Ieee Electron Device Letters*, **2012,** 33, 50.
7. T. Kamiya and H. Hosono, *NPG Asia Mater.*, **2010,** 2, 15.
8. S. Jeong, Y.-G. Ha, J. Moon, A. Facchetti, and T. J. Marks, *Adv. Mater.*, **2010,** 22, 1346.
9. Y. S. Rim, D. L. Kim, W. H. Jeong, and H. J *Appl. Phys. Lett.* , **2010,** 97, 233502.
10. J. W. Hennek, M.-G. Kim, M. G. Kanatzidis, A. Facchetti and T. J. Marks, *J. Am. Chem. Soc.*, **2012,** 134, 9593.
11. D.L. Kim, W.H. Jeong, G.H. Kim and H.J. Kim, *J. Inf. Display*, **2012,** 13, 113.
12. C.G. Lee and A. Dodabalapur, *Appl. Phys. Lett.* , **2010,** 96243501-1.
13. C. G. Choi, S. J. Seo, and B. S. Bae, *Electrochem. Solid-State Lett*. **2008,** 11, H7.

14. H. S. Kim, P. D. Byrne, A. Facchetti, and T. J. Marks, *J. Am. Chem. Soc.*, **2008,**130, 12580,
15. Y. H. Kim, J. S. Heo, T. H. Kim, S. Park, M. H. Yoon, J. Kim, M. S. Oh, G. R. Yi, Y. Y. Noh & S. K. Park, *Nature*, **2012,** 489, 128-133.
16. M. G. Kim, M. G. Kanatzidis, A. Facchetti and T. J. Marks, *Nature*, **2011,** 10, 382-388.

List of Publications

- ✓ A Quasi-Liquid Iontronic–Electronic Light-Harvesting Hybrid Photodetector with Giant Response, **Lily Mandal** , Meenal Deo, Ashish Yengantiwar, Arun Banpurkar, Jyoti P. Jog, and Satishchandra Ogale, *Adv. Mater.* **2012**, 24, 3686-3691.

- ✓ A Self-Powered UV-Vis Photo-detector based on $ZnIn_2S_4$ / Hydrogel Interface, **Lily Mandal**, Nilima S. Chaudhari and Satishchandra Ogale, *ACS Appl. Mater. Inter.*, **2013**, http://dx.doi.org/10.1021/am4025356.

- ✓ Catalyst free novel synthesis of single layer graphene (SLG) and its application in high current O-FET and phototransistor based on P3HT / SLG composite, Prasad Yadav, Chetan Chanmal, Aniruddha Basu, **Lily Mandal***, Jyoti P. Jog and Satishchandra Ogale* *RSC Adv., **2013**, 3 (39), 18049 - 18054*

Book Chapter

- ✓ Electric Field effects in Functional Metal Oxides, **Lily Mandal**, Weinan Lin, James Lourembam, Satishchandra Ogale and Tom Wu* Chapter 15, pg 407-431 Eds S. B. Ogale, T. V. Venkatesan, M. Blamire, Functional Metal Oxides New Science and Novel Applications, *Wiley VCH* **2013**.